INSTITUTO SUPERIOR DE ENGENHARIA DO PORTO

MESTRADO EM ENGENHARIA MECÂNICA

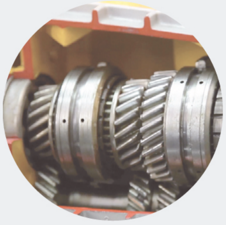

EVALUATION OF THE THERMAL TREATMENT EFFECT ON THE ENTRAPMENT OF THE POWDER IN INTERNAL CHANNELS OF PBF-LB PRINTED PARTS

ÓSCAR FRANCISCO REIS MOTA TEIXEIRA

novembro de 2020

POLITÉCNICO
DO PORTO

EVALUATION OF THE THERMAL TREATMENT EFFECT ON THE ENTRAPMENT OF THE POWDER IN INTERNAL CHANNELS OF PBF-LB PRINTED PARTS

Óscar Francisco Reis Mota Teixeira

2019/2020
ISEP – School of Engineering
Mechanical Engineering Department

EVALUATION OF THE EFFECT OF THE THERMAL TREATMENT ON THE ENTRAPMENT OF THE POWDER IN INTERNAL CHANNELS OF PBF-LB PRINTED PARTS

Óscar Francisco Reis Mota Teixeira
1140313

Dissertation presented to ISEP – School of Engineering to fulfil the requirements necessary to obtain a Master's degree in Mechanical Engineering, carried out under the guidance of the Associate Professor Francisco José Gomes da Silva from ISEP and co-supervision of the Associate Professor Eleonora Atzeni from Politecnico di Torino.

2019/2020
ISEP – School of Engineering
Mechanical Engineering Department

JURY

President
Sandra Cristina de Faria Ramos, PhD
Adjunct Professor, ISEP – School of Engineering, Polytechnic of Porto, Portugal
Supervisor
Francisco José Gomes da Silva, PhD
Associate Professor, ISEP – School of Engineering, Polytechnic of Porto, Portugal
Second supervisor
Eleonora Atzeni, PhD
Associate Professor, Polytechnic of Torino, Italy
Examiner
António Manuel de Bastos Pereira, PhD
Associate Professor with Habilitation, University of Aveiro, Portugal

ACKNOWLEDGEMENTS

Firstly, I would like to acknowledge Professor Francisco Silva for all the help and counselling provided during the last few months which were crucial for the development of this dissertation. Furthermore, I would also like to thank to Professor Eleonora, Professor Sara, Professor Salmi, and Giulio from Politecnico di Torino for all the collaboration provided during my stay in Italy. In addition, a special word of acknowledge also goes to the staff from ISEP's Erasmus Office which often contacted me to check if I was doing well and healthy.

Secondly, I owe a massive thank you to my family for all the support that they provided me since I was born. Throughout the years they have educated and loved me in the best possible way, often sacrificing themselves for my own benefit and I tremendously appreciate all their actions.

Finally, I also would like to acknowledge my friends and girlfriend for all encouragement, help, counselling, and care which were essential to keep my motivation and mental health during the current pandemic crisis.

KEYWORDS

Additive Manufacturing, Heat Treatments, Residual Stresses, Powder Bed Fusion, Selective Laser Melting, Electron Beam Melting, Inconel 718, Ti-6Al-4V

ABSTRACT

Additive manufacturing (AM) can be seen as a disruptive process that builds complex components layer upon layer. Two of its distinct technologies are Selective Laser Melting (SLM) and Electron Beam Melting (EBM), which are powder bed fusion processes that create metallic parts with the aid of a beam source. Two of the most studied and manufactured superalloys in metal AM are the Inconel 718 (IN718) and the Ti-6Al-4V. The former is commonly employed in the marine, nuclear power plants, gas turbines, and aerospace field due to its capacity of retaining good mechanical properties at high temperatures, while the latter is often used in the aerospace field due to its low density and high melting point, and in the biomedical area owing to its high corrosion resistance and excellent biocompatibility when in contact with tissues or bones of the human body. Nevertheless, the aforementioned alloys frequently require a post-processing heat treatment in order to enhance certain mechanical properties, modify the microstructure and reduce the residual stresses (RS), which are induced by thermal principles, as the gradient temperature is high because of the heating and thermal expansion upon the deposition of a new layer, and its subsequent cooling. Therefore, production errors in the components might occur due to geometrical distortion. Thus, it is mandatory to understand the expected orientation and magnitude of the RS in order to do accurate predictions of the final part properties.

The initial goal of this dissertation was to evaluate the thermal treatment effect on the entrapment of IN718 powder in internal channels of laser beam powder beam fusion manufactured components. However, due to the current pandemic, Polito's laboratories could only be used by researchers and PhD students. Having that constraint, I was advised, by Professor Francisco Silva, to write two review papers that would replace the experimental work of this thesis, being the first about residual stresses and heat treatments of Selective Laser Melted IN718 parts and the second about residual stresses and heat treatments of Electron Beam Melted and Selective Laser Melted Ti-6Al-4V components.

From the first scientific paper one can conclude that the expected microstructure in the as-built state of the IN718 components is characterized by fine columnar grains and a saturated γ matrix with the presence of the Laves phase and carbides. This heterogeneous microstructure promotes unfavourable anisotropic mechanical properties, meaning that, for high and cyclic loads applications, heat treatments must be conducted. In addition, it was also shown that RS can be lowered by applying heat treatments and favourable printing parameters, i.e. high scanning speed and low laser power.

Finally, from the second review paper, it can be concluded that that the expected as-built microstructure of the Ti–6Al–4V alloy is different in both manufacturing processes, mainly due to the distinct cooling rates. However, heat treatments can modify the microstructure, reduce RS, and increase the ductility, fatigue life, and hardness of the components. Furthermore, distinct post-treatments can induce compressive RS on the part’s surface, consequently enhancing the fatigue life.

PALAVRAS CHAVE

Manufatura Aditiva, Tratamentos Térmicos, Tensões Residuais, Fusão em Cama de Pó, Derretimento Seletivo em Laser, Fusão de Feixe de Eletrões, Inconel 718, Ti-6Al-4V

RESUMO

A manufatura aditiva pode ser vista como um processo disruptivo que cria componentes complexos camada após camada. Duas das suas tecnologias distintas são o derretimento seletivo em laser e a fusão por feixe de eletrões, que são processos de fusão em cama de pó que criam peças metálicas com o auxílio de feixe laser e eletrões, respetivamente. Algumas das superligas mais estudadas e fabricadas na manufatura aditiva de metais são o Inconel 718 e o Ti-6Al-4V. O primeiro é normalmente utilizado na marinha, centrais nucleares, turbinas a gás e no campo aeroespacial devido à sua capacidade de reter boas propriedades mecânicas a altas temperaturas, enquanto o último é frequentemente usado no campo aeroespacial devido à sua baixa densidade e alto ponto de fusão, e na área biomédica pela sua alta resistência à corrosão e excelente biocompatibilidade quando em contato com tecidos ou ossos do corpo humano. No entanto, as peças feitas das ligas anteriormente citadas frequentemente requerem um tratamento térmico após fabricadas a fim de potencializar certas propriedades mecânicas, modificar a microestrutura e reduzir as tensões residuais, que são induzidas por princípios térmicos, uma vez que o gradiente de temperatura é alto devido ao aquecimento e expansão térmica mediante a deposição de uma nova camada e o seu posterior arrefecimento. Portanto, podem surgir componentes com erros dimensionais derivados da distorção geométrica. Assim, é obrigatório entender a orientação esperada e a magnitude das tensões residuais de modo a fazer previsões precisas das propriedades da peça final.

O objetivo inicial desta dissertação era avaliar o efeito do tratamento térmico no aprisionamento do pó IN718 em canais internos de componentes fabricados por derretimento seletivo em laser. No entanto, devido à atual pandemia, os laboratórios de Polito só podiam ser usados por investigadores e alunos de doutoramento. Tendo essa restrição, fui aconselhado, pelo Professor Francisco Silva, a escrever dois artigos de revisão bibliográfica que iriam substituir o trabalho experimental desta tese, sendo o primeiro sobre tensões residuais e tratamentos térmicos de peças de IN718 produzidas por derretimento seletivo em laser, e o segundo sobre tensões residuais e tratamentos térmicos de componentes de Ti-6Al-4V fabricados por fusão de feixe de eletrões e derretimento seletivo em laser.

Do primeiro artigo científico pode-se concluir que a microestrutura esperada no estado *as-built* dos componentes do IN718 é caracterizada por grãos colunares finos e uma matriz γ saturada com a presença da fase Laves e carbonetos. Essa microestrutura heterogénea promove propriedades mecânicas anisotrópicas desfavoráveis, fazendo com que, para aplicações com cargas elevadas e cíclicas, sejam realizados tratamentos térmicos. Além disso, também foi mostrado que as tensões residuais podem ser reduzidas pela aplicação de tratamentos térmicos e parâmetros de impressão favoráveis, ou seja, alta velocidade de *scan* e baixa potência do laser.

Finalmente, a partir do segundo artigo de revisão, pode concluir-se que a microestrutura *as-built* esperada da liga Ti–6Al–4V é diferente em ambas as tecnologias de fabrico, principalmente devido às distintas taxas de arrefecimento das mesmas. No entanto, os tratamentos térmicos podem modificar a microestrutura, reduzir as tensões residuais, aumentar a ductilidade bem como a vida à fadiga e dureza dos componentes. Além disso, pós-processamentos distintos podem induzir tensões residuais compressivas na superfície das peças e, consequentemente, aumentar a vida à fadiga das mesmas.

LIST OF ABBREVIATIONS, UNITS AND SYMBOLS

List of Abbreviations

3D	Three-dimensional
AC	Air Cooling
AL_2O_3	Alumina
Al-Si-Mg	Aluminium-Silicon-Magnesium
AM	Additive Manufacturing
ASTM	American Society of Testing and Materials
$CaCO_3$	Calcium Carbonate
CAD	Computer-aided Design
CO_2	Carbon Dioxide
Co-Cr-Mo	Cobalt-Chromium-Molybdenum
CT	Computed Tomography
DA	Double Aging
DMLS	Direct Metal Laser Sintering
EaB	Elongation at Break
EBM	Electron Beam Melting
ELI	Extra Low Interstitial
FAHS	Fly Ash Hollow Spheres
FCC	Face-Centred Cubic
FDM	Fused Deposition Modelling
GNP	Graphene Nano-platelets
HIP	Hot Isostatic Pressing
HO	Homogenization
HT	Heat Treatment
IC	Integrated Chips
IN	Inconel
LaB_6	Lanthanum Hexaboride
LED	Laser Energy Density
MgO	Magnesium Oxide
MJF	Multi Jet Fusion
Nb	Niobium
Ni	Nickel
PA	Polyamide
PBF	Powder Bed Fusion
PBF-LB	Laser Beam Powder Bed Fusion
PC	Polycarbonate
PCL	Polycaprolactone
PE	Polyethylene

PET	Polyethylene Terephthalate
PLA	Polylactic Acid
PP	Polypropylene
PPROC	Post-processing
Polito	Politecnico di Torino
PSD	Particle Size Distribution
Ra	Arithmetic Average of the Surface Roughness
Re	Rhenium
RS	Residual Stresses
SA	Solution Annealing
SiO_2	Silica
SLμM	Micro Selective Laser Melting
SLM	Selective Laser Melting
SLS	Selective Laser Sintering
SM	Subtractive Manufacturing
SS-X	Bidirectional scanning without 90° rotation between successive layers
SS-XY	Bidirectional scanning with 90° rotation between successive layers
STL	Standard Tessellation Language
Ta	Tantalum
Ti	Titanium
TiC	Titanium Carbide
TPU	Thermoplastic Polyurethane
UTS	Ultimate Tensile Strength
VED	Volumetric Energy Density
W	Tungsten
WC	Tungsten Carbide
XRD	X-ray Diffraction
Y-TZP	Yttria-stabilized Tetragonal Zirconia Polycrystal
YS	Yield Strength

List of Units

°C	Celsius degree
μm	Micrometre
g	Gram
J	Joule
J/mm^2	Joule per Square Millimetre
J/mm^3	Joule per Cubic Millimetre
min	Minute
mm	Millimetre
MPa	Mega Pascal
W	Watt

Lists of Symbols

$	Dollar
%	Percentage
€	Euro
d	Laser Spot Size
E	Modulus of elasticity
E_I	Linear Input Energy Density
E_L	Linear Energy Density
E_S	Surface Energy Density
E_V	Volumetric Energy Density
h	Hatching Space
P	Laser Power
t	Layer Thickness
T_m	Melting Temperature
v	Laser Scanning Speed
w	Beam Waist
γ	Gamma Matrix
γ’	Prime Phase Matrix ($Ni_3(Al,Ti)$)
γ’’	Double Prime Phase Matrix (Ni_3Nb)
ρ	Density
σ_y	Yield Strength
σ_u	Ultimate Strength

GLOSSARY OF TERMS

Green Part	A component in which the substrate is joined by polymeric glue and requires additional post-processing.
Scaffold	Artificial extracellular matrix that allows the regeneration of large parts of broken bones.
Fly Ash Hollow Spheres	Fly ash hollow spheres are hollow spheres made from silica and alumina with air or inert gas fillings and are by-products of coal combustion in thermal power plants.
Scalmalloy	Aluminium-Magnesium-Scandium Alloy as ductile as titanium and light as aluminium. Apworks property.
Voxel	Also called a volumetric pixel, a voxel is one of a group of small volumes at which some density parameter of an object is estimated in a three-dimensional tomographic reconstruction.

FIGURES INDEX

TABLES INDEX

INDEX

INTRODUCTION

1.1 CONTEXTUALIZATION
1.2 MAIN GOALS
1.3 METHODOLOGY
1.4 DISSERTATION STRUCTURE
1.5 WELCOMING INSTITUTION

1 INTRODUCTION

1.1 CONTEXTUALIZATION

1.1.1 ADDITIVE MANUFACTURING

Additive manufacturing (AM), also known as three-dimensional (3D) printing, can be described, according to the American Society of Testing and Materials (ASTM), as “The process of joining materials to make objects from 3D model data, usually layer upon layer… ”[1]. In fact, it starts with a 3D model designed in a CAD software that is subsequently saved into an STL file, which essentially consists of a mesh composed of several triangles. Then, the latter is passed to the machine software and the printing parameters are defined. After that, the component in question is printed and, subsequently, removed from the build plate and post-processed, if necessary. Finally, and after completing these steps, you have a part ready to use [2]. This technology is said to have been born in 1981 through Hideo Kodama, a researcher at the Nagoya Municipal Institute for Industrial Research [3]. He published an article on a functional photopolymer rapid prototyping system that printed objects layer upon layer. In 1984, and based on Hideo's research, Charles Hull created a stereolithography system and founded the first AM company, called 3D Systems. This moment can be considered the true driver of the AM technology, taking us to the present day where it is beginning to spread in several markets.

1.1.2 ECONOMIC REPORT AND MARKETS

This technology is considered economically competitive for small to medium batches, as it does not need tools or moulds to manufacture a component. In addition, it allows the creation of complex geometries, which other manufacturing processes are not able to match. All of this, plus the recent technological advances, grant the possibility of producing a higher percentage of functional parts by the means of AM, as you can see in Figure 1.

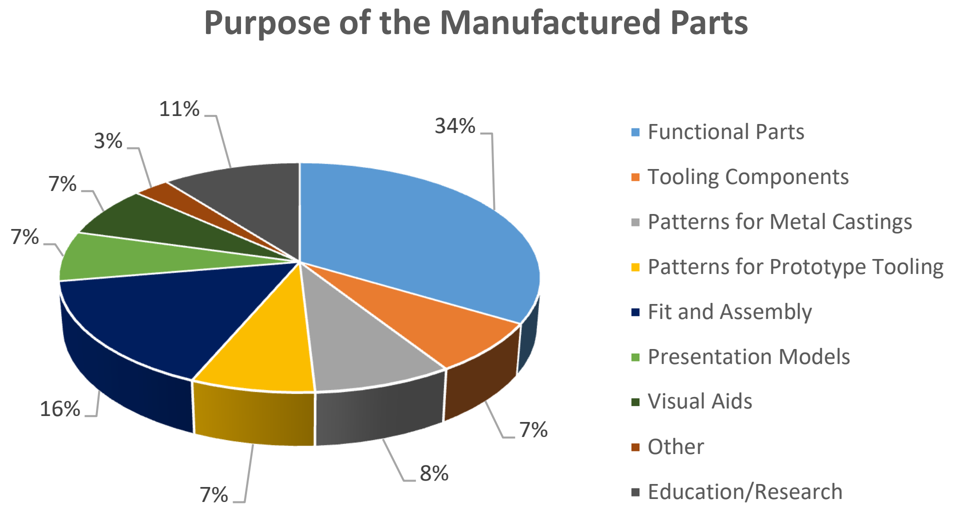

Figure 1 - Purpose of the manufactured parts. Adapted from: Wohlers Report 2017 [4]

Regarding the main markets, it is known, thanks to the Wohlers Report, that in 2016 the industrial sector was the one that used this technology the most, followed by the aerospace and automotive sector (Figure 2). However, these last two are expected to increase the use of additive manufacturing, since for the automotive market any reduction on the vehicle development time means a faster reach to the market of the product, and for the aerospace market, is crucial reducing the mass of a single component and the number of assemblies, in order to increase the energy efficiency of the entire system.

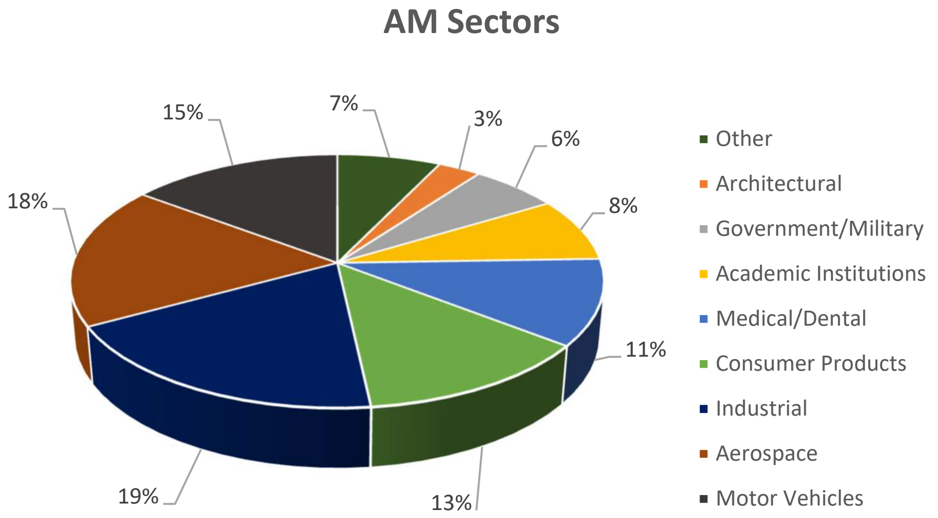

Figure 2 - Main economic sectors. Adapted from: Wohlers Report 2017 [4]

In addition, several companies are eager to have or manufacture AM systems because of the countless possibilities associated to this disruptive technology. Thus, in 2016 there were a total of 97 companies building and selling 3D printing machines, an increase of 35 companies compared to 2015. This affluence increases the size of the market year after year and, according to Statista, in 2021 it will reach a figure of 21 billion $ (Figure 3).

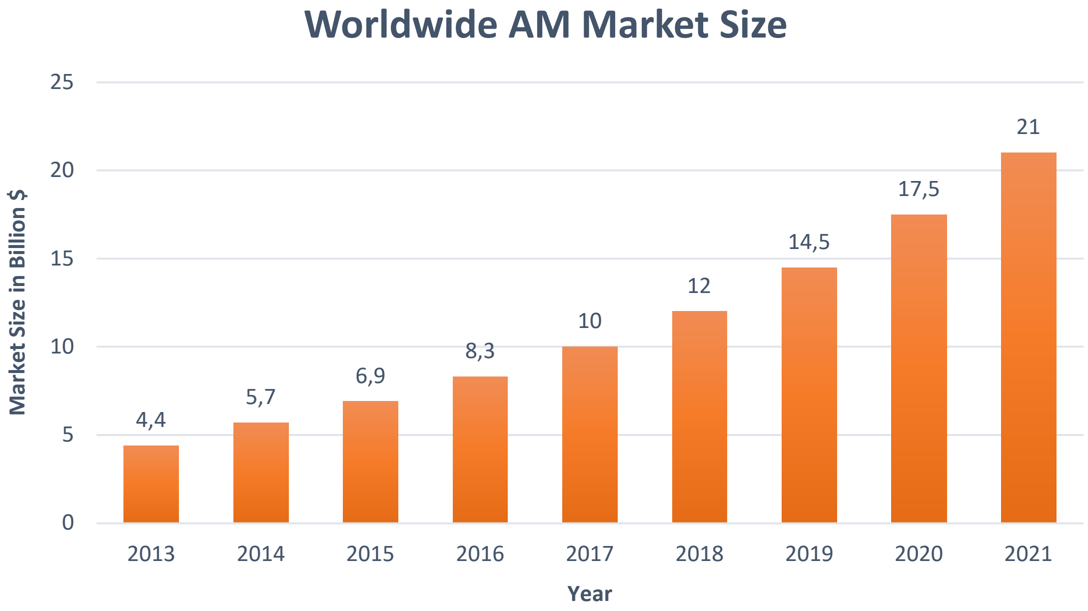

Figure 3 - Worldwide AM market size. Adapted from: Statista [5]

1.2 MAIN GOALS

The main objective of this report is the bibliographic research of the topics Laser Beam Powder Bed Fusion (PBF-LB), the super alloys existing in this technology, as well as some methods used to study the components after printing. The practical part aimed to create a new approach that evaluated the thermal treatment effect on the powder entrapment in internal channels, however, it could not be done due to the current pandemic.

1.3 METHODOLOGY

The methodology followed for the bibliographic research consisted of analysing several books, research and review articles, as well as standards, master's/doctoral theses, and websites.

1.4 DISSERTATION STRUCTURE

The thesis is divided into six different chapters, in order to facilitate the reader's understanding and reading. With that said, we have:

- Introduction – where is written a contextualization of the topic, defined objectives and the methodology approached;
- Literature Review – this second chapter aimed to introduce the PBF-LB technology state-of-the-art, as well as the superalloys used in AM. Furthermore, residual stresses and computed tomography methods are also addressed;
- Thesis Development – where the experimental work would be described;
- Conclusions – where a summary about the bibliographic research is made in addition with final considerations about the work;
- References – chapter dedicated to present the bibliographic references consulted when writing this report;
- Annexes – last chapter that includes relevant information aligned with this work.

1.5 WELCOMING INSTITUTION

The experimental part of this academic work was developed at Politecnico di Torino (Polito), which is a university based in the city of Turin, Italy, established in 1859. It is among the most prestigious public education and research institutions in the engineering branch, at both international and national levels and has an annual budget of 263 million €. In fact, Polito got classified as the 31st best university in the world on Mechanical, Aeronautical, Manufacturing and Production Engineering subjects, by the 2019 QS World University Ranking. In addition, it is a university that cares and believes in an international student community, with the enrolment of 16% foreign students in the 2018/2019 academic year (Source: Politecnico at a glance, 2020).

Within Polito there are several different departments, however, the experimental work was going to be carried out in the Department of Management and Production Engineering (DIGEP), and the Department of Applied Science and Technology (DISAT). At the DIGEP, the specimens were going to be built, an X-ray CT evaluation would be performed, and the RS were also going to be measured and analysed in partnership with the staff from the Advanced Manufacturing Technologies (AMTECH) research group. At the DISAT, activities concerning specimen preparation would be performed, as well as porosity evaluation and microstructure analysis.

LITERATURE REVIEW

2 LITERATURE REVIEW

In the previous chapter, a general introduction to the additive manufacturing technology was made, however, in this second chapter the topics of PBF-LB will be addressed, as well as superalloys such as Titanium (Ti), Nickel (Ni), Cobalt-Chromium-Molybdenum (Co-Cr-Mo) and Aluminium-Silicon-Magnesium (Al-Si-Mg). Finally, the topics of computed tomography and residual stresses will also be discussed.

2.1 LASER BEAM POWDER BED FUSION PROCESSES

According to ASTM F2792-12a [1], it is possible to subdivide the Powder Bed Fusion (PBF) category into three different technologies, shown in Table 1.

Table 1 - ASTM F2792-12a classification. Adapted from [1]

Category	Technology	Materials
Powder Bed Fusion	Selective Laser Sintering	Metals, polymers and ceramics
	Selective Laser Melting	
	Electron Beam Melting	

In fact, when talking about PBF-LB, only the technologies of Selective Laser Sintering (SLS) and Selective Laser Melting (SLM) can be included, as only these two use a laser to promote the heating and subsequent joining of material. As the name implies, Electron Beam Melting (EBM) technology uses a high-speed electron beam to promote material fusion, transforming kinetic energy into heat. Having said that, this last technology will be discarded since it does not fit with the topic of this dissertation.

Recently, some studies have been covering the topics of Direct Metal Laser Sintering (DMLS) and Multi Jet Fusion (MJF), however, the first technology can be seen as an adaptation of SLM and, therefore, will be grouped with it [6]. The small differences between the two technologies are shown in Table 2. Nevertheless, DMLS can be also be incorrectly labelled as SLS, but the former technology is not used on metals. Regarding MJF, it is owned by Hewlett-Packard and uses an infrared lamp to cure two liquid agents called fusion and detailing [7], hence it will not be covered in this report for not using a laser.

Table 2 - Differences between SLM and DMLS [6,8]

	SLM	DMLS
Differences	Usually used in pure metals	Used in metal alloys
	Needs more energy than DMLS	Needs less energy than SLM
	The material is melted	The material is sintered

2.1.1 SELECTIVE LASER SINTERING

2.1.1.1 HOW IT WORKS

The SLS technology was developed at the University of Texas in Austin, United States of America, and was the first PBF-LB process to be commercialized [2]. The main components of an SLS printer can be seen in Figure 4 and the operation method can be briefly described in the following steps:

- Firstly, the powder cartridge rises and dispenses a predefined amount of powder;
- In the second place, the levelling roller/blade creates a uniform layer of dust on the construction platform and places the excess powder in another cartridge opposite to the first one;
- Thirdly, the powder is preheated by an infrared lamp to a temperature below the glass transition;
- Then, a low-power CO_2 laser sinters the material;
- Finally, the construction platform lowers according to the thickness of each layer, normally varies between 80 and 150 µm, and the process is repeated until the final piece is made [9].

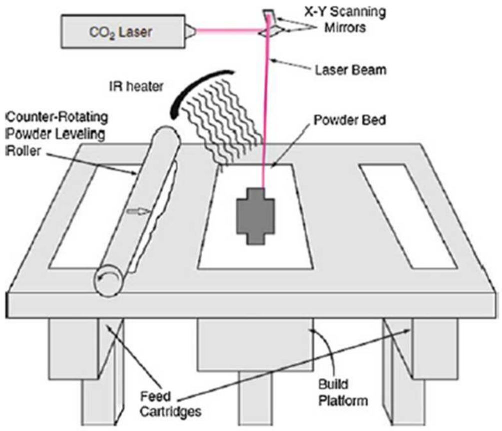

Figure 4 - Main components of an SLS printer [2]

It is extremely important to emphasize that this process must be done in a chamber with an atmosphere without humidity and surrounded by an inert gas, usually nitrogen or argon, in order to avoid oxidation of the material [10].

2.1.1.2 MATERIALS

When it comes to materials, SLS can be considered to use practically only powdered polymers, with polyamide 12 (PA12) being the main one, although there are also other types of PA, such as PA 11. In addition, there is also the polyethylene terephthalate (PET), thermoplastic polyurethane (TPU) and polycaprolactone (PCL) [11,12]. However, ceramic powders can also be employed [13] and, currently, it is possible to create composite materials, as Nofal, M. et al demonstrated by joining expanded graphite with paraffin wax (Figure 5) [14].

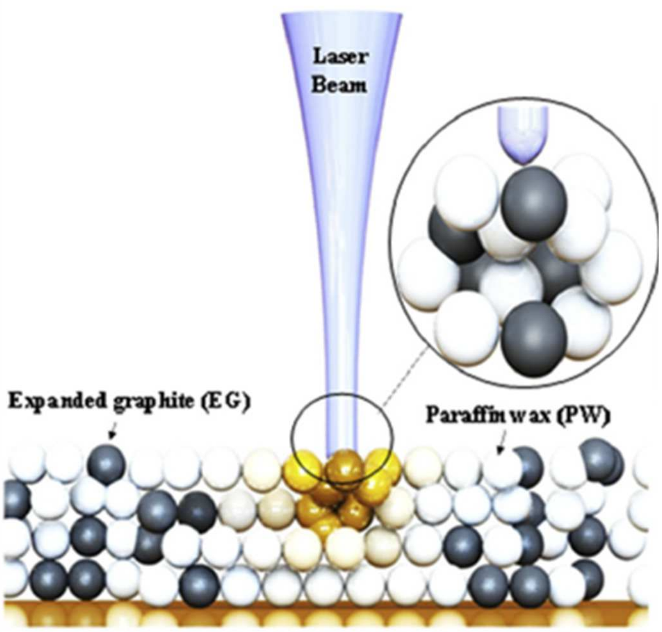

Figure 5 - Demonstration on how to create a composite material using SLS [14]

In this technology, support structures are not necessary, because, firstly, the powder when compacted acts as support and, secondly, the preheating of the powder prevents deformations in the component when the material is partially melted by a low-power laser since, the expansion and subsequent thermal contraction of the material is done practically in a uniform way. However, this preheating makes it not advisable to reuse the powder without adding virgin substrate in certain materials. In Table 3, it is possible to view studies related to it.

Table 3 - Studies related to powder reuse in SLS

Bibliographic References	Summary
Gu, H. *et al* [15]	In this article, the authors simulated the preheating of a PET powder outside the printer using a low vacuum oven. In reality, this substrate is equivalent to the powder that stays long hours inside the printing chamber exposed to a low nitrogen flow and temperatures close to the material's melting zone. After almost 100 hours of exposure, they printed a specimen and found that its mechanical properties (modulus of elasticity, tensile strength, among others) and its molecular weight had not undergone significant changes when compared to the specimen printed with virgin powder. So, they came to the conclusion that a PET powder exposed up to 100 hours of preheating can be reused without the addition of virgin powder.
Dadbakhsh, S. *et al* [16]	In this work, the researchers analysed a PA12 powder in three different states, virgin, used-virgin mixed, and used. For that, they printed several specimens of each state of powder and reached some conclusions. The first was that the mechanical properties of test specimens printed with a used powder were significantly inferior to those of virgin specimens. This was due to the loss of crystallinity when the substrate ages. However, when comparing virgin specimens with those printed with 50% of each powder, they came to the conclusion that there was no significant difference in their mechanical properties, so the powder ratio used was ideal.
Kumar, S. *et al* [17]	The authors of this article propose a different reuse of the substrate. Kumar, S. et al say that the aged PA12 powder can be turned into a filament for later use in a Fused Deposition Modelling (FDM) printer. But, for this, the powder has to be mixed with tungsten carbide (WC) in order to improve its mechanical properties. Furthermore, plasticizers and additives should also be added to improve the plasticity of the filament and promote a uniform mixing of the various particles, respectively. However, they concluded that, for this model to work, it would be beneficial if the source of the aged powder and the processing location were the same, in order to avoid transportation costs.
Kozlovsky, K. *et al* [18]	Kozlovsky, K. et al investigated the mechanical properties of nylon specimens that had been printed using a reused powder 1, 4 and 8 times. For this, they performed mechanical tests in order to determine the ultimate tensile strength (UTS) and elongation at break (EaB) of the different specimens. After analysing the results, the authors found that there was a significant decrease in the value of the UTS between reuse 1 and 4, however the same was not verified in EaB. Between reuse 4 and 8, the UTS and EaB values did not differ significantly. As such, the researchers concluded that nylon can be reused without significantly compromising the quality of the final piece.

2.1.1.3 POST-PROCESSING

In order to improve the mechanical properties as well as the surface finish of the parts printed by SLS, it is advisable that, after manufacture, post-processing is performed. Table 4 shows some studies conducted over the years in order to understand how post-processing affects the final properties of materials.

Table 4 - Post-processing in SLS

Bibliographic References	**Summary**
Nelson, J. C. *et al* [19]	The researchers wanted to find out what was the influence of pressure on the post-processing of polycarbonate (PC) specimens, taking into account that they do not reach their full density when printed. In order to accomplish the latter, they used a vacuum oven and applied different pressures when heating the samples. They concluded that the pressure does not influence the contraction of the PC and, also, that the material when heated close to the glass transition temperature presents a uniform contraction.
Zarringhalam, H. *et al* [20]	In this work, the authors submitted PA specimens to heat treatments of different durations and temperatures, as well as to three different polymeric infiltrants. Then, they performed tests to ascertain the impact force, modulus of elasticity, breaking stress and elongation at breaking. After comparison with tabulated values, they found out that the test pieces exposed to heat treatments had more favourable results than those that were infiltrated. In addition, the greater the heating above the glass transition temperature, the better the mechanical behaviour, however, the specimen heated to the closest melting temperature showed serious deformations.
Yan, C. *et al* [21]	The authors of this article used a dissolution-precipitation process in order to coat metallic powder with PA12. Then, they used an indirect method to produce metallic parts through SLS, in which the polymeric coating served as "glue" for the metallic parts, forming a green part. The latter was subjected to post-processing in an oven, in order to remove the polymeric glue and, later, it was infiltrated with epoxy resin. When comparing the post-processed parts with the green parts, they concluded that the former had better mechanical properties than the latter.
Shahzad, K. *et al* [22]	In this work, the authors wanted to study the effect of different types of post-processing of a composite powder of alumina (Al_2O_3) and polypropylene (PP). To this end, they produced green parts that later followed four different post-processing paths. The first was debinding and sintering, the second was pressure infiltration followed by debinding and sintering, the third was warm isostatic pressing and debinding and sintering, and the fourth was pressure infiltration followed by warm isostatic pressing and debinding and sintering. After analysing the theoretical density of the pieces, they concluded that the

Bibliographic References	Summary
	combination of warm isostatic pressing with debinding and sintering was the one that produced pieces with the highest density (89%).

Several companies offer different finishes, in order to enhance certain properties of the final product. For example, 3D Hubs has a wide range of finishes available, including standard, vibro polish, dyeing, spray painting or lacquering, watertightness, and metallic coating [23]. The advantages and disadvantages of these can be seen in Table 5.

Table 5 - Different finishes performed by 3D Hubs [23]

Finishing	Advantages	Disadvantages
Standard	Good overall accuracy because part geometry remains the same; Low cost.	Grainy surface finish; Cannot change the colour of the part.
Vibro Polish	Excellent surface roughness; Able to make several pieces at the same time; Removes sharp edges	It is not advisable for delicate features because it affects part geometry.
Dyeing	Multiple colours available; It does not affect part geometry and is suitable for complex parts; Better cost-benefit compared to other techniques.	Dye penetration of only 0,5 mm; Finish is not shiny.
Spray painting or Lacquering	Lacquer can improve mechanical properties; Bright colour finish; Improves protection against ultraviolet rays.	Slightly influences the geometry of the part; Requires prior surface cleaning.
Watertightness	Enhances water resistance; Able to improve mechanical strength.	Thick coating that influences the geometry of the part.
Metal Coating	Improves mechanical properties; Excellent surface finish; Ensures electrical conductivity to parts.	High cost; Increases lead time; Limited number of materials available.

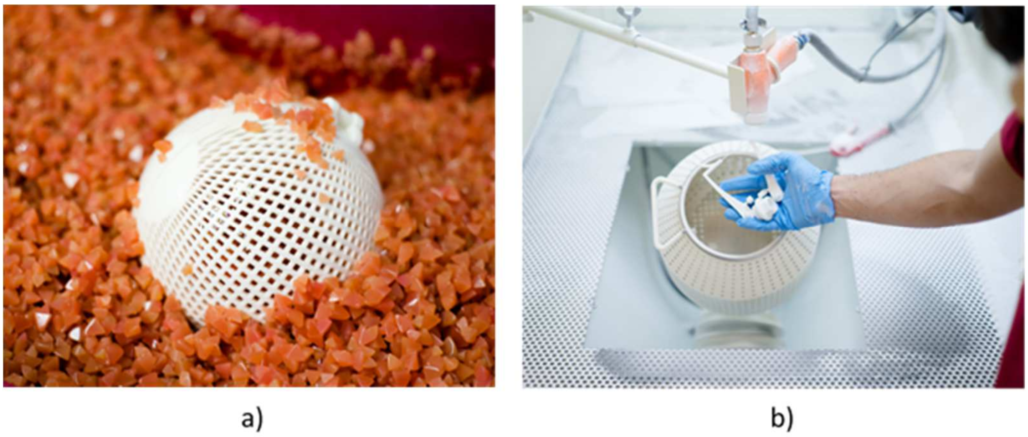

Figure 6 - Different finishes: a) vibro polish, b) powder removal with compressed air, part of the standard finish [23]

2.1.1.4 RECENT DEVELOPMENTS

Nowadays, this technology is being widely used in the medical industry, namely in the dental field for the creation of ceramic implants, made from a powder with several constituents (Y-TZP/MgO/Epoxy Resin E12) [24]. In addition, the aerospace area has also used this process to manufacture small scale models in order to conduct tests in wind tunnels [25]. Table 6 shows other studies carried out recently in different areas.

Table 6 - Recent developments

Bibliographic References	**Summary**
Gayer, C. *et al* [26]	The researchers developed a composite powder of polylactic acid (PLA) and calcium carbonate ($CaCO_3$) capable of being reabsorbed by the human body. This powder is suitable for the biomedical area since the latter frequently uses printed implants and scaffolds (artificial extracellular matrices that allow the regeneration of large parts of broken bones). Furthermore, for substrate manufacturing, they used an impact mill that processed four different powders in terms of PLA's inherent viscosity. After some attention paid to the printing parameters, namely the laser power, the authors concluded, that the powder with lower viscosity was the most suitable in terms of processability.
Chen, A. *et al* [27]	In this work, the authors produced a composite powder of PA12 and fly ash hollow spheres (FAHS, a by-product generated in coal plants), in order to create pieces of mullite ceramic foam with a high degree of structural complexity. The powder was made in a pressure reactor by joining FAHS with granules of PA12 and an ethanol solution. After increasing the temperature, the PA12 dissolved and, on cooling, it crystallized, forming the composite substrate. Then, they printed several specimens in order to understand how the printing parameters and the mass percentage of PA12 influenced porosity

Bibliographic References	Summary
	and compression stress. Finally, they concluded that the increase of the sintering temperature reduced the porosity in the samples and increased the compression stress. On the other hand, the increase of PA12 powder's weight percentage by 5% slightly increased the porosity of the parts and decreased the compression stress.
Singamneni, S. *et al* [28]	Singamneni, S. et al mixed a PA powder with a keratin powder, using different weight percentages of the latter, 5 and 10 percent, respectively. Similarly, they also made a mixture, like the previous one, however, they used polyethylene (PE) instead of PA. Consequently, after printing, they performed characterization tests and concluded that the presence of keratin in the PA substantially decreased the inter-particle bond, while in the PE mixture the decrease was almost imperceptible.
Meng, Z. *et al* [29]	The authors of this scientific paper have developed a new strategy for the design and fabrication of PCL scaffolds so that they can easily adjust their mechanical properties. For this, the scaffolds were printed in a way to form a network of sinusoidal filaments instead of linear ones. After carrying out compression tests on different types of scaffolds, they concluded that their flexibility can be significantly changed, since the elastic modulus went from 1944 kPa to 678 kPa, by modifying the linear network into a sinusoidal one. In addition, when the sinusoidal network period increased, the flexibility also improved because the elastic modulus decreased to 27 kPa.

2.1.2 SELECTIVE LASER MELTING

2.1.2.1 HOW IT WORKS

According to the patent issued by the Fraunhofer Institute, this technology emerged in 1996 with Wilhelm Meiners, Konrad Wissenbach and Andres Gasser as main inventors [30]. The operating method can be described in the following steps and analysed in Figure 7:

- First, the building platform is heated in order to reduce the deformations caused by temperature differences (only on some machines);
- Then, the powder cartridge rises, thanks to an actuator, and dispenses a predefined amount of powder;
- Third, the levelling roller/blade creates a uniform layer of powder on the construction platform and places the substrate excess in another cartridge opposite the first one;
- Then, a high energy density laser melts the powder forming a melt pool of approximately 100 µm in length [31];

- Finally, the construction platform lowers according to the thickness of each layer, usually varies between 20 and 100 µm depending on the material, and the process is repeated until the final piece is complete [32].

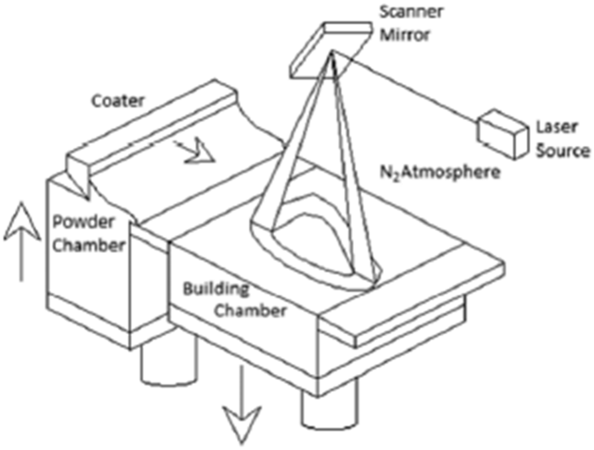

Figure 7 - Illustrative image of the SLM process [31]

Similar to SLS, this process must be done in a chamber surrounded by an inert gas, to avoid oxidation of the material after melting. However, in this technology the parts are usually connected to a substrate plate by support structures in order to reduce deformations when printing. Since the SLM is capable of producing parts with a relative density between 90 and 100 percent, the only necessary post-processing is usually the removal of the support structures [33].

2.1.2.2 MATERIALS

In general, SLM is considered to work with metallic powders, namely steel alloys, Ti, Ni, Co-Cr-Mo and Al. In addition, recently, precious metals such as gold, silver, and platinum have been introduced [34]. Furthermore, there is also the possibility of using ceramic substrates, for example alumina or silica (SiO_2), however it is necessary to pay special attention when printing them, because they combine a high melting temperature with a low ductility. For this reason, and thanks to the temperature differences that cause thermal stresses, ceramics tend to crack easily as Zheng, Y. et al demonstrated [35]. Moreover, it is also possible to print composite materials, such as stainless-steel powder mixed with titanium carbide (TiC), in order to improve wear resistance and mechanical properties at high temperatures [36].

According to Table 7, several studies were carried out regarding the reuse of the powder in the SLM technology. It was concluded that there are alloys more suitable than others to be reused continuously, namely the denser ones.

Table 7 - Substrate reuse in SLM

Bibliographic References	**Summary**
Grainger, L. [37]	Grainger, L., a Renishaw collaborator, studied the effects caused by the reuse of titanium powder, Ti_6Al_4V Grade ELI (Extra Low Interstitial), namely the amount of oxygen and nitrogen in the substrate, particle size distribution (PSD), density and, also, fluidity. For this, they used the AM250 printer 38 times for 3 months, in order to spend all the powder from the cartridge. The researcher concluded that, around the 16th printing, oxygen levels started to fall outside the allowable limits for ELI grade titanium but remained allowable within grade 5. Eventually, nitrogen levels also deviated outside the limits. In addition, the fluidity of the powder improved as the number of prints increased, because the PSD decreased due to the deterioration of the particles.
Cordova, L. *et al* [38]	The authors of this article analysed several substrates, including Inconel 718 (IN 718), Ti6Al4V, AlS10Mg and Scalmalloy (aluminium-magnesium-scandium alloy), in order to understand the impact of their reuse. For that, they used the SLM Solutions 280 machine and printed specimens of inconel 38 times, titanium 11 times, aluminium 6 times and scalmalloy 3 times. After testing, they compared the PSD, morphology, and fluidity of virgin and used powders. They concluded that the lower density alloys suffered a greater increase in PSD, negatively influencing the fluidity of the substrate. In addition, IN and aluminium showed particle elongation as well as the appearance of satellites.
Ardila, L. *et al* [39]	In this article, the authors studied the properties of an IN 718 powder that has been recycled whenever printed again. At each new iteration, Ardila, L. et al collected the specimens for analysis using mechanical tests, as well as powder samples to study their properties, and recycled the remaining powder by sieving and drying. At the end of 14 cycles, they spent 10 kg of 25 in the cartridge and collected 0,6 kg through the sieving, thus achieving a material utilization efficiency greater than 95 percent. They concluded that, through this methodology, there were no significant changes in the shape and composition of the substrate and, still, that the mechanical properties of the test pieces were similar in all iterations.
Pinto, F. C. *et al* [40]	Pinto, F. C. et al took into account that, after several reuses of the 316L stainless steel powder, a phase change occurred, that is, it stopped being totally austenitic, and became 6% vol. of δ-ferrite. After printing cylindrical specimens with the reused powder, they concluded that voids were created due to the magnetic agglomeration of δ-ferrite particles. Having said this, and to improve the quality of the pieces, they suggested that the powder, once sieved, should also be separated magnetically in order to lose the δ-ferrite particles.

2.1.2.3 POST-PROCESSING

As previously mentioned, part of the post-processing of this technology consists of removing the support structures, however, others can also be applied, namely grinding, sandblasting, and plasma electrolytic polishing, in order to improve the surface roughness of the part. If it is intended to increase the density or change the microstructure of a component, hot isostatic pressing (HIP) and subsequent heat treatment (HT) can be used, as dictated by ASTM F3055 standard [41]. Table 8 shows studies related to what was said previously.

Table 8 - Post-processing used in SLM

Bibliographic References	**Summary**
Liu, Y. *et al* [42]	The authors studied the effects of post-processing (PPROC) on the mechanical properties and microstructure of the IN 718 powder. For this, after printing samples on the SLM Solutions 280 machine, they used HIP followed by an HT, taking into account that the substrate could be strengthened through the γ’ (Ni_3 (Al, Ti)) and γ’’ (Ni_3Nb) phases in the γ matrix. Liu, Y. et al used the ASTM F3055 standard and, as such, the HIP was performed at 100 MPa and 1120 °C followed by a cooling of 150 °C/min under an inert atmosphere. Then, they performed an HT that consisted of annealing and aging, in two distinct stages. After carrying out several tests, they compared the specimens that underwent PPROC with those that did not and, consequently, they concluded that the density of the former was higher than that of the latter, as the latter had voids inside. In addition, the specimens without PPROC showed a microstructure composed mainly of γ grains. However, in the other specimens, the PPROC caused precipitation of the γ’’ phase with recrystallization of the γ and grain growth in a heterogeneous way. Finally, PPROC reduced the stiffness of the test pieces but increased the σ_y and σ_u.
Löber, L. *et al* [43]	The researchers compared different post-processing, including grinding, sandblasting and plasma electrolytic polishing, in order to understand which one would be the best to reduce the surface roughness that is characteristic of the pieces printed by SLM. They concluded that grinding was the process with the best results in terms of surface roughness (Ra = 0,34 ± 0,01 µm), however, it is only viable for parts without geometric complexity. In addition, they also found that, for more complicated parts, the combination of sandblasting with plasma electrolytic polishing was the one that obtained a lower surface roughness (Ra = 3,58 ± 0,09 µm).
Sangid, M. D. *et al* [44]	In this article, the authors studied the influence that post-processing has on the microstructure of the IN 718 powder. For this, they printed and compared the specimens in the as-built state with those that underwent HT (homogenization, solution, and aging). They concluded that the ultimate tensile strength largely increased due to HT and the anisotropy was reduced,

Bibliographic References	Summary
	as there was precipitation of the γ’ and γ’’ phases. In addition, and after an X-ray computed tomography analysis, they inferred that there was a decrease in porosity.
Sing, S. L. *et al* [45]	Sing, S. L. et al studied the influence that post-processing has on the microstructure and mechanical properties of a CoCrMo powder. Firstly, they printed several specimens on the SLM 250HL machine and then defined three different HT cycles. The first HT consisted of a solution treatment at 1220 °C for 1 hour, followed by water quenching. The second consisted of preheating at 815 °C for 4 hours, followed by a solution treatment at 1220 °C for 2 hours. The third only differed from the first in the number of hours, as it was done for 4 hours. After performing mechanical tests, they compared the yield strength (YS) and UTS values of test pieces that underwent HT and as-built, with parts obtained by casting. They concluded that the values of YS and UTS were almost double in the as-built parts than in those obtained by casting. In addition, the HT reduced the mechanical resistance of the components, since there was the formation of carbides that outweighed the stress relief effect.

2.1.2.4 RECENT DEVELOPMENTS

Currently, this process is used with great frequency in the medical field, as it allows the manufacture of customized components for each case and person. Furthermore, it is also used in the aerospace area, because, together with topological optimization, it allows to reduce the mass of the parts, thus increasing the airplane's energy efficiency, as Seabra, M. et al demonstrated [46]. In addition, there is a connection between this technology and motorsports, since Cooper, D. E., et al published an article in which Red Bull Technology manufactured 0,5 mm thick hydraulic channels (Figure 8) and found that there was a mass reduction and a 250 percent increase in fluid flow when compared to previously used parts [47].

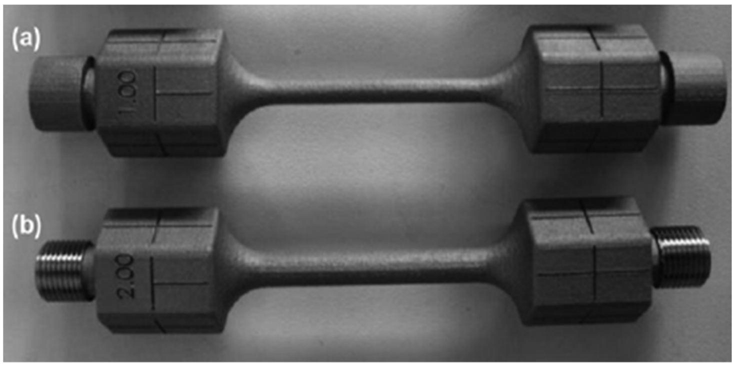

Figure 8 - Components before (a) and after machining (b) [47]

Christoph Hansen, head of AM for the Sauber F1 Team, recently gave a PowerPoint presentation in which he shared that the sports team uses this technology to manufacture competition parts, namely pipes for the turbo, exhaust and intercooler, as well as uprights covers and roll hoops [48]. Table 9 shows other recent studies related to this process.

Table 9 - Recent developments in SLM

Bibliographic References	**Summary**
Noelke, C. *et al* [49]	The authors developed a system capable of producing parts using Micro Selective Laser Melting (SLµM) because, to achieve resolutions below 30 µm, pre-processing has to be done through open lines instead of closed contours as in SLM. The dust deposition system needed to be adapted, because the particles tended to agglomerate due to their small size (<50 µm). Furthermore, they also used a 50 W fiber laser and a telecentric f-theta lens capable of projecting a laser diameter equal to 19,4 µm. After the machine's construction, they did several tests in order to understand which would be the smallest structure diameter achievable. They concluded, after printing a helix structure with 90 µm connections, that this was the best result since it did not break.
Wu, L. *et al* [50]	In this article, the authors studied the properties of an aluminium composite powder and graphene nano-platelets (GNP) that were added in order to improve the wear resistance of the metal. Firstly, the substrates were mixed through a ball mill with 20 minutes cycles and breaking of 10 minutes between each cycle, for a total of 4 hours. Then they printed Al and Al/GNP test pieces on Renishaw's AM400 machine and performed tests to determine the tribological properties of both. They concluded that, with the increase in sliding speed, the friction coefficient decreased, due to the self-lubricating properties of the GNP. In addition, the wear regime changed from abrasive to delamination wear, due to the formation of a stable mixed mechanical film.
Jung, I. D. *et al* [51]	In this scientific paper, the authors investigated the feasibility of printing metallic parts with integrated chips (IC), since, nowadays, one seeks to monitor everything constantly and remotely. That said, they divided the printing of the components of IN 718 and 316L stainless steel into three stages. First, the piece was printed up to the height at which the CI is going to be placed. Then, the existing dust was removed, and the IC was put in place, however, it is covered by a protective layer that was previously printed. Finally, the upper part of the piece was printed. After carrying out tests, they concluded that the mechanical properties, as well as the microstructure of the "smart" parts were comparable with the normal parts printed by SLM. In addition, they proved that the IC was not damaged due to the typical heat of the process, as it was able to send data via Bluetooth and Wi-Fi.

Bibliographic References	**Summary**
Tan, Q. *et al* [52]	Tan, Q. et al studied the influence of Lanthanum Hexaboride (LaB6) nanoparticles when inoculating the AlSi10Mg alloy. To do this, they created a composite powder of aluminium with 0.5 wt.% LaB6 nanoparticles using an ultrasonic vibrator and an electromagnetic shaker in order to obtain a homogeneous mixture. Then, they printed specimens of aluminium powder and composite powder in order to compare the microstructure of both. With that said, they concluded that the addition of LaB6 nanoparticles caused the homogeneous mixture to show significant grain refinement due to the crystallographic atomic matching across the Al/LaB6 interfaces. In addition, the composite powder showed isotropic mechanical properties and greater plasticity when compared to aluminium powder. Finally, the authors recommend the use of this technique to manufacture aluminium alloys that are more complicated to print, namely those of the 2000 and 7000 series.

2.1.3 PARAMETERS

Given the fact that the printing parameters are the same for SLS and SLM, changing only the property values, this topic was written apart from the two technologies.

In Figure 9, it is possible to see the main parameters to be taken into account when manufacturing a component. It is important to note that most parameters are interdependent. For example, the laser power depends on the melting temperature of the material and the temperature at which the powder is. In addition, the absorptivity of the powder bed is influenced by the type of material, shape and size of the particles, which, in turn, also dictate the power of the laser to be used [2].

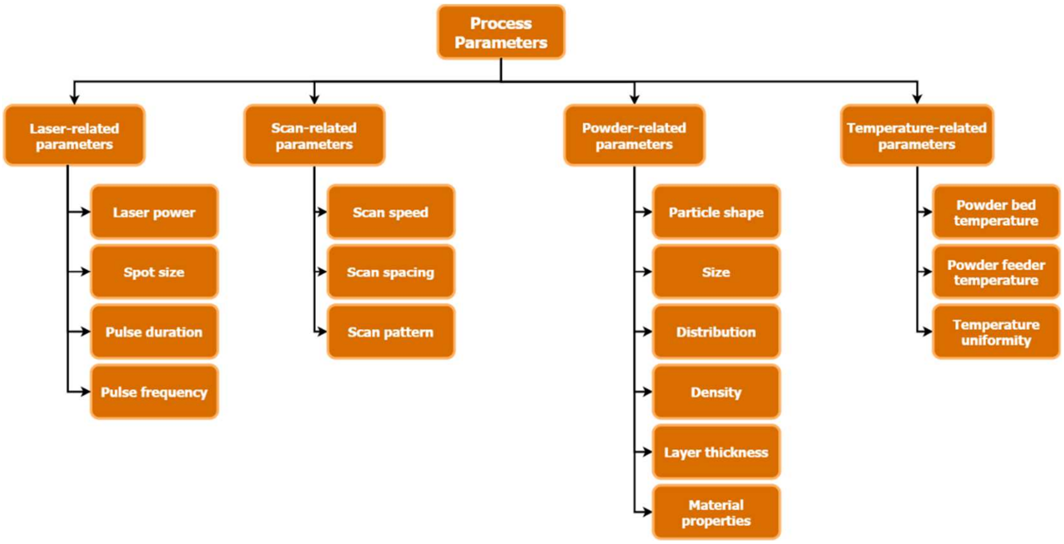

Figure 9 - Parameters of PBF-LB processes. Adapted from: [2]

There are different equations that comprise different process parameters and can be used in order to, theoretically, estimate the value of the property to be used. In Table 10 we have:

Table 10 - Example of equations used to determine printing parameters [53]

Name	Equation	Additional Information
Volumetric energy density	$E_V = \frac{P}{v \times h \times t} \quad [\mathrm{J/mm^3}]$	P – Laser power; v – Laser scanning speed; h – Hatching space; t – Layer thickness.
Linear input energy density	$E_I = \frac{4P}{\pi \times v \times d^2} \quad [\mathrm{J/mm^3}]$	d – Laser spot size.
Surface energy density	$E_S = \frac{P}{v \times d} \quad [\mathrm{J/mm^2}]$	Energy density applied to the powder bed surface.
Linear energy density	$E_L = \frac{P}{v} \quad [\mathrm{J/mm}]$	Defined as the power input per unit speed.
Optimal hatching space	$h = 0{,}7 \times w \quad [\mathrm{mm}]$	w – Beam waist.

The surface is scanned in two ways, first the laser contours the outer shape of the part in order to improve the precision and surface finish, and then scans the interior of the part using various possible patterns. These patterns dictate the path that the laser takes on the component's surface and are responsible for controlling the microstructure and minimizing defects such as warps [54]. In Figure 10, it is possible to see the different strategies followed when scanning the surface of a piece printed by PBF-LB.

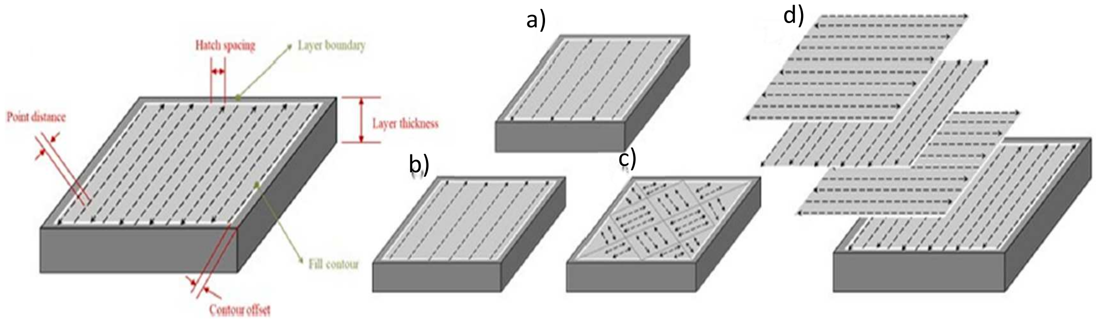

Figure 10 - Different scan patterns: a) meander, b) uni-directional, c) chessboard and d) rotation of the scan orientation with each new layer [54]

In addition, there are numerous studies related to process parameters and how they influence factors such as residual stresses, mechanical properties, and surface finish. Table 11 shows some of them.

Table 11 - Process parameters and their influence on final parts

Bibliographic References	**Summary**
Ali, H. *et al* [55]	The authors investigated the effect that different scan patterns have on the formation of residual stresses and on the mechanical properties of a titanium alloy, as well as the re-scan effect on relieving residual stresses. For this, they printed several specimens with 5 different scanning techniques, namely, meander with 45-degree rotation between each layer, meander with 90-degree rotation between each layer, chessboard, chessboard with 45-degree rotation of the adjacent block and, finally, chessboard with 90-degree rotation of the adjacent block. After comparing the various samples, the researchers concluded that the meander scan strategy with 90-degree rotation for each new layer was the one with the lowest residual stresses, however, they were unable to detect any correlation between the scan patterns and the mechanical properties. Furthermore, re-scanning relieved residual stresses by 33 percent, but the specimens suffered a great deterioration in mechanical properties, so it is not advisable to use this technique on titanium powder.
Nguyen, Q. B. *et al* [56]	In this article, the authors studied the influence of layer thickness on the mechanical properties and dimensional accuracy of the Inconel 718 powder. They printed, on the 3D Systems ProX-300 machine, several specimens with different layer thicknesses, 20, 30, 40 and 50 μm respectively. After having performed mechanical tests and microstructure analysis, they concluded that the specimen with the lowest layer thickness showed the best values for density, microhardness, stiffness and ultimate tensile strength. These results were linked to a bigger formation of strengthening precipitates (γ’ and γ’’) in the grain and matrix joints of specimens with a layer thickness of 20 μm. Finally, the specimens with the lowest layer thickness also obtained distinct microstructures due to different cooling times.
Majeed, A. *et al* [57]	Majeed, A. et al studied the influence of laser power, scanning speed, hatch distance, and overlap rate on the surface quality of $AlSi_{10}Mg$ parts. To do this, they printed several specimens, using different parameters, on the SLM Solutions 280HL machine and then measured the surface roughness on two different faces, using the Mitutoyo Surftest SJ-210 machine. Then, through a regression model and an analysis of the variance results, they concluded that the surface roughness increased with the increase in laser power and obtained an optimal value, which was equal to 0,32 kW. Furthermore, they also determined that the increase in hatch distance caused an increase in

Bibliographic References	Summary
	surface roughness. In contrast, the scanning speed and the overlap rate showed a negative correlation with surface roughness. Finally, they concluded that the optimal parameter values were 0,32 kW for laser power, 0,60 m/s for scanning speed, 35% degree of overlap and 88,7 µm hatch distance.
Tonelli, L. *et al* [58]	In this scientific paper, the authors studied the effect that Laser Energy Density (LED) has on the surface morphology, microstructure, and hardness of a CoCrMo alloy. They started by printing test pieces with the geometry of a parallelepiped, changing some printing parameters between builds. These parameters dictated whether the LED was low (up to 100 J/mm³), medium (100-150 J/mm³) or high (150-270 J/mm³). With that said, they analysed the different samples and concluded that, on the one hand, the specimens with a low LED had a high porosity, very variable macrohardness (18-36 HRC) and a high roughness on the upper surface (7-13 µm). On the other hand, the printed specimens with medium and high LED presented low porosity, uniform values of microhardness (35-37 HRC) and low surface roughness (2,5-5 µm).

2.2 SUPERALLOYS IN ADDITIVE MANUFACTURING

Here, the main superalloys existing in AM will be described, giving a greater emphasis to IN 718, as it is strongly interconnected to this dissertation.

In fact, when it comes to superalloys, we are talking about raw material made specifically for a given manufacturing process, and which is capable of operating in demanding conditions thanks to its excellent service properties [59]. However, in the near future, high entropy alloys and intermetallic compounds will also be used, as they are being studied at the moment [60].

2.2.1 TITANIUM

Titanium alloys have been receiving a special attention from the aerospace industry, thanks to the low specific density and the high melting point of this material (around 1650 °C) [61]. In other words, several companies turn to titanium when they need a light component capable of safely supporting high loads and/or when working temperatures are high [62]. In addition, it is also used with high frequency in medical implants, due to its excellent biocompatibility when in contact with tissues or bones of the human body [63]. Note that this material is quite difficult and expensive to machine, so its use and diffusion in AM is of great interest.

In fact, the titanium alloy most studied by the scientific community and used to manufacture final components is Ti_6Al_4V (UNS R56400) [64]. The crystalline structure of this alloy is composed of a compact hexagonal structure (phase α) and body-centred cubic (phase β). The existence of aluminium and vanadium causes the α and β phases to stabilize, respectively [62]. In general, the microstructure, when depositing material, presents a martensitic phase (α').

Figure 11 - Topological optimization of a gooseneck flap actuation bracket made of Ti_6Al_4V: a) old part, b) new part. Adapted from: [65]

2.2.2 NICKEL

Nickel alloys are often used to produce components that operate at high temperatures, for example, parts of gas turbine engines, because in their chemical composition they contain refractory elements such as tungsten (W), tantalum (Ta) and rhenium (Re). In addition, the microstructure is composed of precipitates from phase γ' in the matrix γ, and this, combined with what has been said previously, makes nickel alloys have excellent thermal and mechanical stability at high temperatures [66].

Usually, the most used and studied nickel alloys today are IN 625 (UNS N06625), IN 718 (UNS N07718), Hastelloy X (UNS N06002) and Waspaloy (UNS N07001).

Figure 12 - Monolithic trust chamber made of IN 718 [67]

INCONEL 718

As it was previously said at the beginning of chapter 2.2, the components manufactured for this thesis are made of IN 718, hence it will be given special attention to this alloy.

First and foremost, IN 718 is a precipitation strengthening alloy and has a Face-Centred Cubic (FCC) γ phase, composed mainly by nickel, chromium, and iron. The γ matrix can be strengthened by precipitating coherent phases, such as γ'' (Ni_3Nb) and γ' ($Ni(Al,Ti)$), however, due to the high segregation susceptibility of niobium (Nb), carbides and undesirable phases tend to appear, like δ (Ni_3Nb) and Laves ($(Ni,Cr,Fe)(Nb,Mo,Ti)$), which degrade mechanical properties if not dissolved by a heat treatment [68]. Nonetheless, as Zhang, D. et al demonstrated, moderate amounts of δ at the grain boundaries are beneficial to the notch sensitivity of the material, however, high amounts detriment the mechanical properties, as it was previously mentioned [69]. In Table 12 is possible to analyse the different crystal structures and shapes of the aforementioned phases.

Table 12 - Crystal structure and shape of the different phases [70]

Phase	Crystal Structure	Shape
γ'	Face-Centred Cubic $L1_2$	Spheroidal
γ''	Body-Centred Tetragonal DO_{22}	Disk
δ	Orthorhombic DO_a	Needle-like / Plate-like
Laves	Cubic or Hexagonal (C14, C15, C36)	Round, island-like

The most typical post-processes employed to improve the mechanical properties of IN 718 parts are HT, HIP, and machining. In fact, parts made of this alloy usually undergo a HT consisting of two different stages. The first is solution annealing (SA), to dissolve the undesired phases, such as carbides and Laves, and promote the dissolution of interdendritic segregation. The second is double aging (DA), as it promotes the formation of the strengthening phases γ' and γ'' [71].

ASTM F3055 [41] standard specifies different heat treatments that can be performed on IN 718 parts produced by AM. In order to reduce the internal porosity, HIP should be done in a temperature range of 1120 to 1185 °C at 100 MPa from 3 to 5h. To relieve residual stresses and promote recrystallization, homogenization (HO) can be carried out at a temperature range of 1050 to 1080 °C for one and a half hours followed by air cooling (AC). AMS 5663 [72] standard states that SA should be performed at 980 °C for 1 hour followed by AC, and DA should be done at 720 °C for 8 hours followed by furnace cooling during 2 hours to a temperature of 620°C, maintained at that temperature for 8 hours and then air-cooled. AMS 5383 [73] recommends a HO treatment at a temperature of 1080 °C for 1,5 hours followed by AC, then SA should be done at 980 °C for 1 hour followed AC, and, after that, a DA treatment can be performed in the same way as the AMS 5663 standard. In addition, AMS 5664E [74] standard specifies that a HIP treatment must be done at 1180 °C with a pressure of 150 MPa for 3 hours followed by furnace cooling, and then HO should be performed at a temperature of 1065 °C for 1 hour followed by AC. After that, a DA treatment can be done at 760 °C for 10 hours, followed by furnace cooling at a rate of 55 °C/h until it reaches 650 °C. Finally, it should be held at that temperature for 8 hours and then air-cooled. In Table 13 it is possible to analyse the influence that different printing parameters have on the microstructure, mechanical properties, porosity and residual stresses of IN 718 parts.

Table 13 – Influence of printing parameters on IN 718

Bibliographic References	**Summary**
Lu, Y. *et al* [75]	In this work, the authors studied the influence of the dimension of island scanning on the mechanical properties, microstructure, and residual stresses. To do this, they started by printing IN 718 specimens with 4 different island scanning areas, 2 x 2, 3 x 3, 5 x 5, and 7 x 7 mm². Then, they analysed the microstructure through an optical microscope and concluded that in the test piece with the smallest scan area, the island sizes and borders were not clearly visible, and cracks were formed, in contrast with all the other ones. Then, they performed mechanical tests and concluded that the mechanical properties of all test pieces were similar. Finally, they studied the residual stresses and found that the smallest ones were found in the 2 x 2 specimen, followed by the 5 x 5, which in turn was followed by the 7 x 7 and 3 x 3. After taking all these factors into account, the researchers concluded that the specimen with a 5 x 5 mm² scan area was the strongest candidate.
Yang, H. *et al* [76]	The authors of this scientific paper wanted to understand the influence of laser power on the formability, mechanical properties, and microstructure of IN 718 parts. That said, they printed several test pieces using different laser powers (500 up to 2000 W) and concluded that, on the one hand, the forming process window (scanning speed and hatch spacing) is narrowed as a consequence of higher laser power, but, on the other hand, the built rate is increased. After analysing the microstructure of the specimens, the researchers concluded that the laser power increase did not change the phase composition, however, coarser γ-dendrites, more Laves phase precipitation, and a finer columnar grain could be obtained under a higher laser power. Finally, and as expected, the laser power increase caused the YS and UTS to decrease due to the greater appearance of the Laves phase.

Bibliographic References	Summary
Moussaoui, K. *et al* [77]	Moussaoui, K. et al main objective was to study the influence of Volumetric Energy Density (VED) on the porosity, microstructure, and mechanical properties of IN 718 parts. For that, they printed 35 cubic specimens varying the laser power, scan speed, and hatch spacing. Subsequently, they measured the surface roughness of the test pieces and concluded that lower laser powers and scan speeds resulted in better roughness values. Then, they studied the microstructure and concluded that the increase in VED made the dendrites longer, tighter, and more orientated along the build axis. In terms of microhardness and tensile mechanical properties, there was no observed effect. Finally, they measured the porosity of the specimens and came to the conclusion that the increase in the VED led to a reduction in porosity.
Wan, H. Y. *et al* [78]	In this scientific paper, the authors sought to understand the influence of the scanning strategy in terms of mechanical properties and microstructure in parts made from IN 718. Therefore, they adopted two different scanning strategies, the first was bidirectional scanning without 90° rotation between successive layers (SS-X) and, the second one, was with 90° rotation between successive layers (SS-XY). After printing the specimens with different scan strategies, they studied their microstructure and mechanical properties and concluded that SS-X specimens showed better tensile strength and fatigue strength than SS-XY. This was due to the refinement of the grain in the SS-X test pieces.

2.2.3 COBALT

These alloys are composed of cobalt, chromium, and a small percentage of molybdenum, and are widely used for biomedical applications, namely dental restorations. They have a σ_y in the order of 600 MPa [79], as well as good resistance to high temperatures. In addition, when calcium monophosphate (CaP) is added, this alloy has excellent corrosion resistance and good biocompatibility and is, therefore, also indicated for joint implants [80]. One of the most used alloys is ASTM F75 CoCr (UNS R30075).

Figure 13 - Knee joint implant, made from ASTM F75 CoCr [81]

2.2.4 ALUMINIUM

The use of these alloys is not as accentuated as those previously mentioned, because, unlike titanium, aluminium is an easy material to be machined, which is why it is advantageous to process it through chip removal processes. Despite its high thermal conductivity, which allows for faster printing and reduces residual stresses, aluminium has some disadvantages. The first is the low boiling point of some alloy elements, such as zinc (Zn), which the Al 7000 series has. This causes the melt pool to be turbulent, resulting in various splashes of material and porosities. In addition, PBF-LB processes are not ideal for making parts of this material, due to its enormous reflectivity over a wide range of wavelengths [64].

The main alloys used are $AlSi_{10}Mg$ (EN AC-43000) and $AlSi_{12}$ (EN AC-44200) because, the addition of silicon results in a melting temperature drop causing a eutectic solidification, making the material easier to process [62].

Figure 14 - Motor housing for an electric race car made from AlSi10Mg [82]

2.2.5 MECHANICAL PROPERTIES

This chapter was created with the purpose of comparing and analysing the most relevant mechanical properties of the alloys mentioned above, as it is shown in Table 14.

Table 14 - Mechanical properties of the main AM superalloys in the as-built state. Source: Datasheets from the annexes

Alloy	**ρ [kg/m³]**	**T_m [°C]**	**σ_y [MPa]** (XY Direction)	**E [GPa]** (XY Direction)	**Hardness [HRC]**
Ti_6Al_4V	4430	1650	950	120	33
IN 718	8190	1300	780	160	30
ASTM F75 CoCr	8300	1400	560	220	34
AlSi10Mg	2680	580	442	71	- (119 HV)

2.3 STRESS MEASUREMENTS

In LB-PBF processes, residual stresses (RS) are induced by thermal principles and they are very usual as the gradient temperature is high because of the heating and thermal expansion upon deposition of a new layer, and subsequent cooling and contraction of it [83]. As a consequence, parts can suffer a great geometrical distortion and cause production errors, thereby, it is crucial to know the expected magnitude and orientation of the RS in order to carry out safe and accurate predictions of the final part properties [84]. In Table 15 is possible to view the distinct classifications of RS and where they act.

Table 15 - Residual stresses classification [84]

RS Classification	Operational Length Scale	Additional Information
Type I	Macroscopic stresses that act on the scale of component geometry.	May cause global distortion. Are the most discussed ones in the literature.
Type II	Microstresses acting at the individual grain scale, often called intergranular stresses.	Form due to local microstructural effects, such as grain to grain differences in slip behaviour.
Type III	Atomic scale residual stresses.	Occur due to vacancies, introduction of substitutional atoms, etc.

The main physical factors that contribute to RS formation on LB-PBF parts are the laser power, scan speed, and layer thickness, which create high-temperature gradients followed by rapid heating and cooling rates (about 10^6 K/s for the Ti6Al4V alloy, according to [85]). In fact, the next layer to be built is deposited on top of the previous one (or substrate), which is at a much lower temperature than the melted material. Just after the deposition, the material is divided into a softer hot zone, known as melted material, and a stronger cold zone, which is the surrounding material. This will generate uneven plastic deformations that will remain accumulated inside the material as residual stresses, Figure 15 [84].

Nowadays, multiple techniques are employed to measure residual stresses and they can be divided into two major groups, destructive, and non-destructive testing. In the following subchapter RS measurement methods will be addressed.

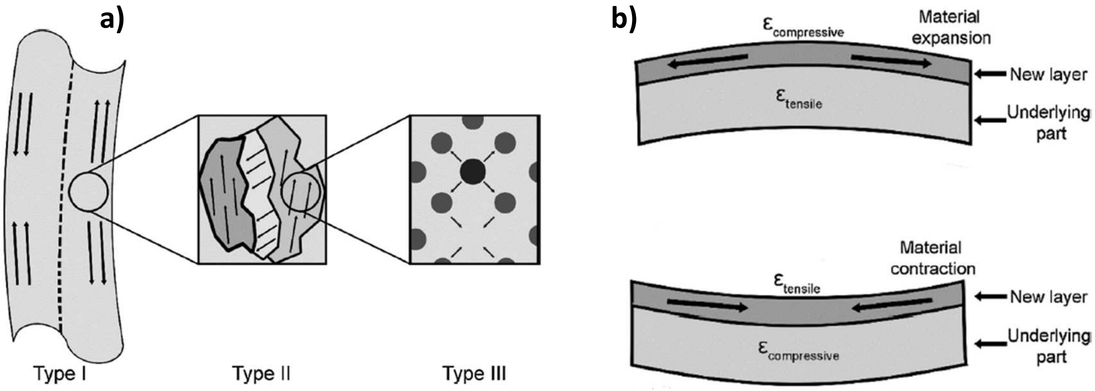

Figure 15 - Residual stresses classification a), and plastic deformation development b). Adapted from: [84]

2.3.1 X-RAY DIFFRACTION

In fact, non-destructive techniques using diffraction methods are divided into three, namely X-ray diffraction (XRD), X-ray synchrotron radiation, and neutron diffraction. However, the most used today is XRD due to its great accuracy (± 20 MPa), as well as the big variety of equipment available [86]. This last method is used to discover residual stresses on part's surfaces, measuring the interplanar spacing *d* through Bragg's law, and comparing it with the non-deformed lattice parameter. Figure 16 shows that residual stresses change the interplanar spacing of the crystal planes.

In order to use this method, the grain size of the piece must be lower than 100 µm, and the best result is achieved when the grain size value is around 30 µm. However, the biggest limitation of this technique is the measurement depth, since it can only reach values of 10-30 µm [86].

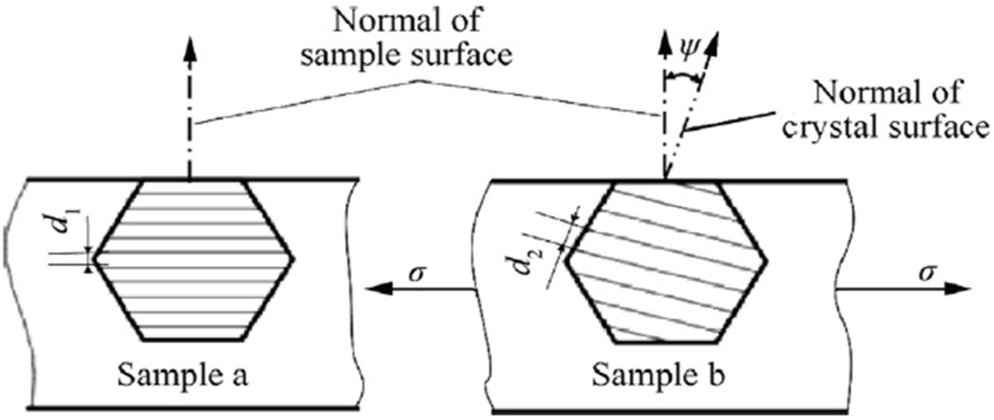

Figure 16 - RS influence on interplanar spacing between crystal planes [86]

2.3.2 HOLE-DRILLING STRAIN-GAGE METHOD

According to ASTM E837-08 standard, the hole-drilling strain-gage method can be described as a technique that “determines residual stresses near the surface of an isotropic linear-elastic material. It involves attaching a strain rosette to the surface, drilling a hole at the geometric centre of the rosette, and measuring the resulting relieved strains. The residual stresses within the removed material are then determined from the measured strains using a series of equations.” [87]. It is considered a semi-destructive method as it does not affect, in a significant way, the structural integrity of the part. In addition, this procedure is different from others since any trained technician, or someone with the help of a guidebook can perform the tests properly. Furthermore, it is also a very versatile method, as it can be performed on laboratory or on-site, and is suitable for different part sizes and shapes.

The precision of this method can be severely affected by the mechanical properties of the tested material, hole alignment and boring, strain gage installation and selection, as well as the data acquisition instrumentation [88]. As it was said previously, the tested material should have isotropic characteristics, however, the Poisson ratio and Young’s modulus should also be known. Moreover, the surface place where the measure is performed must be flat, away from material or geometric discontinuities, and previously cleaned and degreased. The ASTM standard does not recommend abrading or grinding the surface, because these methods may induce residual surface stresses, however, several studies recommend a light use of surface abrasion techniques to improve the surface roughness [88,89]. The rosettes can have different configurations, usually with 3 (Type A and B) or 6 (Type C) individual strain-gages, as exemplified on Figure 17. The rosette selection must take into account the material and thermal stability of the workpiece, and the size and location of the hole, as it will influence the sensitivity of the strain measurement and hole dimension. In order to centre the drill with the rosette, optical devices like microscopes should be used, and then the hole can be done using a carbide burr or endmill (not advisable for hard materials) driven by an electric motor or air-turbine [87].

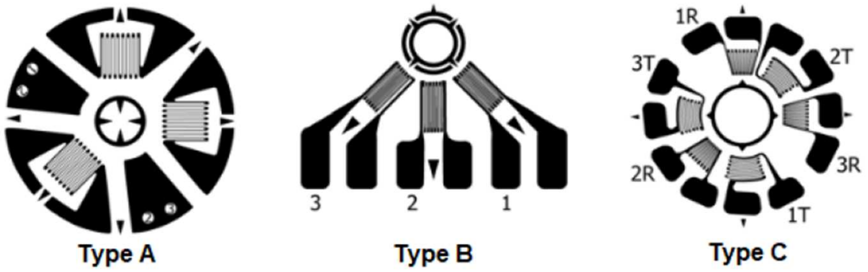

Type A **Type B** **Type C**

Figure 17 - Different types of rosette configurations [87]

2.4 X-RAY COMPUTED TOMOGRAPHY

X-ray computed tomography (CT) is described, according to ASTM E 1441, as "a radiographic method that provides an ideal examination technique whenever the primary goal is to locate and size planar and volumetric detail in three dimensions." [90]. With that said, CT can be seen as an advanced measuring technique that allows a non-destructive examination of macro and micro-scale features, i.e. voids and inclusions, that are inaccessible with other measuring methods. In addition, nowadays it is able to do micro-scaled topographical measurements of re-entrant features and non-accessible surfaces [91].

This method works by irradiating an X-ray beam into a sample that is placed on a rotating stage and the subsequent absorption of the X-ray image is measured through a planar detector, Figure 18. The constant rotation of the sample allows to gather multiple images and then, an integrated software is responsible to reconstruct the volumetric data which comprises voxels. In AM, this technique is widely used to inspect the porosity and build defects in final components, thus allowing to decide whether the part pass or fails [92].

One of the biggest limitations of this technique is, in fact, part size. This becomes especially crucial in high-density metal components and in parts larger than 100 mm, as the penetration of X-rays becomes quite complicated. In addition, the "rule of thumb" is that the best possible resolution for a typical geometrical magnification is 2000 times smaller than the widest place of the component, this means that a 40 mm part has the best possible voxel size of 20 µm. Furthermore, the minimum pore size that can be accurately identified is at least 3 voxels wide, so a scan made at 20 µm voxel size will quantify all pores greater than 60 µm in diameter [92].

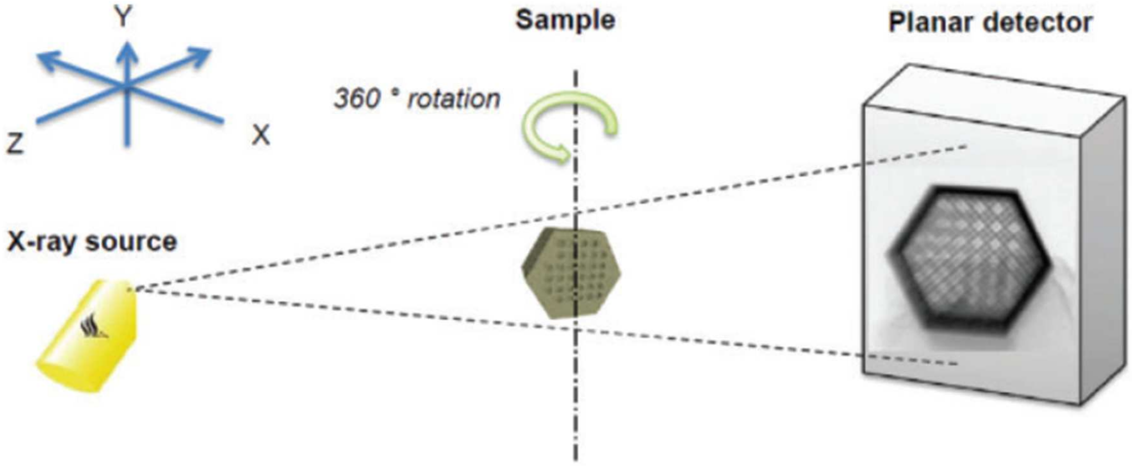

Figure 18 - Principal components of a CT scan machine [92]

Du Plessis, A. et al recommend, as a fast option, the use of 2D X-ray images to inspect several pieces in a batch and, if a defective piece is suspected, do a CT scan with low resolution and quality, in order to see the inside of the defective part. However, if one wants to invest a moderate amount of time in component analysis, such as inclusion or porosity analysis, the authors recommend the use of a witness specimen, made in the same build as the sample, because it allows to have a higher resolution than the part. In addition, if a statistical analysis shows that the witness specimens does not have critical pore sizes, then a pass decision can be made for all the parts of the same build [92].

This technique is very effective in detecting manufacturing defects in parts produced by AM, as Kim, F. H et al demonstrated in [93]. The authors printed three different cylindrical specimens in diameter, as well as in the number, shape, and size of internal features. After a CT analysis, they concluded that the difference between nominal and actual volumes increased as the interior feature size decreased. This was due to the inaccurate production of the top surfaces, as shown in Figure 19.

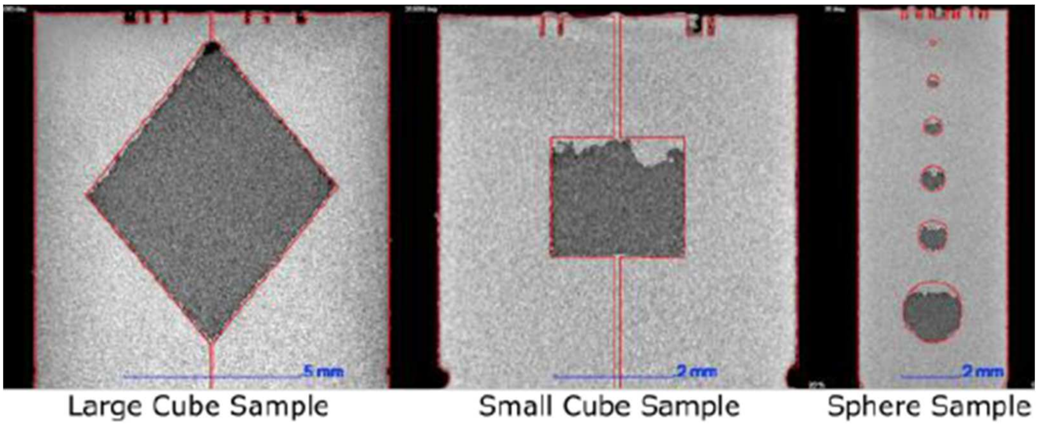

Figure 19 - CT scan of the three different samples printed [93]

THESIS DEVELOPMENT

PAPERS

3 THESIS DEVELOPMENT

The initial goal of this dissertation was to evaluate the thermal treatment effect on the entrapment of Inconel 718 powder in internal channels. To do so, a novel approach was going to be done in which the thermal treatment was split in two, Figure 20.

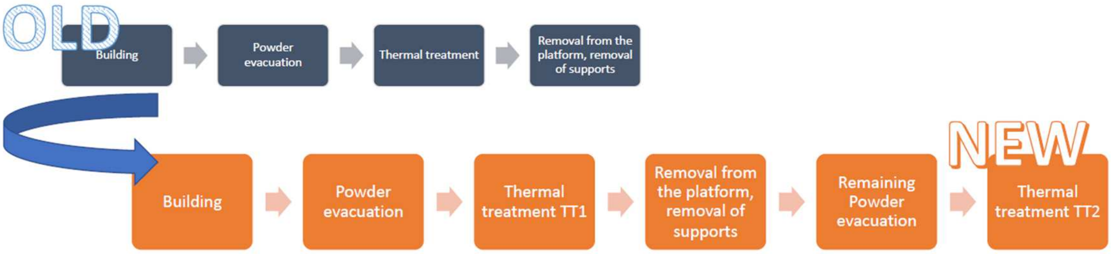

Figure 20 - Novel approach diagram

However, due to the current pandemic, Polito's laboratories can only be used by researchers and PhD students. Having that constraint, I was advised, by Professor Francisco Silva, to write two review papers that would replace the experimental work of this thesis. The aforementioned articles can be seen in the next chapter.

ARTICLE 1: RESIDUAL STRESSES AND HEAT TREATMENTS OF INCONEL 718 PARTS MANUFACTURED VIA SELECTIVE LASER MELTING: AN OVERVIEW ABOUT RECENT DEVELOPMENTS

Residual Stresses and Heat Treatments of Inconel 718 Parts Manufactured via Selective Laser Melting: An Overview About Recent Developments

O. Teixeira · F. J. G. Silva · E. Atzeni

Received: date / Accepted: date

Abstract Additive manufacturing (AM) is a unique manufacturing process that disrupted completely the way which components are made, since this process is capable of producing complex parts layer after layer. As a matter of fact, one of its distinct technologies is Selective Laser Melting (SLM) which is a powder bed fusion process that creates metallic parts with the aid of a high-energy laser beam. One of the most employed superalloys in this technology is the Inconel 718 (IN718), a precipitation-hardened alloy that is used in the marine, nuclear power plants, gas turbines, and aerospace field due to its capacity of retaining good mechanical properties at high temperatures. The research novelty of this review manuscript is the compilation of all kinds of information from the last 15 years of investigation about IN718 parts produced via SLM, namely information related to distinct heat treatments and the influence they have in increasing mechanical properties of the manufactured components, as well as reducing residual stresses (RS) and part porosity. Throughout the review, it can be seen that the expected microstructure in the as-built state is characterized by fine columnar grains and a saturated γ matrix with the presence of the Laves phase and carbides. However, distinct heat treatments can be employed which lead to the dissolution of the undesired phases (Laves and carbides), the precipitation of the strengthening phases (γ’ and γ’’), and the porosity decrease. Furthermore, it was also shown that heat treatments as well as optimized process parameters can be held accountable for lowering the RS of the IN718 manufactured parts. Nevertheless, there are still some problems to overcome, namely the mechanical properties variability when subjecting IN718 powder to different process parameters. Moreover, the RS evolution under different heat treatments needs to be further investigated.

Keywords Additive Manufacturing; 3D Printing; Selective Laser Melting; Inconel 718; Residual Stresses; Heat Treatment; Hot Isostatic Pressing; Microstructure; Mechanical Properties.

O. Teixeira · F. J. G. Silva
ISEP - School of Engineering, Polytechnic of Porto, Rua Dr. António Bernardino de Almeida, 431, 4200-072 Porto, PORTUGAL
Tel.: +351-228340500
Fax: +351-228321159
E-mail: fgs@isep.ipp.pt

E. Atzeni
Dipartimento di Ingegneria Gestionale e della Produzione, Politecnico di Torino, ITALY

1 Introduction

Additive manufacturing (AM) was created in 1981 by Hideo Kodama [1] and can be described, according to the American Society of Testing and Materials (ASTM), as a process that produces components layer after layer from 3D model data [2]. Nevertheless, this manufacturing process is also known by many as three-dimensional printing (3DP), however the former is used for final parts, while the latter is used for prototypes. As a matter of fact, this technology can be seen as a disruptive one, as it completely changed the creation of parts through the addition of material instead of the common subtraction of it, something that is characteristic of subtractive manufacturing [3,4]. According to the aforementioned standard, this new technology can be divided into seven distinct process categories, namely Binder Jetting, Direct Energy Deposition, Material Extrusion, Sheet Lamination, Vat Photopolymerization, and Powder Bed Fusion, Table 1. However, this manuscript will be focused towards the previous category, which can be subdivided into three different technologies, specifically Selective Laser Sintering (SLS), Electron Beam Melting (EBM), and Selective Laser Melting (SLS). The first one, SLS, is mainly used to manufacture polymeric components and uses a laser to sinter the powder layer after layer, while the second, EBM, uses high energy electron beam to melt the powder. The third one, SLM, will be explained in further detail in the next subsection since it is the manufacturing technology that this manuscript focus the most.

1.1 Selective Laser Melting

SLM appeared in 1996 through Wilhelm Meiners, Konrad Wissenbach and Andres Gasser [5]. This technology uses a high-energy laser to fully melt the metallic and it must be done in a chamber surrounded by an inert gas, such as argon or nitrogen, to avoid oxidation of the material after melting, remove spatter, metal vapor, and plasma plumes [6-9]. In addition, the parts are usually connected to a substrate plate by support structures, in order to reduce deformations when printing. The operating method can be described as follows:

- Firstly, on some machines, the build platform is heated in order to reduce deformations caused by temperature differences;
- Then, an actuator rises the powder cartridge and dispenses a predefined amount of metallic powder;
- Next, thanks to the levelling roller, a uniform layer of powder is created on the construction platform and the powder excess is pushed to another cartridge;
- After that, a melt pool of approximately 100 μm in length is formed due to a high energy density laser which melts the powder [10];
- Finally, the construction platform lowers according to the thickness of each layer, which usually varies between 20 and 100 μm depending on the material, and the process is repeated until the final piece is completed [11].

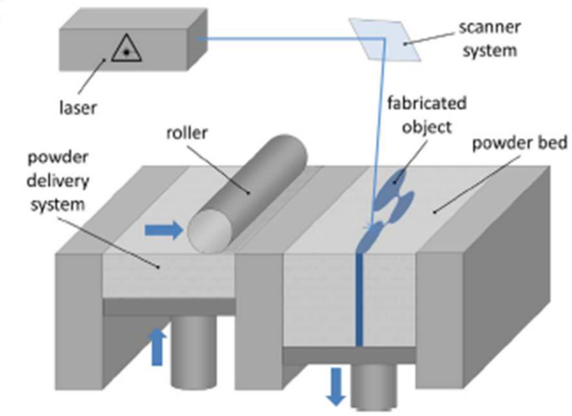

Figure 1 - SLM process schematic figure [12]

1.2 Inconel 718

One of the most used superalloys in AM is the Inconel 718 (IN718), which is a precipitation-hardened alloy and has a Face-Centred Cubic (FCC) γ phase, composed mainly by nickel, chromium, and iron [13]. It can be applied in the marine, nuclear power plants, gas turbines, and aerospace fields due to its capacity of retaining mechanical stability at high temperatures up to ~700 °C [14,15]. In addition, it has an excellent creep resistance, high fatigue strength at elevated temperatures, and a good corrosion resistance as it was reported in several literatures [16-21]. The γ matrix can be strengthened by precipitating coherent phases, such as γ'' (Ni3Nb) and γ' (Ni(Al,Ti)), however, due to the high segregation susceptibility of niobium (Nb), carbides and undesirable phases tend to appear, like δ (Ni3Nb) and Laves (Ni,Cr,Fe)(Nb,Mo,Ti), which degrade mechanical properties if not dissolved by a heat treatment [22].

Nevertheless, as Zhang et al. [23] demonstrated, moderate amounts of δ at the grain boundaries are beneficial to the notch sensitivity of the material. In Table 2 is possible to analyse the different crystal structures and shapes of the aforementioned phases. The most typical post-processes employed to improve mechanical properties, reducing porosity and residual stresses (RS) of IN718 parts are heat treatments (HTs), and hot isostatic pressing (HIP) [25,26].

Table 1 - ASTM Classification [2]

Process Category	Technologies	Materials
Binder Jetting	3D Printing Ink Jetting S-Print M-Print	Ceramic, Metal, and Polymer
Direct Energy Deposition	Direct Metal Deposition Laser Deposition Laser Consolidation Electron Beam Direct Melting	Metal: Wire and Powder
Material Extrusion	Fused Deposition Modelling	Polymer
Material Jetting	Polyjet Ink-jetting Thermojet	Photopolymer
Powder Bed Fusion	Electron Beam Melting Selective Laser Melting Selective Laser Sintering	Ceramic, Metal, and Polymer
Sheet Lamination	Ultrasonic Consolidation Laminated Object Manufacture	Hybrids, Metallic, and Ceramic
Vat Photopolymerization	Stereolithography Digital Light Processing	Photopolymer, and Ceramic

In fact, parts made of this alloy usually undergo a HT consisting of two different stages. The first is solution annealing (SA), to dissolve the undesired phases, such as carbides and Laves, and promote the dissolution of interdendritic segregation [27]. The second is double aging (DA), as it promotes the formation of the strengthening phases γ' and γ'' [28]. Furthermore, ASTM F3055 [29] standard specifies different heat treatments that can be performed on IN 718 parts produced by AM. In order to reduce the internal porosity, HIP should be done in a temperature range of 1120 to

1185 °C at 100 MPa from 3 to 5 hours. To relieve residual stresses and promote recrystallization, homogenization (HO) can be carried out at a temperature range of 1050 to 1080 °C for 1.5 hours followed by air cooling (AC). AMS 5663 [30] standard states that SA should be performed at 980 °C for 1 hour followed by AC, and DA should be done at 720 °C for 8 hours followed by furnace cooling (FC) during 2 hours to a temperature of 620°C, maintained at that temperature for 8 hours and finally submitted to AC. AMS 5383 [31] recommends a HO treatment at a temperature of 1080 °C for 1.5 hours followed by AC, then SA should be done at 980 °C for 1 hour followed by AC, and, after that, a DA treatment can be performed in the same way as recommended in AMS 5663 standard. In addition, AMS 5664E [32] standard specifies that a HIP treatment must be done at 1180 °C with a pressure of 150 MPa for 3 hours followed by FC, and then HO should be performed at a temperature of 1065 °C for 1 hour followed by AC. After that, a DA treatment can be done at 760 °C for 10 hours, followed by furnace cooling at a rate of 55 °C/h until it reaches 650 °C. Finally, it should be held at that temperature for 8 hours and then air-cooled.

Table 2 - Crystal structure and shape of the different phases [24]

Phase	Crystal Structure	Shape
γ'	Face-Centred Cubic L12	Spheroidal
γ''	Body-Centred Tetragonal DO22	Disk
δ	Orthorhombic DOa	Needle-like / Plate-like
Laves	Cubic or Hexagonal (C14, C15, C36)	Round, island-like

In the selective laser melting process, RS are induced by thermal principles and they are very usual as the gradient temperature is high because of the heating and thermal expansion upon deposition of a new layer, and subsequent cooling and contraction of it [33]. Consequently, component geometrical distortion might occur and originate production errors. Therefore, one should determine and understand the expected magnitude and orientation of the RS in order to do predict, in a trustworthy way, the final part properties. They can be divided into three different types of residual stresses, Type III, II, and I, depending on the operational length scale, Figure 2. Type III act at the atomic scale of the component, Type II, often called intergranular stresses, are micro-stresses acting at the individual grain scale, and Type I are macroscopic stresses that act on the scale of component geometry [34]. Nowadays, multiple techniques are employed to measure residual stresses and they can be divided into two major groups, destructive, and non-destructive testing. In one hand, if the goal is to investigate internal residual stresses in a destructive way, one can use the crack compliance method, the stripping method or the contour method. On the other hand, X-Ray Diffraction (XRD) is one of the most suitable techniques to find residual stresses located on the surface level in a non-destructive way due to its great accuracy (± 20 MPa), and the large variety of equipment available [35]. Moreover, if one seeks to discover RS in a semi-destructive and more economical way, the hole-drilling strain-gage method is the way to go. The latter can be considered a semi-destructive technique as it does not affect the structural integrity of the part in a significant way. According to ASTM E837-08 [36] standard, the aforementioned method computes RS near the surface of isotropic linear-elastic materials. The technique can be described as follows:

- The strain rosette is attached to the surface of the component;
- Then, a hole is drilled at the geometric centre of the rosette, and the resulting relieved strains are measured;
- Finally, the RS within the removed material are then determined using a series of equations.

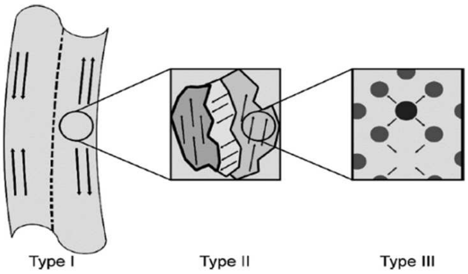

Figure 2 - Residual Stresses classification [34]

Another relevant topic which directly influences the quality and geometry of the final parts is the characteristics of the powder. For example, Aboulkhair et al. [37] reported that powder morphology, composition, surface characteristics, and size distribution influenced the defect formation of additively manufactured parts. In another study, Cunningham et al. [38] indicated that the feedstock powder pores were correlated to the porosity degree of the manufactured components. Similarly, Panwisawas et al. [39] stated that the entrapped gas in the feedstock led to pore formation upon sample manufacturing. Moreover, powder flowability is directly impacted by the powder morphology, which, consequently, influences the spreading uniformity of the layer during production [40,41]. It is also worth mentioning that re-used powders often suffer a quality reduction in terms of particle sphericity, internal porosity, and surface roughness, which, eventually, leads to quality deterioration of the printed parts [42-44]. In addition, Zhao et al. [45] studied the influence of the IN718 powder in the defect suppression of additively manufactured components. For that, the researchers used two distinct powders, namely spherical and imperfect spherical. According to Figure 3, the former possessed a higher circularity as well as more compact binomial distribution in terms of particle diameter, when compared to the latter. Besides, the authors also measured the void volume fraction of both powders and ascertained that the spherical one exhibited a lower value (0.0061 %) than the imperfect spherical (0.0325 %). Then, after printing the specimens, the researchers concluded that spherical powder had a broader process window suppressing defect than the imperfect one. Furthermore, the forming quality of the specimen built with the imperfect powder, and optimal processing conditions, was inferior to the spherical one.

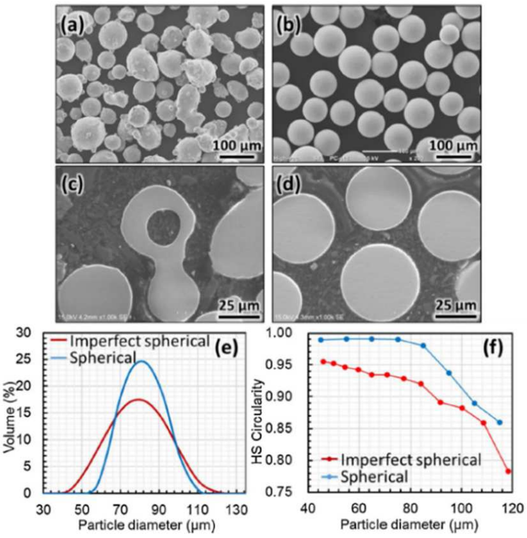

Figure 3 - Imperfect spherical powder can be seen in image a) and c), while spherical powder is represented in b) and d). Image e) represents the binomial distribution of the powder's particle diameter, while f) shows the circularity of the distinct powders [45]

The research novelty of this review manuscript is the compilation of all kinds of information from the last 15 years of investigation about IN718 parts produced via SLM in a structured way, namely information related to distinct heat treatments and the influence they have in increasing mechanical properties of the manufactured components, as well as reducing residual stresses (RS) and part porosity. The authors strongly believe that the compilation of the aforementioned data is essential because the diffusion of additive manufacturing to produce geometrical complex components for demanding industries is growing, and the IN718 is one of the most used superalloys of this technology. Besides, the interpretation of this manuscript will allow the reader to understand the research evolution of this nickel alloy.

At the same time, it provides a good starting point for those who want to learn about additive manufacturing since the essential information about heat treatments and their influence on residual stresses, which can be harmful to the component's life, is discussed in detail. Lastly, this review paper can also be useful to understand some key aspects (i.e. microstructure and mechanical properties) of the IN718 alloy, thus improving the quality and performance of the manufactured parts.

The paper is divided into four different sections, in which the first introduces the topic and indicates the main motivations for carrying out this work. Section 2 discusses the methodology used to search and compile information related to the topic. In section 3, a literature review is performed which aims to address heat treatments and residual stresses of IN718 parts. Finally, section 4 lists the main ideas from this work and makes a description of future perspectives on this field.

2 Methodology

The methodology followed in this article started with the selection of the theme, which is Heat Treatments and Residual Stresses on SLMed IN718 parts. In this way, the authors tried to analyse the amount of information available on the B-On platform in order to get a general idea of the number of articles published on this topic. When performing an advanced search by title, abstract, and keywords on the topics "Additive Manufacturing + Inconel 718", 291 articles were found since 2005, Figure 4.

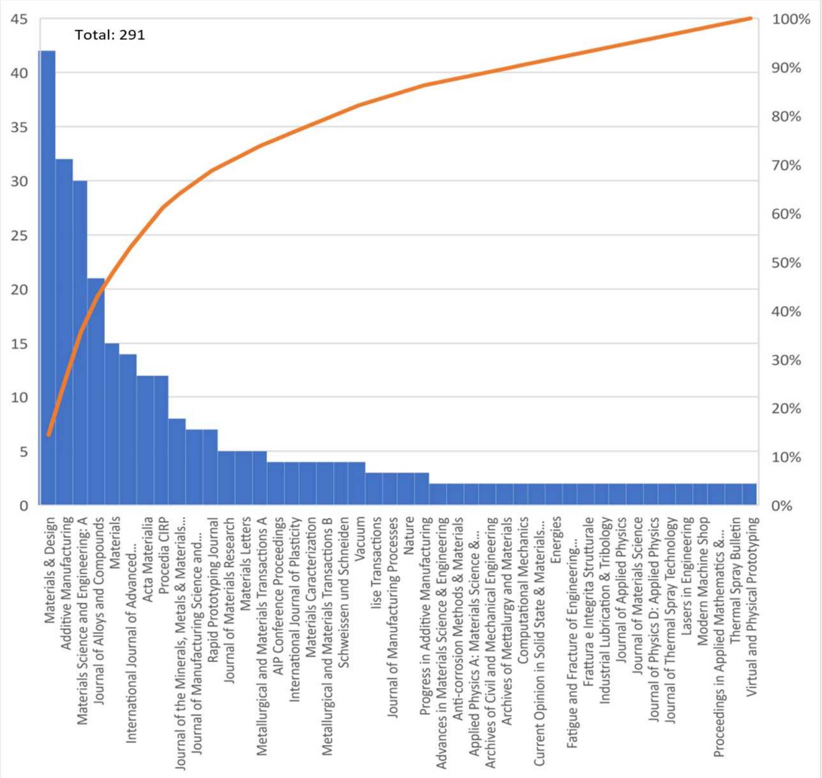

Figure 4 - Pareto's chart of the research "Additive Manufacturing + Inconel 718" on the B-On platform

Then, after a thorough research for the topics "Heat Treatments + Selective Laser Melting + Inconel 718", Figure 5, it was concluded that the number of results had decreased considerably, with a total of 102 research articles. After that, the authors searched for "Residual Stresses + Selective Laser Melting + Inconel 718", Figure 6, and found that there were only 25 research articles. Note that, if the research had not been done in an advanced way, the results would have been much higher, however, more than 50 % of the results would not be relevant for this review article.

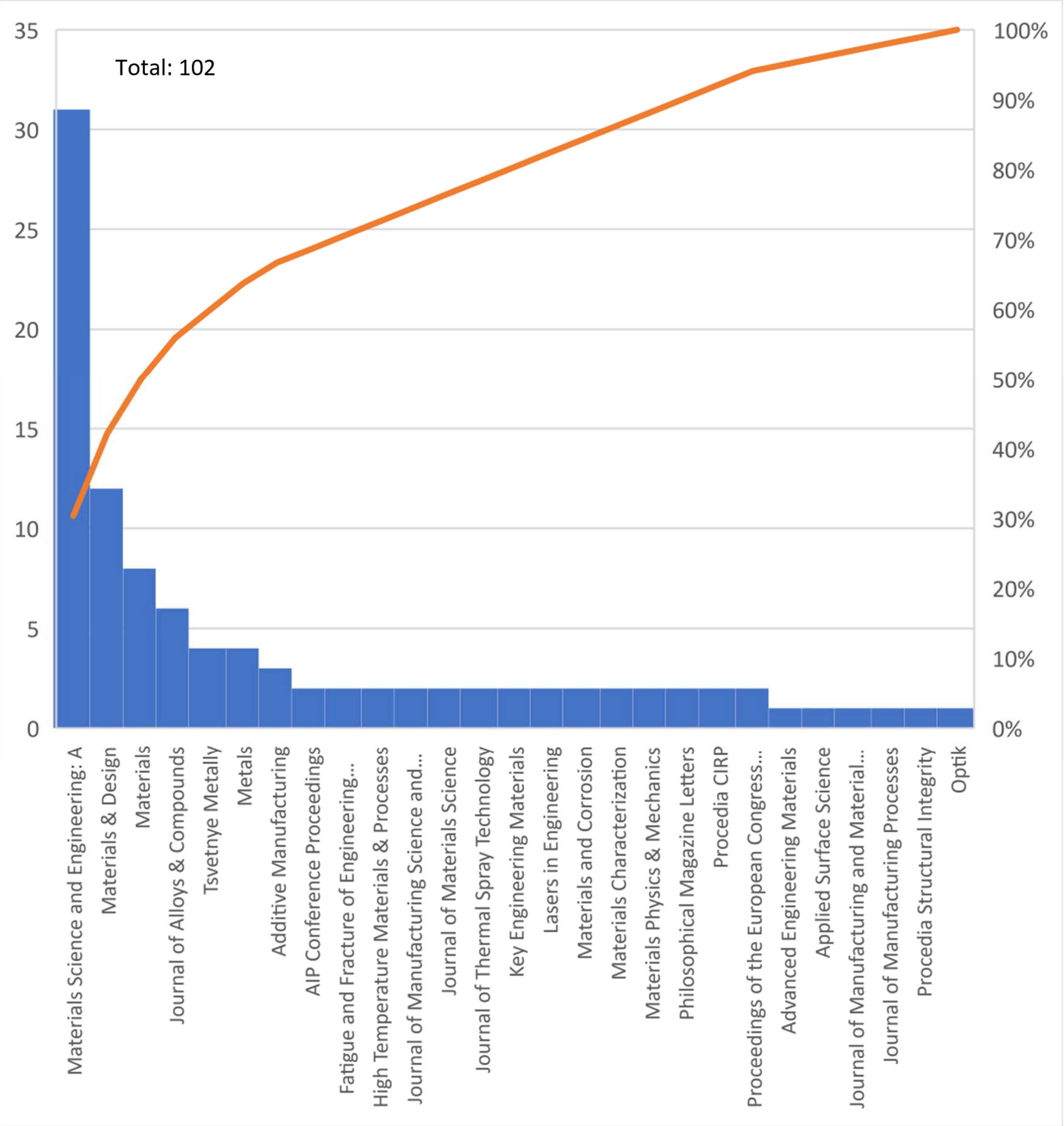

Figure 5 – Pareto's chart of the research "Heat Treatment + Selective Laser Melting + Inconel 718" on the B-On platform

Subsequently, scientific articles were read as well as master's/doctoral theses, and, within them, the authors sought more relevant information for this review work. Then, after acquiring all the necessary information, it was defined two subsections within the literature review, namely heat treatments, and residual stresses. Finally, the authors started writing this report summarizing the main ideas taken from what they read.

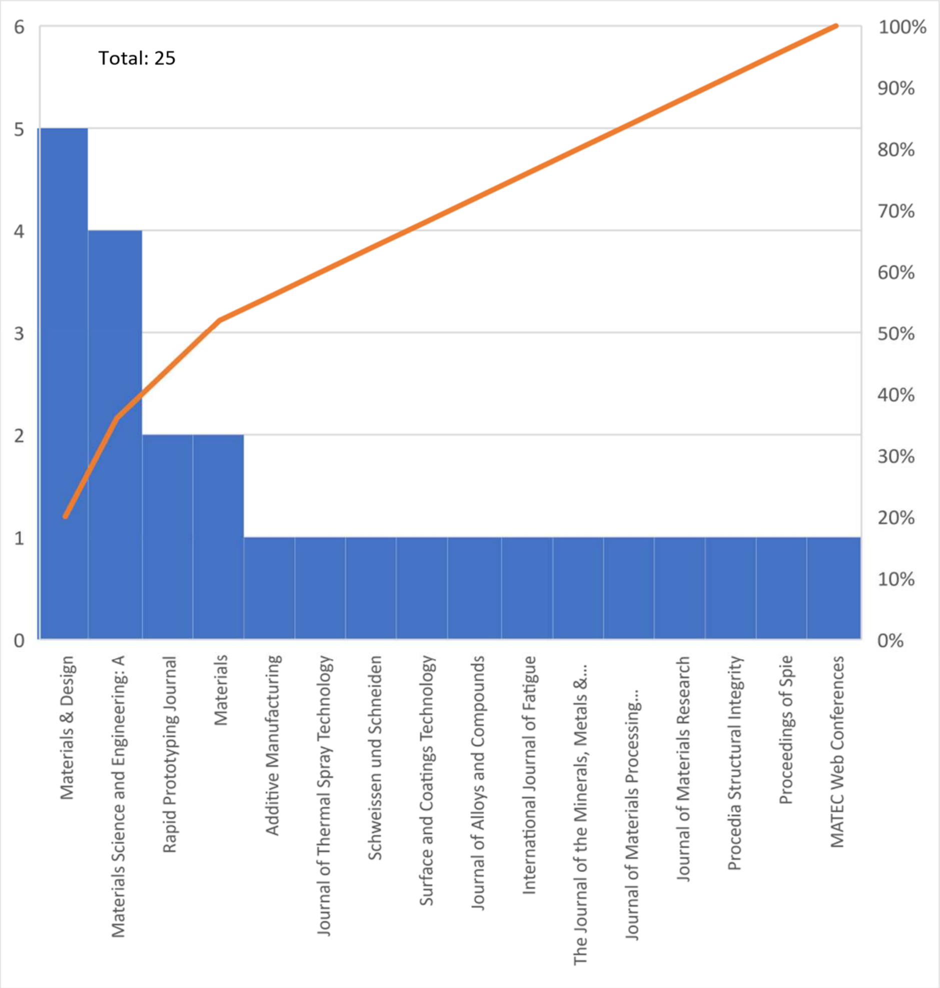

Figure 6 - Pareto's chart of the research "Residual Stress + Selective Laser Melting + Inconel 718" on the B-On platform

3 Literature Review

As it was previously said, the literature review is divided into two main section, which are heat treatments and residual stresses. Regarding the first section, the authors will start to discuss the as-built microstructure, then will move to the SA treatment, subsequently will introduce the DA treatment, followed by the HO variable. Then, HIP treatments will also be reviewed. Regarding the second section, the authors will start to dissect the reason why RS are formed, and then will discuss suitable scan strategies and process parameters that lower the aforementioned stresses. Furthermore, compressive and tensile residual stresses will also be discussed, as well as the RS computation through Finite Element Modelling (FEM).

3.1 Heat Treatments

Heat treatments are greatly known for helping increase the mechanical properties such as yield and ultimate tensile strength, as well as to reduce porosity and residual stresses of IN718 components. Moreover, Calandri et al. [46] reported that the SLM additive manufactured IN718 should not be applied in the as-built state as the microstructure showed heterogeneities, large quantity of brittle precipitates distributed unevenly, and micro-segregation of alloying elements. The researchers also discovered that when the temperature reached 565 °C there was the formation of γ' particles, while a large precipitation of γ'' particles occurred at 740 °C.

In another study, Tucho et al. [47] investigated the effect of the solution heat treatment on the hardness and microstructure of SLMed IN718 parts. The aforementioned treatment was applied with two different temperatures (1100 °C and 1250 °C) and duration (1 and 7 hours). Regarding the microstructure, the researchers concluded that the samples heated at 1100 °C for 1 hour initiated but did not complete recrystallization since the holding time was low, so it was possible to see the typical as-built microstructure. When the duration time was increased from one to seven hours, the specimens showed near-complete recrystallization because the grain was coarser, in addition, the Laves phase was dissolved. Moreover, the authors showed that the microstructure of the 1250 °C/1 h and 1250 °C/7 h was similar, with full recrystallization and a coarser grain. However, the estimated diffusion length of Nb was far superior in the 1250 °C/7 h heat treatment. In terms of hardness, the best result was achieved in the 1100 °C/1 h specimen, as the duration and temperature were proven responsible for the hardness decrease. Calandri et al. [48] studied the influence of time and temperature of the SA treatment on the microstructure of SLMed IN718 samples, having in mind that the aforementioned heat treatment would dissolve the interdendritic precipitates and reduce the segregation of heavy elements such as Niobium. To do so, the researchers conducted a SA treatment in which the temperature ranged from 980 °C up to 1200 °C and the time varied from 1 to 2 hours. After carrying out microstructural tests, the authors concluded that at a temperature of 980 °C the formation of the δ phase is unavoidable as the solvus temperature of the phase is higher. In addition, the researchers reported that the SA treatment should not be performed at 1200 °C since it led to severe grain coarsening which, eventually, leads to mechanical properties loss. To conclude, they found that the advisable SA temperature was 1065 °C with a soaking time of 2 hours as it led to a great dissolution of the as-built precipitates without having an imprudent grain growth.

In a distinct manuscript, Cao et al. [49] studied the effect of the SA + DA treatment on precipitation and microstructure of IN718 specimens manufactured via SLM. The first heat treatment was carried out under a temperature of 1065 °C for 1 hour and then air-cooled. The second heat treatment required a temperature of 760 °C for 10 hours followed by FC for 2 hours, then held at 650 °C for 8 hours and finally air-cooled until it reached room-temperature. After performing a scanning electron microscope (SEM), Figure 7, transmission electron microscope (TEM), and X-Ray Diffraction (XRD) analyses, the authors concluded that, due to the heat treatments, both γ' and γ'' phase precipitated within the cellular γ matrix. In addition, the researchers found coarser acicular γ'' precipitates at the grain boundaries as well as plate-like and globular δ precipitates.

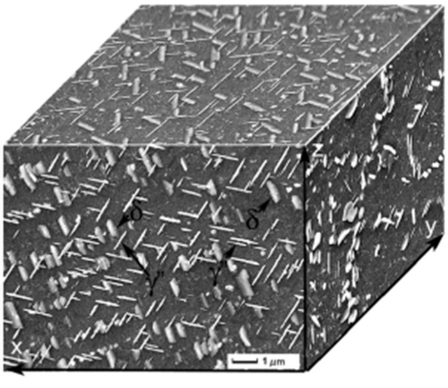

Figure 7 - Composite 3D SEM image of the microstructure of a heat-treated specimen at the vertical (xz and yz) and horizontal (xy) planes [49]

Likewise, Feng et al. [50] studied the effect of the SA + DA treatment on the hardness, microstructure, phase transformation and precipitates of SLMed IN718 specimens. After analysing the microstructure of the SA + DA specimens, they concluded that the heat treatment promoted the disappearing of the columnar crystals and fine dendrites typically seen in the as-built state. Furthermore, the microstructure exhibited a homogeneous bulk crystal structure, and a dissolution of some intermetallic compounds and hardening phases such as Ni-Cr-Co-Mo were also seen. In addition, the solution treatment promoted the precipitation of the δ phase at the grain boundaries and the surface hardness of the as-built specimens was similar to the heat-treated specimens.

Komarasamy et al. [51] investigated the heat treatment effect on impact toughness, microstructure, and fatigue of IN718 manufactured via selective laser melting. The specimens were subjected to SA at 954 °C for 1 hour followed by AC, and then DA at 718 °C for 8 hours followed by furnace cooling until they have reached 621 °C, held at that temperature for 18 hours, and finally air-cooled. After the microstructure analysis, the authors reported that, in this case, the heat treatment did not promote recrystallization, hence it was possible to see a coarse columnar grain structure, as well as a low fraction of Laves phase along with excessive precipitation of δ phase in interdendritic-regions, grain boundaries, grain interior, and sub-grain boundaries. In addition, Komarasamy et al. [51] also identified γ' and γ'' phase precipitates which contributed to the hardness increase of the specimens. After mechanical tests, the authors concluded that fatigue properties were similar to wrought IN718 and also the severe presence of δ phase led to local microstructure-controlled crack propagation. In another report, Huang et al. [52] studied the influence of the time, temperature and cooling rate of SA and DA treatment on the mechanical properties and microstructure of SLMed IN718 specimens. For that, the researchers carried out fourteen different heat treatments, Table 3, in which they varied the SA temperature from 980 °C up to 1280 °C for different times and cooling rates, in addition the DA temperature ranged from 620 °C to 770 °C for 2 to 14 hours. After studying the microstructure and comparing the different results of the heat-treated specimens, the authors came to the conclusion that the ductility and precipitation of strengthening phases in the DA treatment could be improved by the Laves phase dissolution. Furthermore, the precipitation of strengthening phases in the solution treatment was increased when the cooling rate was decreased. Moreover, the HT4 (direct DA at 720 °C/8 h + 620 °C/8 h, AC) was the one which had the best yield and ultimate tensile strength, while the best elongation was achieved in HT10 (SA at 1080 °C/45 min, WQ). To conclude, the researchers came to an equation that relates the minimum solution time to the solution temperature.

$$t = \frac{1}{3266} exp \frac{21642}{T} \qquad (1)$$

Table 3 - Heat treatment influence on the mechanical properties [52]

Sample	SA Processing Condition	DA Processing Condition	YS [MPa]	UTS [MPa]	ε [%]
HT1	980 °C/1 h, AC	720 °C/8 h + 620 °C/8 h, AC	1207 ± 12	1471 ± 4	18,9 ± 1,3
HT2	1080 °C/1 h, AC	720 °C/8 h + 620 °C/8 h, AC	1369 ± 17	1529 ± 19	18,6 ± 0,9
HT3	1130 °C/1 h, AC	720 °C/8 h + 620 °C/8 h, AC	1337 ± 2	1500 ± 1	19,8 ± 1,2
HT4	None	720 °C/8 h + 620 °C/8 h, AC	1374 ± 14	1545 ± 10	14,1 ± 0,7
HT5	1080 °C/45 min, AC	720 °C/8 h + 620 °C/8 h, AC	1361 ± 12	1509 ± 4	20,4 ± 1,3
HT6	1080 °C/3 h, AC	720 °C/8 h + 620 °C/8 h, AC	1260 ± 17	1458 ± 10	21,4 ± 1,2
HT7	1080 °C/5 h, AC	720 °C/8 h + 620 °C/8 h, AC	1248 ± 25	1457 ± 9	22,0 ± 0,8
HT8	980 °C/2h 40 min, AC	720 °C/8 h + 620 °C/8 h, AC	1354 ± 9	1506 ± 6	15,8 ± 2,9
HT9	1080 °C/45 min, FC	None	1037 ± 19	1329 ± 3	27,8 ± 1
HT10	1080 °C/45 min, WQ	None	541 ± 10	976 ± 5	39,1 ± 0,3
HT11	1080 °C/45 min, FC	720 °C/8 h + 620 °C/8 h, AC	1268 ± 8	1476 ± 6	17,9 ± 1,4
HT12	1080 °C/45 min, WQ	720 °C/8 h + 620 °C/8 h, AC	1306 ± 7	1475 ± 11	22,2 ± 0,6
HT13	1080 °C/45 min, AC	700 °C/12 h + 620 °C/6 h, AC	1356 ± 15	1500 ± 5	20,8 ± 1,4
HT14	1080 °C/45 min, AC	700 °C/4 h, AC	1172 ± 5	1414 ± 3	23,8 ± 1,0

Clebus et al. [53] studied the heat treatment effect on the microstructure and mechanical properties of SLMed IN718 samples. The authors exposed the specimens to three different variants of SA treatment in which the temperature ranged from 980 °C up to 1100 °C for 1 hour and then water-cooled. The second step of the heat treatment for all the variants consisted in DA at 720 °C for 8 hours followed by furnace cooling at 100 °C/h rate until it reaches 620 °C, then held at that temperature for 10 hours and finally AC. After analysing the microstructure of the specimens, the researchers concluded that the heat treatments did not change completely the crystallographic orientation and the elongated shape of the solid solution grains. In addition, mechanical properties such as yield, and ultimate tensile strength were enhanced due to the DA treatment.

Gao et al. [54] analysed the δ phase effect on the mechanical performances at high temperature of IN718 specimens manufactured via selective laser melting. For that, the authors employed three distinct heat treatments to the specimens, namely SA (1080 °C for 1.5 hours followed by FC) + DA (720 °C for 8 hours followed by FC at a rate of 55 °C /h until it reaches 620 °C, then held at that temperature for 8 hours and finally FC), SA (980 °C for 1 hour followed by FC) + DA as described before, and SA (1080 °C for 1.5 hours followed by FC + 980 °C for 1 hour and furnace-cooled until room-temperature) + DA. After the high temperature tensile tests the researchers evidenced that the SA (1080 °C + 980 °C) + DA specimen had the highest yield and ultimate tensile strength, followed by the SA (1080 °C) + DA specimen, then the SA (980 °C) + DA, and finally the as-built coupon. However, the authors also reported that the heat treatments decreased the elongation at break of the specimens. In addition, the SA (1080 °C) + DA coupon exhibited a fine columnar grain with no precipitation of the δ phase. Furthermore, the SA (980 °C) + DA specimen showed a large proportion of the δ phase, which explains the lowest value of tensile strength between the heat-treated specimens. To conclude, the SA (1080 °C + 980 °C) + DA specimen showed a moderate precipitation of the δ phase along the grain boundaries which explains the highest value of yield and ultimate tensile strength. Likewise, Wang et al. [55] investigated the mechanical properties and microstructure of SLMed IN718 parts before and after heat treatment, in order to identify the benefits of it. Thus, some of the specimens underwent a solution treatment at 980 °C for 1 hour, followed by air-cooling and then doubled aged for 720 °C for 8 hours, furnace-cooled until it reached 620 °C, then held at that temperature for 8 hours and finally AC, while others remained in the as-built state. After the referred heat treatment, the microstructure evolved from fine to large grains with the precipitation of the δ phase at the grain boundaries, Figure 8. However, the Laves phase could not fully dissolve because the solution temperature was low. In terms of mechanical properties, the heat-treated specimens had a better yield and ultimate tensile strength than the as-built ones, nevertheless, the elongation at break and Young's modulus was higher in the latter than the former.

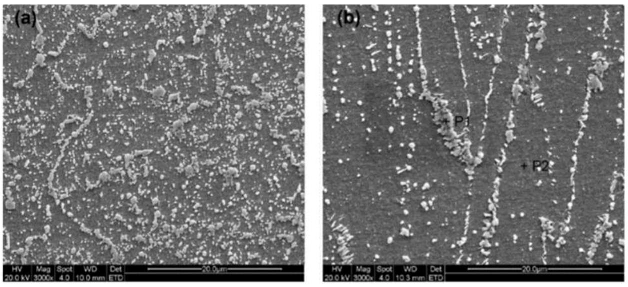

Figure 8 - SEM micrograph of the microstructure of a heat-treated specimen, a) cross section, b) vertical section [55]

Zhang et al. [56] investigated about the influence of heat treatments on the pitting corrosion of selective laser melted IN718 components. The researchers employed three distinct heat treatments, namely SA for 2 hours followed by air-cooling + DA at 720 °C for 8 hours, then cooled until 620 °C and held at this temperature for 10 hours, followed by FC. The only changed variable between them was the SA temperature (1040 °C, 1100 °C, and 1200 °C). After conducting a corrosion test in a electrochemical test cell, the authors concluded that the heat treatments performed with the two lowest SA temperatures had a high pitting corrosion resistance and a relative low corrosion rate because of the precipitation of the γ' and γ'' phases on the γ matrix, as well as the residual stress relief. Furthermore, the SA treatment at 1200 °C promoted the carbide formation in the bulk matrix and the depletion of Cr and Mo, which caused a very weak pitting corrosion.

In a different report, Liu et al. [57] investigated the effect of the heat treatments on the microstructure evolution and phase transformation of SLMed IN718 specimens. For that, they conducted three different treatments, including a direct double aging performed at 720 °C for 3 hours then air-cooled until 620 °C and held at that temperature for 3 hours followed by AC, a SA at 950 °C for 1 hour followed by AC + DA, and lastly a SA at 1050 °C for 3 hours followed by AC + DA as described earlier. After a microstructural study, the authors concluded that the first heat treatment transformed the columnar and small dendritic crystals into bulk crystals as well as allowed the precipitation of the δ phase in the crystal grain. In addition, the temperature rise in the SA treatment promoted an excessive precipitation of the δ phase in the grain interiors and boundaries, Figure 9.

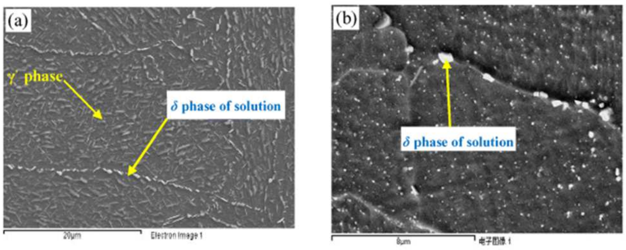

Figure 9 - SEM image of typical precipitates, a) SA at 950 °C + DA, b) SA at 1050 °C + DA [57]

Zhou et al. [58] studied the heat treatment influence on the microstructure and mechanical properties of additively manufactured IN718 samples. In Table 4 is possible to analyse the different heat treatments conducted, as well as the mechanical properties achieved in each treatment. The authors reported that the as-built specimens showed a columnar dendritic or fine cellular microstructure due to the rapid cooling rate of the manufacturing process, in addition carbides and Laves phase were also visible. Furthermore, the authors also concluded that the solution temperature of 1065 °C was the only one able to dissolve completely the Laves phase, resulting in carbide growth. To conclude, Zhou et al. [58] also ascertained that the solution treatment reduced the hardness of the specimens, however the double aging treatment increased it significantly. Similarly, Li et al. [59] investigated the heat treatment effect on the microstructural evolution of IN718 specimens manufactured by SLM. For that, three distinct heat treatments were conducted, namely DA (760 °C for 10 hours followed by furnace cooling at a rate of 55 °C/h until they have reached 650 °C then held at that temperature for 8 hours and finally air-cooled), HO (1065 °C for 1.5 hours followed by AC) + DA as described above, and SA (980 °C for 1 hour then AC) + DA, Figure 10. After optical microscopy, XRD, TEM, and SEM analysis of the microstructure, the researchers concluded that the HO + DA and SA + DA treatments eliminated the Nb and Ti micro-segregations. In addition, the former heat treatment promotes the γ' phase precipitation (18 vol.%) while the latter stimulates the γ'' phase precipitation (29 vol.%). Furthermore, the δ phase precipitated at the grain boundaries in the SA + DA treatment, while in the HO + DA was dissolved into the γ matrix. To conclude, the direct DA treatment only promoted the precipitation of the δ phase in the interdendritic regions.

In another report, Deng et al. [60] studied the effects of post heat treatments on the microstructure of IN718 specimens manufactured via selective laser melting. To do so, the researchers conducted four different types of heat treatments, namely DA (720 °C for 8 hours followed by furnace cooling at a rate of 50 °C/h until it reaches 620 °C, then held at that temperature for 8 hour an finally air-cooled), SA (980 °C for 1 hour then water-cooled) + DA, HO (1080 °C for 1 hour then water-cooled) + DA, and HO + SA + DA as described above. After analysing the microstructure of the heat-treated specimens, the authors concluded that both γ' and γ'' phases precipitated, and the Laves phase was dissolved. However, the HO + SA + DA specimens exhibited a large quantity of δ phase which is responsible for forming large voids that lead to further propagation of the cracks. In addition, the heat-treated specimens showed a significant increase of strength while the ductility decreased correspondingly. According to the researchers, this was due to the partial/complete removal of residual stresses

Table 4 - Distinct heat treatments conducted and mechanical properties [58]

Sample	SA Processing Condition	DA Processing Condition	Young's Modulus [GPa]	Vickers Hardness [HV10]
As-built	None	None	208 ± 7.7	296 ± 2.9
HT1	None	720 °C/8 h + 620 °C/8 h	226 ± 8.6	467 ± 4.3
HT2	980 °C/1 h	None	193 ± 7.7	267 ± 2.1
HT3	980 °C/1 h	720 °C/8 h + 620 °C/8 h	209 ± 6.0	458 ± 4.2
HT4	1065 °C/1 h	None	181 ± 9.0	235 ± 4.2
HT5	1065 °C/1 h	720 °C/8 h + 620 °C/8 h	226 ± 6.3	477 ± 6.6

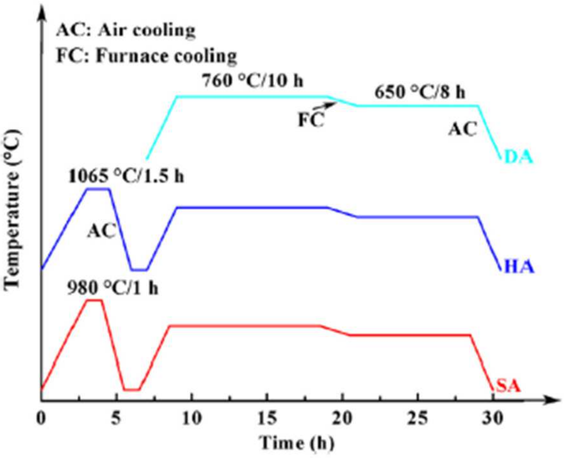

Figure 10 - Schematic representation of the employed heat treatments, namely double aging (DA), homogenization + double aging (HA), and solution + double aging (SA) [59]

Zhao et al. [61] investigated the influence of three different heat treatments on the tensile properties at room- and high-temperature of SLMed IN718 specimens. The post-processes consisted in a HO + SA + DA treatment (1080 °C for 1.5 hours then water-cooled + 980 °C for 1 hour followed by water cooling + 720 °C for 8 hours followed by furnace cooling at 55 °C/h rate until it reaches 620 °C and then kept at that temperature for 8 hours and finally AC), a SA + DA treatment, and DA as described earlier. Then, the authors proceeded to do the tensile tests at room-temperature and discovered that on one hand, the as-built specimens had the best total elongation (almost 30 %) opposed to the double-aged specimens (nearly 7,5 %), on the other hand the last specimens obtained the best yield strength (~1350 MPa) while the first ones showed to have the worst yield strength (~700 MPa). In addition, the authors concluded that the heat-treated specimens showed worst elongation results under the high temperature yield test as opposed to the as-built specimen which had a total elongation of nearly 35 %.

In a distinct experience, Zhang et al. [62] studied the influence of standard heat treatments, based on the AMS 5662, on the mechanical properties and microstructure of additively manufactured IN718 specimens. In this way, the researchers started by studying the microstructure of the as-built specimens, Figure 11, and then submitted ones to a SA + DA, as well as to HO + SA + DA treatments as the standard recommends. After conducting different tests, the authors reported that the microstructure of the SA + DA specimens had the precipitation of the γ' and γ'' phases in the γ matrix while the δ phase precipitated in the grain boundaries and grain interior. Therefore, the mechanical strength of the aforementioned specimens was much better than the as-built ones, however, the ductility decreased. In addition, the HO + SA + DA heat-treated specimens had a decrease of 4 % in yield strength when compared to the SA + DA, but the ductility increased 22 % because the δ phase precipitates were reduced. In a similar study, Karabulut et al. [63] studied the heat treatment influence on the microstructure, microhardness, and wear resistance of selective laser manufactured IN718 specimens. The researchers followed a standard heat treatment for casted IN718 used on [62]. After the investigation of the microstructure, the authors concluded that the heat treatment must be done at temperatures above 900 °C in order to promote the creation of grains and grain boundaries, as well as to eliminate cellular dendritic structures and laser scanning paths. In addition, the low temperature heat treatments improved the wear resistance and increased the microhardness, while the ones done at high temperature promoted the opposite.

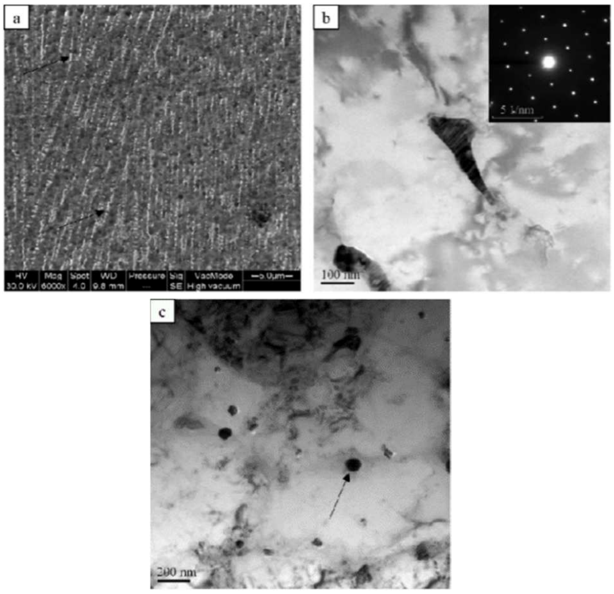

Figure 11 - Microstructure of the as-built sample, a) SEM micrograph showing columnar dendrites, b) TEM image Laves phase and the corresponding SAED pattern, and c) TEM image of carbide [62]

In another scientific paper, Pei et al. [64] compared AMS 5663 heat-treated SLM printed IN718 specimens with forged IN718 in terms of fatigue performance and mechanical properties. Before doing the aforementioned heat treatment, the specimens underwent a HO process, which was meant to reduce the residual stresses, at 1100 °C for 1.5 hours followed by AC. After the mechanical tests, the researchers concluded that the ultimate tensile strength of the SLMed specimens was higher in the horizontal direction than the forged IN718, however, the latter had superior fatigue performance than the former one, which was related to the micro-defects and low ductility of the printed specimens. Li et al. [65] employed a novel heat treatment which aimed to improve the plasticity while keeping the mechanical strength of selective laser melted IN718 specimens, having in mind that the traditional HO + DA treatment would increase strength but lower the ductility. The researchers managed to accomplish that by conducting a heat treatment composed by HO at 1150 °C for 2 hours followed by air-cooling, and then one-time aging at 700 °C for 12 hours followed by water-cooling. The tensile test confirmed that the elongation at break improved from 17 % to 24 % while the ultimate tensile strength decreased 5 MPa.

Xu et al. [66] studied the effect of heat treatments on the creep performance of Selective Laser Melted specimens of IN718 and compared the results with conventional hot-rolled coupons and as-built specimens. The researchers conducted a standard heat treatment according to AMS 5383 and in another specimen performed a HIP treatment at 1200 °C and with a pressure of 103 MPa for 4 hours. Then, conducted a creep test at 650 °C and 650 MPa of the four types of specimens and, after accessing the results, they concluded that the HIPed samples yielded a mean of 20 hours compared to 90 hours for the heat-treated ones, Figure 12. This low value was caused by an excessive intergranular precipitation made by the HIP process. Furthermore, the hot-rolled specimens yielded for the longest time (200 hours) due to the fact of having a finer average grain size.

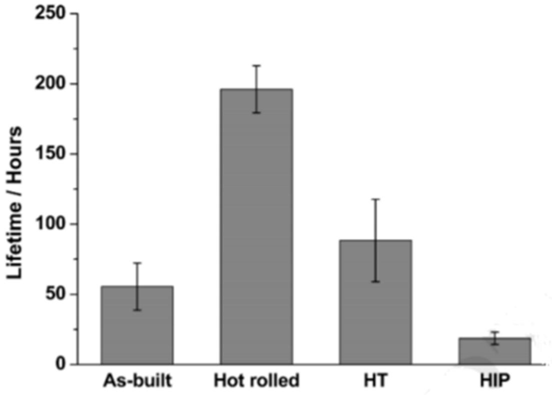

Figure 12 - Average lifetime of the as-built, hot rolled, heat treated, and HIPed specimens [66]

In another study, Schaak et al. [67] analysed the percentage of infiltrated Argon after a HIP treatment. For that, they printed rectangular specimens of IN718 and subjected them to a measurement of the percentage of infiltrated Argon before and after HIP. In addition, they also measured the porosity of the samples before and after heat treatment, using micro X-ray Computed Tomography. They concluded that the HIP treatment reduced the porosity of the specimens, but caused an exponential increase in Argon infiltration, going from 0.308 ppm to 3.22 ppm. However, they realized that this increase was due to the large inclusion of the gas near the surface of the samples and after grinding the surface, the value decreased to 0.36 ppm. In a distinct report, Tillmann et al. [68] applied a HIP treatment to SLMed IN718 samples in order to ascertain if the porosity would decrease. The researchers conducted several HIP tests where the time had a fixed value of 2 hours, the temperature ranged from 500 °C to 1300 °C, and the pressure varied from 50 MPa up to 150 MPa. After measuring the porosity of the HIPed specimens through a micro X-Ray Computed Tomography device, the authors concluded that the process pressure had less influence than the temperature and, in order to obtain a significant porosity reduction, the process temperature must be over 1150 °C and the pressure higher than 100 MPa, Figure 13. In addition, the researchers found out that even with the best HIP parameters and an enhanced holding time of 4 hours, the specimens could not be 100 % dense (99,998 %).

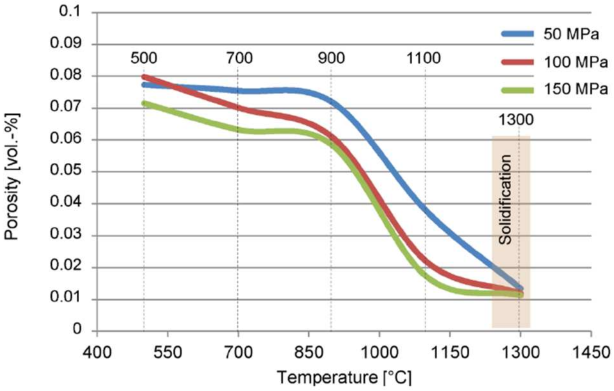

Figure 13 - Influence of HIP parameters on part porosity [68]

Jiang et al. [69] investigated the influence of post-build heat treatments on the phase formation, mechanical properties, microstructure, and recrystallization behavior of SLMed IN718 parts. The specimens were heat treated as follows: no post-treatment, three different simulated HIP at 1120 °C (for 1.5 hours, 4 hours, and 16 hours) followed by water quenching (WQ), direct DA treatment at 720 °C for 8 hours followed by FC at 55 °C/h rate until it have reached 620 °C and then held at that temperature for 8 hours followed by AC, and finally simulated HIP at 1120 °C for 4 hours followed by WQ + DA treatment as described before. After a careful analysis, the researchers concluded that the time increase in the simulated HIP resulted in a xz-plane microstructure evolution from columnar to equiaxed grains, and also the 16 hour HIPed specimen exhibited a lower orientation gradient and a nearly strain-free condition that led to isotropic mechanical properties. In addition, the DA treatment promoted the increase of the Young's modulus and hardness, Table 5. Amato et al. [70] studied the influence that different heat treatments had on the hardness of SLMed IN718 parts. In order to do that, they submitted the samples to two distinct post-processes. The first was a treatment of HIP at 1163 °C with a pressure of 100 MPa for 4 hours + SA at 1160 °C for 4 hours, and the second only applying SA with the conditions of the previous one. After the hardness tests, they compared the as-built, HIP + SA, SA, and SA wrought IN718 samples and concluded that the specimen with the solution annealing treatment was the one that obtained the highest hardness values (39 HRC), followed by HIP + SA (33 HRC), then the as-built (30 HRC), and finally SA wrought IN718 (24 HRC).

Table 5 - Hardness and Young's Modulus of the different samples [69]

Sample	**Vickers Microhardness [HV2.0]**	**Young's Modulus [GPa]**
As-built (xy)	281.0 ± 18.4	208.8 ± 5.8
As-built (xz)	254.0 ± 11.1	202.6 ± 11.2
HIP 1.5h (xy)	205.0 ± 9.9	225.3 ± 25.0
HIP 1.5h (xz)	211.8 ± 5.7	208.4 ± 15.6
HIP 4h (xy)	181.3 ± 5.8	225.4 ± 7.4
HIP 4h (xz)	185.9 ± 12.1	203.2 ± 7.8
HIP 16h (xy)	170.5 ± 5.9	229.4 ± 8.6
HIP 16h (xz)	171.1 ± 6.2	225.6 ± 8.9
HIP + DA (xy)	390.7 ± 12.2	232.5 ± 12.6
HIP + DA (xz)	404.5 ± 9.1	223.5 ± 6.1
DA (xy)	476.2 ± 32.9	232.3 ± 10.8
DA (xz)	393.1 ± 14.4	226.7 ± 12.8

Raza et al. [71] studied the influence that different heat treatments have on the microstructure of selective laser melted IN718 coupons. For that, the researchers employed three distinct heat treatments, namely Pseudo HIP (done without pressure) at 1160 °C for 3 hours, HIP + SA at 954 °C for one hour, and Pseudo HIP + SA + DA at 760 °C for 5 hours and then 649 °C for 1 hour. After that, the authors studied the microstructure of the different heat-treated specimens and reported that the Pseudo HIP altered the grain morphology to a coarser equiaxed one, and dissolved the Laves phase. Due to the SA, intergranular plate-like precipitates, which the authors presumed to be the δ phase, and MC-type carbides were visible through SEM. In addition, the DA specimens showed precipitates of δ phase within the grain boundary and coarser MC-type carbides residing in the grains. Similarly, Popovich et al. [72] investigated the heat treatment effects on microstructure and mechanical properties of IN718 additive manufactured specimens. For that, the researchers studied the samples under four different conditions, namely as-built, SA at 850 °C for two hours then air-cooled, HIP at 1180 °C and 150 MPa of pressure for 3 hours followed by furnace cooling, and finally HIP + HO at 1065 °C for 1 hour followed by air-cooling + DA at 760 °C for 10 hours followed by FC at a 55 °C/h rate until it reaches 650 °C, then held at that temperature for 8 hours followed by AC. After running some tests, the authors found out that the as-built specimens' microstructure had distinctive fine- and coarse-grained zones and exhibited carbide particles and interdendritic Laves phases. In addition, the HIPed specimens showed better mechanical properties because of the dissolution of the undesirable δ and Laves phases, however, they kept a sharp microstructural border between coarse- and fine-grained regions.

Aydinöz et al. [73] studied the influence that distinct heat treatments have on the microstructure of IN718 specimens printed by SLM. To do this, they submitted the samples to six different post-treatment conditions and left one in the as-built state for later analysis. The first post-treatment condition was SA at 1000 °C for one hour, followed by AC. The second condition was HIP at 1150 °C with a pressure of 1000 bar for 4 hours followed by FC. The third condition to which the samples were subjected was a SA treatment, as described above, followed by a DA at 720 °C for 8 hours with subsequent FC at 50 °C/h rate until it reached 621 °C, then was held at that temperature for 8 hours and finally air-cooled. The fourth was HIP + DA, as previously described. The fifth was Arc-PVD coating + HIP and the last one was Arc-PVD coating + HIP + DA as it was previously described in other conditions. Then, the researchers carried out tests to inspect the size, orientation, and boundary of the grain by means of a SEM equipped with an electron backscatter diffraction (EBSD) and, posteriorly used a TEM equipped with energy dispersive spectroscopy (EDS) system to identify the formation of precipitates. They concluded that the as-built specimen had a columnar grained structure, and the SA treatment dissolved the Laves phase and created cell structures with sharp boundaries. In addition, the DA treatment led to the evolution of γ'' precipitates, and the HIP originated a recrystallization of the specimen, Figure 14c, and eliminated cell structures. Furthermore, the DA treatment performed after HIP led to the evolution of the δ phase, mainly at the grain boundaries, and the formation of γ'' precipitates. Alternatively, Wang at al. [74] studied the influence that heat treatments have on relieving residual stresses of SLMed IN718 components. In fact, the authors employed a stress relief heat treatment and reported that the compressive residual stresses were lowered from 378.4 MPa to 321 MPa due to a microstructural homogenization as the Laves partially dissolved into the γ matrix.

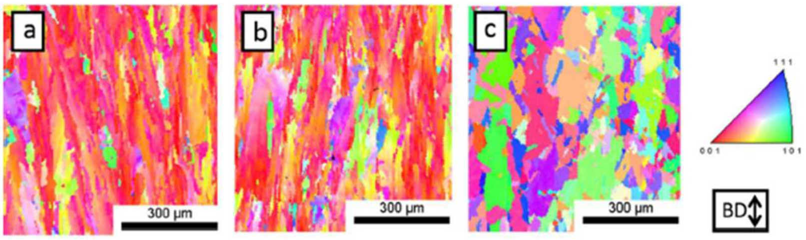

Figure 14 - EBSD micrographs, a) as-built condition, b) SA condition, and c) HIP condition [73]

Finally, the authors of the current report compiled in Table 6 distinct values of YS, UTS, and ε in order to enable the reader to draw conclusions and comparisons between different heat treatments.

Table 6 - Manufacturing process and post-treatment effect on the mechanical properties of the IN718 alloy

Mnf. Process	Condit.	Orient.	YS [MPa]	UTS [MPa]	ε [%]	Ref.
SLM	SA + A	V	1184	1351	23	[51]
SLM	SA + A	H	1231	1430	20	[51]
SLM	SA	-	541	976	39.1	[52]
SLM	SA + DA	-	1306	1475	22.2	[52]
SLM	DA	-	1374	1545	14.1	[52]
SLM	As-built	-	643	991	13	[53]
SLM	SA + DA	-	1159	1377	8	[53]
SLM	SA + DA	H	1173	1450	13.5	[54]
SLM	As-built	H	889 – 907	1137 – 1148	19.2 – 25.9	[55]
SLM	SA + DA	H	1102 – 1161	1280 – 1358	10 – 22	[55]
SLM	DA	-	~1370	~1500	~7.5	[61]
SLM	SA + DA	-	~1250	~1400	~15	[61]
SLM	HO + SA + DA	-	~1250	~1350	~13	[61]
SLM	SA + DA	H	1084	1371	10.1	[62]
SLM	HO + SA + DA	H	1046	1371	12.3	[62]
SLM	SA + DA	H	1329	1429	-	[64]
SLM	HO + DA	-	1100	1325	17	[65]
SLM	HO + A	-	1070	1320	24	[65]
SLM	HIP + SA	V	850	1140	28	[70]
SLM	HIP + SA	H	890	1200	28	[70]
SLM	HIP	-	645	1025	38	[72]

Mnf. Process	Condit.	Orient.	YS [MPa]	UTS [MPa]	ε [%]	Ref.
SLM	HIP + HO + DA	-	1145	1376	19	[72]
SLM	As-built	V	580	845	-	[73]
SLM	SA	V	535	870	-	[73]
SLM	SA + DA	V	1240	1400	-	[73]
SLM	HIP	V	430	875	-	[73]
SLM	HIP + DA	V	1100	1315	-	[73]
SLM	Arc-PVD + HIP	V	420	815	-	[73]
SLM	Arc-PVD + HIP + DA	V	1185	1300	-	[73]
Cast	-	-	758	862	5	[62]
Wrought	-	-	1030 – 1167	1275 – 1400	12 – 21	[75]

3.2 Residual Stresses

As it was written before, residual stresses are pretty common in the selective laser melting process as it involves severe temperature gradients which cause heterogeneous plastic strains [76]. Moreover, in AM residual stresses are spatially nonuniform and can lead to worse fatigue life and mechanical properties of the built components, as well as layer delamination and part distortion [77]. Furthermore, the length of the scan vectors made by the laser can also influence the magnitude and distribution of RS, as shorter scan vectors, which are preferable to create lower RS, result in a lower temperature gradient, opposite to longer scan vectors which result in a higher temperature gradient [78]. Hence, one of the most usual scanning strategies employed is the chessboard scanning [79,80], thus Lu et al. [81] investigated the RS evolution on distinct chessboard scanning areas of selective laser melted IN718 specimens through Vickers micro-indentation. After performing the aforementioned test, the authors reported that the lowest RS were found in the 2 x 2 mm^2 sample, however, that only happened because cracks were formed, and stresses were released. Thus, the authors concluded that the 5 x 5 mm^2 scanning area was the best to produce end parts with the lowest RS. In another scientific paper, Yi et al. [82] investigated the Linear Energy Density (LED) effect on the deformation of sectioned IN718 specimens manufactured via SLM. The authors reported that higher LED values would increase the specimens' deformation and, therefore, higher residual stresses could be seen.

Mukherjee et al. [83] proved, by using thermal simulations and an analytical strain parameter, that the residual stresses on IN718 parts would decrease when the scanning speed is increased. On the contrary, the increase of the laser power and the number of layers was proven to enlarge the RS, Figure 15. In another study, Ahmad et al. [84] quantified the residual stresses on SLMed IN718 specimens through an experimental measuring technique called contour method. The researchers concluded that, near the surface, the tensile stresses were 837 MPa, and at the middle of the part, the compressive stresses were 459 MPa.

As a matter of fact, on SLMed parts, horizontal oriented RS are of lower magnitude than vertical ones since the hot melted material on top of the cold previous layer creates bending forces [76]. Also, several studies [85-93] reported that upon cooling, one should expect compressive stresses in the middle of the part and tensile stresses near the surface. However, some researchers came across to contrary results, namely Ghosh et al. [94] found irregularities between simulation and experimental results, Cottam et al. [95] reported that the H13 tool steel had an opposite RS distribution to the one found in the literature, and Barros et al. [96] used a semi-destructive technique called hole-drilling strain-gage method to investigate the heat treatment effect on RS of SLMed IN718 components and concluded that the RS were lowered, although compressive stresses near the surface were measured in the heat-treated specimens, which evolved to tensile stresses as the depth increased.

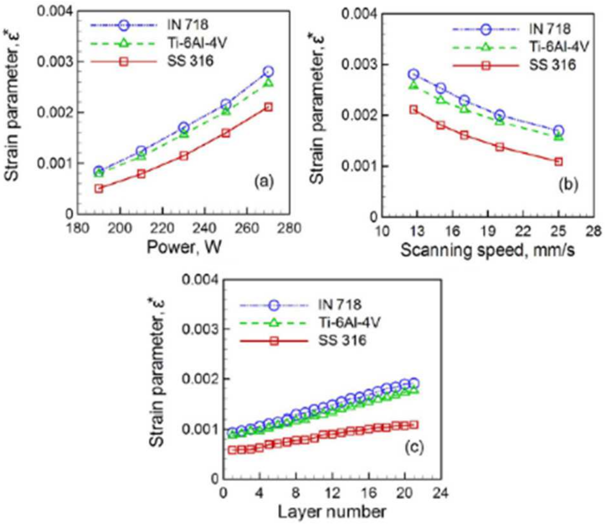

Figure 15 - Non-dimensional strain variation depending on a) laser power with a constant scan speed, b) scan speed with a constant laser power, and c) number of layers for a constant scan speed and laser power [83]

The main focus of this review paper has been about SLMed components, however, the authors thought that it would be also interesting to compare the residual stresses on SLM and EBM processes since both can be classified as a powder bed fusion technology. Thus, the main differences between the two processes are the beam source and the temperature of the build chamber, as the EBM technology keeps the latter at a much higher temperature (500-800 °C) [97-100]. Hence, one should expect fewer residual stresses because of the lower temperature gradient during manufacturing ($T_{melt} - T_{ambient}$). Keeping in mind that, Sochalski-Kolbus et al. [101] investigated the RS difference between SLMed and EBMed IN718 components using neutron diffraction. The authors concluded that the preheating step and cooling rate of the EBM process produced parts with almost 400 MPa lesser residual stresses than the SLM process.

Nadammal et al. [102] studied the hatch length effect on RS of additively manufactured IN718 specimens. To do that, the researchers used neutron diffraction to access the residual stresses of the different specimens and concluded that for short hatch lengths the normal stress component is thoroughly compressive. Also, the longitudinal stress component for the shorter hatch length specimens moved from 200 MPa tensile stress to 300 MPa compressive stress.

Residual stresses can also be predicted through computational models, namely FEM which is a strong tool that has been used for additive and several other manufacturing processes. However, computing residual stresses through FEM in AM is not so simple and, in some cases, requires several days to run a study, because of the large number of thin layers, temperature gradients, and the different laser paths that are inherent to the process [103]. In addition, Wang et al. [104] stated that the computational models should be subsequently validated through non-destructive and/or destructive techniques. Keeping in mind that, several researchers [10,105,106] developed an approximation model in which the computational time was decreased by gathering several thin layers (thickness in the order of microns) into one large layer (thickness in the order of millimetres). Williams et al. [105] applied the aforementioned model to a bridge-like and a cubic component and reported that the simulated distortion was within 5 % and 10 %, respectively. In another study, Song et al. [107] used FEM to predict the temperature distribution within a single layer in order to obtain better processing parameters. The researchers found out that for a scan speed of 0.2 m/s and a laser power of 110 W the maximum achievable melt depth of a single layer was roughly 45 µm. Song et al. [108] used the ABAQUS AM model to simulate the distortion of SLMed IN718 components under different support structure thickness (0.4 and 0.7 mm). In order to save computational time, the authors neglected the influence of the laser path, hence the in-plane anisotropy of the resulting stress field was ignored. Hence, the researchers reported that a thicker support structure reduced the part distortion and, therefore, the residual stresses. However, one should be aware that a thicker support structure also leads to more material spent and further post-processing time. Finally, Siewert et al. [109] used the Mechanical Layer Equivalent (MLE) method, which is based on the inherent strain method and significantly reduces the computational time because it handles the case as a structural-mechanical problem instead of a thermo-mechanical one, to predict residual stresses of SLMed components. After comparing the results with an XRD analysis, the authors found out that the MLE method had good accordance with the latter, especially when computing critical stresses.

Finally, in order to ease the reader, the authors created Table 7 which can be used as a searching guide to look up scientific articles related to heat treatments within this review paper.

Table 7 - Guide table

Topic	Reference(s)
SA	[47,48]
SA + DA	[49-56]
DA, SA + DA	[57]
DA, SA, SA + DA	[58]
DA, SA + DA, HO + DA	[59]
DA, SA + DA, HO + DA, HO + SA + DA	[60]
DA, SA + DA, HO + SA + DA	[61]
SA + DA, HO + SA + DA	[62,63]
HO + SA + DA	[64]
HO + A	[65]
HO + SA + DA, HIP	[66]
HIP	[67,68]
HIP, DA, HIP + DA	[69]
HIP + SA, SA	[70]
HIP + SA, Pseudo HIP, Pseudo HIP + SA + DA	[71]
HIP, HIP + HO, SA	[72]
HIP, HIP + DA, SA, SA + DA, PVD + HIP, PVD + HIP + DA	[73]

4 Concluding Remarks and Outlook

One of the most used superalloys in AM is the IN718 which is a precipitation-hardened alloy that can be applied in several distinct areas, namely in the marine, nuclear power plants, gas turbines, and aerospace fields due to its solid mechanical stability at temperatures up to nearly 700 °C. For this review work, the authors analysed more than 100 different publications to provide a solid and unbiased overview of heat treatments and residual stresses of IN718 components produced via SLM. The main ideas can be described as follows:

- Owing to the inherent characteristics of the SLM process, i.e. high cooling rates and quick solidification, the expected microstructure in the as-built state is characterized by fine columnar grains and a saturated γ matrix with the presence of the Laves phase and carbides, due to the high segregation susceptibility of Mo, Nb, and Ti. This heterogeneous microstructure eventually promotes weak and anisotropic mechanical properties, meaning that, for high and cyclic loads applications, heat treatments should be employed.
- If one seeks to improve the mechanical properties, such as yield and ultimate tensile strength, as well as the hardness of IN718 parts, then a SA heat treatment followed by DA should be conducted. The former is responsible for dissolving the undesired phases, such as carbides and Laves, while the latter promotes the formation of the strengthening phases γ’ and γ’’.
- The temperature of the SA treatment dictates the expected microstructure, i.e. 1065 °C promotes the full dissolution of the Laves phase, however, if done at 980 °C the Laves phase will not be completely dissolved and results in the formation of the δ phase, since the solution temperature is inferior to the solvus temperature of both phases.
- Usually, when the printing parameters are optimized, one can obtain a component with a density over 99 %, however, sometimes it may be necessary to conduct a HIP treatment to increase the density of the printed components. In that case, the expected final density of the part is nearly

100 % and normally, leads to microstructure recrystallization. Furthermore, it was also shown that for reducing the part porosity the HIP temperature is more critical than the pressure, and for obtaining optimized results one should use a temperature over 1150 °C and a pressure greater than 100 MPa.

- It has been seen that residual stresses can be lowered through heat treatments as well as optimized printing parameters, such as a lower beam power and number of layers. In addition, a high scanning speed coupled with shorter scan vectors, i.e. chessboard scanning, has been demonstrated to lower the residual stresses on IN718 parts. Despite that, it was also shown that some researchers found contrary results from the literature as the RS distribution changed after conducting heat treatments.
- Regarding the RS computation through FEM, it can be concluded that a meticulous study is not viable as it would take days to run in an ordinary computer, however, approximations, i.e. gathering thin layers together, can be successfully done with a 10% degree of error.

Despite the tremendous research over the last years about additively manufactured IN718 parts, there are still some problems to overcome. Namely, the mechanical properties variability when subjected to different process parameters. Also, heat treatments should be further investigated and improved because often one sacrifices ductility for yield and ultimate tensile strength or vice-versa. Finally, there is still a lot of work to do regarding residual stresses of SLMed IN718 components, i.e. research the RS evolution under different heat treatments and develop new computer models that can predict RS under different processing parameters in a quick and trustworthy way.

Acknowledgements The main author would like to thank his mentor for all the support throughout the writing of this report.

List of Symbols and Abbreviations

3DP	Three-dimensional Printing
A	Aging
AC	Air Cooling
AM	Additive Manufacturing
ASTM	American Society for Testing and Materials
Condit.	Condition
DA	Double Aging
EBM	Electron Beam Melting
EBSD	Electron Backscatter Diffraction
EDS	Energy Dispersive Spectroscopy
FC	Furnace Cooling
FCC	Face-centred Cubic
FEM	Finite Element Modelling
H	Horizontal
HIP	Hot Isostatic Pressing
HO	Homogenization
HT	Heat Treatment
IN718	Inconel 718
LED	Linear Energy Density
MLE	Mechanical Layer Equivalent
Orient.	Orientation
Ref.	Reference
RS	Residual Stresses

SA	Solution Annealing
SEM	Scanning Electron Microscope
SLM	Selective Laser Melting
SLS	Selective Laser Sintering
t	Minimum Solution Time
T	Minimum Solution Temperature
$T_{ambient}$	Ambient Temperature
TEM	Transmission Electron Microscope
T_{melt}	Melting Temperature
UTS	Ultimate Tensile Strength
V	Vertical
WQ	Water Quenching
XRD	X-ray Diffraction
YS	Yield Strength
ε	Elongation at Break

References

1. Goldberg, D. (2018). *History of 3D Printing: It's Older Than You Are (That Is, If You're Under 30)*, AutoDesk. [Online], available on: https://www.autodesk.com/ redshift/history-of-3d-printing/ [Viewed on 12/2019].
2. ASTM F2792-12a, "Standard Terminology for Additive Manufacturing Technologies", (Withdrawn 2015) ASTM International, pp. 1–3, West Conshohocken, PA, 2012.
3. Silva, F. J. G., Campilho, R. D. S. G., Gouveia, R. M., Pinto, G., & Baptista, A. (2018). A Novel Approach to Optimize the Design of Parts for Additive Manufacturing. In *Procedia Manufacturing*, *17*, pp. 53–61.
4. Gouveia, R. M., Silva, F. J. G., Atzeni, E., Sormaz, D., Alves, J. L., & Pereira, A. B. (2020). Effect of Scan Strategies and Use of Support Structures on Surface Quality and Hardness of L-PBF AlSi10Mg Parts, *Materials, 13*(10), 2248 (20 pp.).
5. W. Meiners. *Shaped body especially prototype or replacement part production*, German patent 19649865 filled on December 2nd of 1996, issued on February 12th of 1998.
6. Giganto, S., Zapico, P., Castro-Sastre, M. Á., Martínez-Pellitero, S., Leo, P., & Perulli, P. (2019). Influence of the scanning strategy parameters upon the quality of the SLM parts. *Procedia Manufacturing*, *41*, pp. 698–705.
7. Anwar, A. B., Ibrahim, I. H., & Pham, Q. C. (2019). Spatter transport by inert gas flow in selective laser melting: A simulation study. *Powder Technology*, *352*, pp. 103–116.
8. Ferrar, B., Mullen, L., Jones, E., Stamp, R., & Sutcliffe, C. J. (2012). Gas flow effects on selective laser melting (SLM) manufacturing performance. *Journal of Materials Processing Technology*, *212*(2), pp. 355–364.
9. Konečná, R., Nicoletto, G., & Riva, E. (2019). Notch fatigue behavior of Inconel 718 produced by selective laser melting. *Procedia Structural Integrity*, *17*, pp. 138–145.
10. Contuzzi, N., Campanelli, S. L., & Ludovico, A. D. (2011). 3D finite element analysis in the Selective Laser Melting process. *International Journal of Simulation Modelling*, *10*(3), pp. 113–121.
11. Nguyen, Q. B., Luu, D. N., Nai, S. M. L., Zhu, Z., Chen, Z., & Wei, J. (2018). The role of powder layer thickness on the quality of SLM printed parts. *Archives of Civil and Mechanical Engineering*, *18*(3), pp. 948–955.
12. Leitz, K. H., Singer, P., Plankensteiner, A., Tabernig, B., Kestler, H., & Sigl, L. S. (2017). Multi-physical simulation of selective laser melting. *Metal Powder Report*, *72*(5), pp. 331–338.
13. Luo, S., Huang, W., Yang, H., Yang, J., Wang, Z., & Zeng, X. (2019). Microstructural evolution and corrosion behaviors of Inconel 718 alloy produced by selective laser melting following different heat treatments. *Additive Manufacturing*, *30*, 100875 (13 pp.).
14. Qi, H., Azer, M., & Ritter, A. (2009). Studies of standard heat treatment effects on microstructure and mechanical properties of laser net shape manufactured INCONEL 718. *Metallurgical and Materials Transactions A: Physical Metallurgy and Materials Science*, *40*(10), pp. 2410–2422.
15. Hosseini, E., & Popovich, V. A. (2019). A review of mechanical properties of additively manufactured Inconel 718. *Additive Manufacturing*, *30*, 100877 (18 pp.).
16. Sui, S., Tan, H., Chen, J., Zhong, C., Li, Z., Fan, W., Gasser, A., & Huang, W. (2019). The influence of Laves phases on the room temperature tensile properties of Inconel 718 fabricated by powder feeding laser additive manufacturing. *Acta Materialia*, *164*, pp. 413–427.
17. He, D. G., Lin, Y. C., Jiang, X. Y., Yin, L. X., Wang, L. H., & Wu, Q. (2018). Dissolution mechanisms and kinetics of δ phase in an aged Ni-based superalloy in hot deformation process. *Materials and Design*, *156*, pp. 262–271.
18. Gu, D. D., Meiners, W., Wissenbach, K., & Poprawe, R. (2012). Laser additive manufacturing of metallic components: Materials, processes and mechanisms. *International Materials Reviews*, *57*(3), pp. 133–164.

19. Baicheng, Z., Xiaohua, L., Jiaming, B., Junfeng, G., Pan, W., Chen-nan, S., Muiling, N., Guojun, Q., & Jun, W. (2017). Study of selective laser melting (SLM) Inconel 718 part surface improvement by electrochemical polishing. *Materials and Design, 116*, pp. 531–537.
20. Yang, H., Jing, G., Gao, P., Wang, Z., & Li, X. (2020). Effects of circular beam oscillation technique on formability and solidification behaviour of selective laser melted Inconel 718: From single tracks to cuboid samples. *Journal of Materials Science and Technology*, *51*, pp. 137–150.
21. Pröbstle, M., Neumeier, S., Hopfenmüller, J., Freund, L. P., Niendorf, T., Schwarze, D., & Göken, M. (2016). Superior creep strength of a nickel-based superalloy produced by selective laser melting. *Materials Science and Engineering A*, *674*, pp. 299–307.
22. Yuan, K., Guo, W., Li, P., Wang, J., Su, Y., Lin, X., & Li, Y. (2018). Influence of process parameters and heat treatments on the microstructures and dynamic mechanical behaviors of Inconel 718 superalloy manufactured by laser metal deposition. *Materials Science and Engineering A*, *721*, pp. 215–225.
23. Zhang, D., Feng, Z., Wang, C., Wang, W., Liu, Z., & Niu, W. (2018). Comparison of microstructures and mechanical properties of Inconel 718 alloy processed by selective laser melting and casting. *Materials Science and Engineering A, 724*, pp. 357–367.
24. You, X., Tan, Y., Shi, S., Yang, J. M., Wang, Y., Li, J., & You, Q. (2017). Effect of solution heat treatment on the precipitation behavior and strengthening mechanisms of electron beam smelted Inconel 718 superalloy. *Materials Science and Engineering A*, *689*, pp. 257–268.
25. Schneider, J., Lund, B., & Fullen, M. (2018). Effect of heat treatment variations on the mechanical properties of Inconel 718 selective laser melted specimens. *Additive Manufacturing*, *21*, pp. 248–254.
26. Goel, S., Ahlfors, M., Bahbou, F., & Joshi, S. (2019). Effect of Different Post-treatments on the Microstructure of EBM-Built Alloy 718. *Journal of Materials Engineering and Performance*, *28*(2), pp. 673–680.
27. Sui, S., Zhong, C., Chen, J., Gasser, A., Huang, W., & Schleifenbaum, J. H. (2018). Influence of solution heat treatment on microstructure and tensile properties of Inconel 718 formed by high-deposition-rate laser metal deposition. *Journal of Alloys and Compounds*, *740*, pp. 389–399.
28. Wang, K., Liu, Y., Sun, Z., Lin, J., Lv, Y., & Xu, B. (2020). Microstructural evolution and mechanical properties of Inconel 718 superalloy thin wall fabricated by pulsed plasma arc additive manufacturing. *Journal of Alloys and Compounds*, *819*, 152936 (24 pp.).
29. ASTM F3055, "Standard specification for additive manufacturing nickel alloy (UNS N07718) with powder bed fusion". ASTM International, West Conshohocken, PA, 2014.
30. AMS 5663, Nickel Alloy, Corrosion and Heat-Resistant, Investment Castings, 52.5Ni-19Cr-3.0Mo-5.1Cb(Nb)-0.90Ti-0.60Al-18Fe, Vacuum Melted Homogenization and Solution Heat Treated, SAE International, 1965.
31. AMS 5383, Nickel Alloy, Corrosion and Heat-Resistant, Investment Castings, 52.5Ni-19Cr-3.0Mo-5.1Cb(Nb)-0.90Ti-0.60Al-18Fe, Vacuum Melted Homogenization and Solution Heat Treated, SAE International, 1966.
32. AMS 5664E, Nickel Alloy, Corrosion and Heat Resistant, Bars, Forgings, and Rings 52.5Ni-19Cr-3.0Mo-5.1Cb-0.90Ti-0.50Al-18Fe Consumable Electrode or Vacuum Induction Melted 1950 °F (1066 °C) Solution Heat Treated, Precipitation Hardenable, SAE International, 2006.
33. Bartlett, J. L., & Li, X. (2019). An overview of residual stresses in metal powder bed fusion. *Additive Manufacturing, 27*, pp. 131-149.
34. Liu, D., & Flewitt, P. E. J. (2014). Raman measurements of stress in films and coatings. *Spectroscopic Properties of Inorganic and Organometallic Compounds*, *45*, pp. 141–177.
35. Guo, J., Fu, H., Pan, B., & Kang, R. (2020). Recent progress of residual stress measurement methods: A review. *Chinese Journal of Aeronautics*, In press, https://doi.org/10.1016/j.cja.2019.10.010.
36. ASTM E 837-08. (2008). Standard Test Method for Determining Residual Stresses by the Hole-Drilling Strain-Gages, *1*, pp. 1–17.
37. Aboulkhair, N, Maskery, I, Ashcroft I, Tuck, C, Everitt, N. (2015). The role of powder properties on the processability of Aluminium alloys in selective laser melting. *Lasers in Manufacturing Conference 2015*.
38. Cunningham, R., Nicolas, A., Madsen, J., Fodran, E., Anagnostou, E., Sangid, M. D., & Rollett, A. D. (2017). Analyzing the effects of powder and post-processing on porosity and properties of electron beam melted Ti-6Al-4V. *Materials Research Letters*, *5*(7), pp. 516–525.
39. Panwisawas, C., Qiu, C. L., Sovani, Y., Brooks, J. W., Attallah, M. M., & Basoalto, H. C. (2015). On the role of thermal fluid dynamics into the evolution of porosity during selective laser melting. *Scripta Materialia*, *105*, pp. 14–17.
40. Escano, L.I., Parab, N.D., Xiong, L., Guo, Q., Zhao, C., Fezzaa, K., Everhart, W., Sun, T., & Chen, L. (2018). Revealing particle-scale powder spreading dynamics in powder-bed-based additive manufacturing process by high-speed x-ray imaging. *Scientific Reports 8*(1) **,** 15079.
41. Tan, J. H., Wong, W. L. E., & Dalgarno, K. W. (2017). An overview of powder granulometry on feedstock and part performance in the selective laser melting process. *Additive Manufacturing, 21,* pp. 228-255.
42. Santecchia, E., Spigarelli, S., & Cabibbo, M. (2020). Material reuse in laser powder bed fusion: Side effects of the laser—metal powder interaction. *Metals, 10*(3), 341.
43. Denti, L., Sola, A., Defanti, S., Sciancalepore, C., & Bondioli, F. (2019). Effect of powder recycling in laser-based powder bed fusion of Ti-6Al-4V. *Manufacturing Technology*, *19*(2), pp. 190–196.
44. Cordova, L., Campos, M., & Tinga, T. (2019). Revealing the Effects of Powder Reuse for Selective Laser Melting by Powder Characterization. *JOM*, *71*(3), pp. 1062–1072.
45. Zhao, Y., Aoyagi, K., Daino, Y., Yamanaka, K., & Chiba, A. (2020). Significance of powder feedstock characteristics in defect suppression of additively manufactured Inconel 718. *Additive Manufacturing*, *34,* 101277.
46. Calandri, M., Yin, S., Aldwell, B., Calignano, F., Lupoi, R., & Ugues, D. (2019). Texture and microstructural features at different length scales in Inconel 718 produced by selective laser melting. *Materials*, *12*(8), 1293 (32 pp.).

47. Tucho, W. M., Cuvillier, P., Sjolyst-Kverneland, A., & Hansen, V. (2017). Microstructure and hardness studies of Inconel 718 manufactured by selective laser melting before and after solution heat treatment. *Materials Science and Engineering A*, *689*, pp. 220–232.
48. Calandri, M., Manfredi, D., Calignano, F., Ambrosio, E. P., Biamino, S., Lupoi, R., & Ugues, D. (2018). Solution Treatment Study of Inconel 718 Produced by SLM Additive Technique in View of the Oxidation Resistance. *Advanced Engineering Materials*, *20*(11), 1800351 (16 pp.).
49. Cao, G. H., Sun, T. Y., Wang, C. H., Li, X., Liu, M., Zhang, Z. X., Hu, P. F., Russel, A. M., Schneider, R., Gerthsen, D., Zhou, Z. J., Li, C. P., & Chen, G. F. (2018). Investigations of γ′ γ″ and δ precipitates in heat-treated Inconel 718 alloy fabricated by selective laser melting. *Materials Characterization*, *136*, pp. 398–406.
50. Feng, K., Liu, P., Li, H., Sun, S., Xu, S., & Li, J. (2017). Microstructure and phase transformation on the surface of Inconel 718 alloys fabricated by SLM under 1050°C solid solution + double ageing. *Vacuum*, *145*, pp. 112–115.
51. Komarasamy, M., Shukla, S., Williams, S., Kandasamy, K., Kelly, S., & Mishra, R. S. (2019). Microstructure, fatigue, and impact toughness properties of additively manufactured nickel alloy 718. *Additive Manufacturing*, *28*, pp. 661–675.
52. Huang, W., Yang, J., Yang, H., Jing, G., Wang, Z., & Zeng, X. (2019). Heat treatment of Inconel 718 produced by selective laser melting: Microstructure and mechanical properties. *Materials Science and Engineering A*, *750*, pp. 98–107.
53. Chlebus, E., Gruber, K., Kuźnicka, B., Kurzac, J., & Kurzynowski, T. (2015). Effect of heat treatment on the microstructure and mechanical properties of Inconel 718 processed by selective laser melting. *Materials Science and Engineering A*, *639*, pp. 647–655.
54. Gao, Y., Zhang, D., Cao, M., Chen, R., Feng, Z., Poprawe, R., Schleifenbaum, J. H., & Ziegler, S. (2019). Effect of δ phase on high temperature mechanical performances of Inconel 718 fabricated with SLM process. *Materials Science and Engineering A*, *767*, 138327 (13 pp.).
55. Wang, Z., Guan, K., Gao, M., Li, X., Chen, X., & Zeng, X. (2012). The microstructure and mechanical properties of deposited-IN718 by selective laser melting. *Journal of Alloys and Compounds*, *513*, pp. 518–523.
56. Zhang, B., Xiu, M., Tan, Y. T., Wei, J., & Wang, P. (2019). Pitting corrosion of SLM Inconel 718 sample under surface and heat treatments. *Applied Surface Science*, *490*, pp. 556–567.
57. Liu, P., Hu, J., Sun, S., Feng, K., Zhang, Y., & Cao, M. (2019). Microstructural evolution and phase transformation of Inconel 718 alloys fabricated by selective laser melting under different heat treatment. *Journal of Manufacturing Processes*, *39*, pp. 226–232.
58. Zhou, L., Mehta, A., McWilliams, B., Cho, K., & Sohn, Y. (2019). Microstructure, precipitates and mechanical properties of powder bed fused inconel 718 before and after heat treatment. *Journal of Materials Science and Technology*, *35*(6), pp. 1153–1164.
59. Li, X., Shi, J. J., Wang, C. H., Cao, G. H., Russell, A. M., Zhou, Z. J., Li, C. P., & Chen, G. F. (2018). Effect of heat treatment on microstructure evolution of Inconel 718 alloy fabricated by selective laser melting. *Journal of Alloys and Compounds*, *764*, pp. 639–649.
60. Deng, D., Peng, R. L., Brodin, H., & Moverare, J. (2018). Microstructure and mechanical properties of Inconel 718 produced by selective laser melting: Sample orientation dependence and effects of post heat treatments. *Materials Science and Engineering A*, *713*, pp. 294–306.
61. Zhao, J.-R., Hung, F.-Y., & Lui, T.-S. (2020). Microstructure and tensile fracture behavior of three-stage heat treated inconel 718 alloy produced via laser powder bed fusion process. *Journal of Materials Research and Technology*, In press, https://doi.org/10.1016/j.jmrt.2020.01.030.
62. Zhang, D., Niu, W., Cao, X., & Liu, Z. (2015). Effect of standard heat treatment on the microstructure and mechanical properties of selective laser melting manufactured Inconel 718 superalloy. *Materials Science and Engineering A*, *644*, pp. 32–40.
63. Karabulut, Y., Tascioglu, E., & Kaynak, Y. (2019). Heat treatment temperature-induced microstructure, microhardness and wear resistance of Inconel 718 produced by selective laser melting additive manufacturing. *Optik*, In press, https://doi.org/10.1016/j.ijleo.2019 .163907.
64. Pei, C., Shi, D., Yuan, H., & Li, H. (2019). Assessment of mechanical properties and fatigue performance of a selective laser melted nickel-base superalloy Inconel 718. *Materials Science and Engineering A*, *759*, pp. 278–287.
65. Li, X., Shi, J. J., Cao, G. H., Russell, A. M., Zhou, Z. J., Li, C. P., & Chen, G. F. (2019). Improved plasticity of Inconel 718 superalloy fabricated by selective laser melting through a novel heat treatment process. *Materials and Design*, *180*, 107915 (7 pp.).
66. Xu, Z., Murray, J. W., Hyde, C. J., & Clare, A. T. (2018). Effect of post processing on the creep performance of laser powder bed fused Inconel 718. *Additive Manufacturing*, *24*, pp. 486–497.
67. Schaak, C., Tillmann, W., Schaper, M., & Aydinöz, M. E. (2016). Process gas infiltration in Inconel 718 samples during SLM processing. *RteJ. – Fachforum für Rapid Technologies, 2016*, pp. 1-8.
68. Tillmann, W., Schaak, C., Nellesen, J., Schaper, M., Aydinöz, M. E., & Hoyer, K. P. (2017). Hot isostatic pressing of IN718 components manufactured by selective laser melting. *Additive Manufacturing*, *13*, pp. 93–102.
69. Jiang, R., Mostafaei, A., Pauza, J., Kantzos, C., & Rollett, A. D. (2019). Varied heat treatments and properties of laser powder bed printed Inconel 718. *Materials Science and Engineering A*, *755*, pp. 170–180.
70. Amato, K. N., Gaytan, S. M., Murr, L. E., Martinez, E., Shindo, P. W., Hernandez, J., Collins, S., & Medina, F. (2012). Microstructures and mechanical behavior of Inconel 718 fabricated by selective laser melting. *Acta Materialia*, *60*(5), pp. 2229–2239.
71. Raza, T., Andersson, J., & Svensson, L. E. (2018). Microstructure of Selective Laser Melted Alloy 718 in As-Manufactured and Post Heat Treated Condition. *Procedia Manufacturing, 25*, pp. 450–458.

72. Popovich, V. A., Borisov, E. V., Popovich, A. A., Sufiiarov, V. S., Masaylo, D. V., & Alzina, L. (2017). Impact of heat treatment on mechanical behaviour of Inconel 718 processed with tailored microstructure by selective laser melting. *Materials and Design*, *131*, pp. 12–22.
73. Aydinöz, M. E., Brenne, F., Schaper, M., Schaak, C., Tillmann, W., Nellesen, J., & Niendorf, T. (2016). On the microstructural and mechanical properties of post-treated additively manufactured Inconel 718 superalloy under quasi-static and cyclic loading. *Materials Science and Engineering A*, *669*, pp. 246–258.
74. Wang, X., & Chou, K. (2019). The effects of stress relieving heat treatment on the microstructure and residual stress of Inconel 718 fabricated by laser metal powder bed fusion additive manufacturing process. *Journal of Manufacturing Processes*, *48*, pp. 154–163.
75. Appa Rao, G., Srinivas, M., & Sarma, D. S. (2004). Effect of thermomechanical working on the microstructure and mechanical properties of hot isostatically pressed superalloy Inconel 718. *Materials Science and Engineering A*, *383*(2), 201–212.
76. Vrancken, B. Study of Residual Stresses in Selective Laser Melting. Ph.D. Thesis, Faculty of Engineering Science, Arenberg Doctoral School, Leuven, Belgium, 2016.
77. Mercelis, P., & Kruth, J. P. (2006). Residual stresses in selective laser sintering and selective laser melting. *Rapid Prototyping Journal*, *12*(5), pp. 254–265.
78. Kruth, J. P., Deckers, J., Yasa, E., & Wauthlé, R. (2012). Assessing and comparing influencing factors of residual stresses in selective laser melting using a novel analysis method. *Proceedings of the Institution of Mechanical Engineers, Part B: Journal of Engineering Manufacture, 226*(6), pp. 980-991.
79. Ali, H., Ghadbeigi, H., & Mumtaz, K. (2018). Effect of scanning strategies on residual stress and mechanical properties of Selective Laser Melted Ti6Al4V. *Materials Science and Engineering A*, *712*, pp. 175–187.
80. Zaeh, M. F., & Branner, G. (2010). Investigations on residual stresses and deformations in selective laser melting. *Production Engineering*, *4*(1), pp. 35–45.
81. Lu, Y., Wu, S., Gan, Y., Huang, T., Yang, C., Junjie, L., & Lin, J. (2015). Study on the microstructure, mechanical property and residual stress of SLM Inconel-718 alloy manufactured by differing island scanning strategy. *Optics and Laser Technology*, *75*, pp. 197–206.
82. Yi, J. H., Kang, J. W., Wang, T. J., Wang, X., Hu, Y. Y., Feng, T., Feng, Y. L., & Wu, P. Y. (2019). Effect of laser energy density on the microstructure, mechanical properties, and deformation of Inconel 718 samples fabricated by selective laser melting. *Journal of Alloys and Compounds*, *786*, pp. 481–488.
83. Mukherjee, T., Manvatkar, V., De, A., & DebRoy, T. (2017). Mitigation of thermal distortion during additive manufacturing. *Scripta Materialia*, *127*, pp. 79–83.
84. Ahmad, B., van der Veen, S. O., Fitzpatrick, M. E., & Guo, H. (2018). Residual stress evaluation in selective-laser-melting additively manufactured titanium (Ti-6Al-4V) and inconel 718 using the contour method and numerical simulation. *Additive Manufacturing*, *22*, pp. 571–582.
85. Li, C., Liu, J. F., Fang, X. Y., & Guo, Y. B. (2017). Efficient predictive model of part distortion and residual stress in selective laser melting. *Additive Manufacturing*, *17*, pp. 157–168.
86. Liu, Y., Yang, Y., & Wang, D. (2016). A study on the residual stress during selective laser melting (SLM) of metallic powder. *International Journal of Advanced Manufacturing Technology*, *87*(1–4), pp. 647–656.
87. DebRoy, T., Wei, H. L., Zuback, J. S., Mukherjee, T., Elmer, J. W., Milewski, J. O., Beese, A. M., Wilson-Heid, A., De, A., & Zhang, W. (2018). Additive manufacturing of metallic components – Process, structure and properties. *Progress in Materials Science, 92*, pp. 112-224.
88. Anderson, L. S., Venter, A. M., Vrancken, B., Marais, D., van Humbeek, J., & Becker, T. H. (2018). Investigating the Residual Stress Distribution in Selective Laser Melting Produced Ti-6Al-4V using Neutron Diffraction. *Materials Research Forum LLC, 4*, pp. 73-78.
89. Vrancken, B., Cain, V., Knutsen, R., & Van Humbeeck, J. (2014). Residual stress via the contour method in compact tension specimens produced via selective laser melting. *Scripta Materialia*, *87*, pp. 29–32.
90. Shiomi, M., Osakada, K., Nakamura, K., Yamashita, T., & Abe, F. (2004). Residual stress within metallic model made by selective laser melting process. *CIRP Annals - Manufacturing Technology*, *53*(1), pp. 195–198.
91. Ding, J., Colegrove, P., Mehnen, J., Ganguly, S., Almeida, P. M. S., Wang, F., & Williams, S. (2011). Thermo-mechanical analysis of Wire and Arc Additive Layer Manufacturing process on large multi-layer parts. *Computational Materials Science*, *50*(12), pp. 3315–3322.
92. Williams, R. J., Davies, C. M., & Hooper, P. A. (2018). A pragmatic part scale model for residual stress and distortion prediction in powder bed fusion. *Additive Manufacturing*, *22*, pp. 416–425.
93. Denlinger, E. R., Gouge, M., Irwin, J., & Michaleris, P. (2017). Thermomechanical model development and in situ experimental validation of the Laser Powder-Bed Fusion process. *Additive Manufacturing*, *16*, pp. 73–80.
94. Ghosh, S., & Choi, J. (2007). Deposition pattern based thermal stresses in single-layer laser aided direct material deposition process. *Journal of Manufacturing Science and Engineering, Transactions of the ASME*, *129*(2), pp. 319–332.
95. Cottam, R., Wang, J., & Luzin, V. (2014). Characterization of microstructure and residual stress in a 3D H13 tool steel component produced by additive manufacturing. *Journal of Materials Research*, *29*(17), pp. 1978–1986.
96. Barros, R., Silva, F. J. G., Gouveia, R. M., Saboori, A., Marchese, G., Biamino, S., Salmi, A., & Atzeni, E. (2019). Laser Powder Bed Fusion of Inconel 718: Residual Stress Analysis Before and After Heat Treatment. *Metals, 9*(12), 1290 (17 pp.).
97. Gong, X., Anderson, T., & Chou, K. (2014). Review on powder-based electron beam additive manufacturing Technology. *Manufacturing Review, 1*, pp. 1-12.
98. Prabhakar, P., Sames, W. J., Dehoff, R., & Babu, S. S. (2015). Computational modeling of residual stress formation during the electron beam melting process for Inconel 718. *Additive Manufacturing*, *7*, pp. 83–91.

99. Smith, C. J., Derguti, F., Hernandez Nava, E., Thomas, M., Tammas-Williams, S., Gulizia, S., Fraser, D., & Todd, I. (2016). Dimensional accuracy of Electron Beam Melting (EBM) additive manufacture with regard to weight optimized truss structures. *Journal of Materials Processing Technology*, *229*, pp. 128–138.
100. Gokuldoss, P. K., Kolla, S., & Eckert, J. (2017). Additive manufacturing processes: Selective laser melting, electron beam melting and binder jetting-selection guidelines. *Materials, 10*(6), 672 (12 pp.).
101. Sochalski-Kolbus, L. M., Payzant, E. A., Cornwell, P. A., Watkins, T. R., Babu, S. S., Dehoff, R. R., Lorenz, M., Ovchinnikova, O., & Duty, C. (2015). Comparison of Residual Stresses in Inconel 718 Simple Parts Made by Electron Beam Melting and Direct Laser Metal Sintering. *Metallurgical and Materials Transactions A: Physical Metallurgy and Materials Science*, *46*(3), pp. 1419–1432.
102. Nadammal, N., Cabeza, S., Mishurova, T., Thiede, T., Kromm, A., Seyfert, C., Farahbod, L., Haberland, C., Schneider, J. A., Portella, P. D., & Bruno, G. (2017). Effect of hatch length on the development of microstructure, texture and residual stresses in selective laser melted superalloy Inconel 718. *Materials and Design*, *134*, pp. 139–150.
103. Luo, Z., & Zhao, Y. (2018). A survey of finite element analysis of temperature and thermal stress fields in powder bed fusion Additive Manufacturing. *Additive Manufacturing, 21*, pp. 318-332.
104. Wang, Z., Denlinger, E., Michaleris, P., Stoica, A. D., Ma, D., & Beese, A. M. (2017). Residual stress mapping in Inconel 625 fabricated through additive manufacturing: Method for neutron diffraction measurements to validate thermomechanical model predictions. *Materials and Design*, *113*, pp. 169–177.
105. Williams, R. J., Davies, C. M., & Hooper, P. A. (2018). A pragmatic part scale model for residual stress and distortion prediction in powder bed fusion. *Additive Manufacturing*, *22*, pp. 416–425.
106. Hodge, N. E., Ferencz, R. M., & Vignes, R. M. (2016). Experimental comparison of residual stresses for a thermomechanical model for the simulation of selective laser melting. *Additive Manufacturing*, *12*, pp. 159–168.
107. Song, B., Dong, S., Liao, H., & Coddet, C. (2012). Process parameter selection for selective laser melting of Ti6Al4V based on temperature distribution simulation and experimental sintering. In *International Journal of Advanced Manufacturing Technology, 61*, pp. 967–974.
108. Song, X., Feih, S., Zhai, W., Sun, C. N., Li, F., Maiti, R., Wei, J., Yang, Y., Oancea, V., Brandt, L. R., & Korsunsky, A. M. (2020). Advances in additive manufacturing process simulation: Residual stresses and distortion predictions in complex metallic components. *Materials and Design, 193*, pp. 1-14.
109. Siewert, M., Neugebauer, F., Epp, J., & Ploshikhin, V. (2019). Validation of Mechanical Layer Equivalent Method for simulation of residual stresses in additive manufactured components. *Computers and Mathematics with Applications*, *78*(7), pp. 2407–2416.

ARTICLE 2: A REVIEW OF HEAT TREATMENTS ON IMPROVING THE QUALITY AND RESIDUAL STRESSES OF THE Ti-6Al-4V PARTS PRODUCED BY ADDITIVE MANUFACTURING

Review - Metals ***2020****, 10, 1006; doi:10.3390/met10081006*

A Review of Heat Treatments on Improving the Quality and Residual Stresses of the Ti-6Al-4V Parts Produced by Additive Manufacturing

Óscar Teixeira [1], Francisco J. G. Silva [1,*], Luís P. Ferreira [1], and Eleonora Atzeni [2]

[1] ISEP—School of Engineering, Polytechnic of Porto, Rua Dr. António Bernardino de Almeida, 431, 4249—015 Porto, Portugal; oscarfrmteixeira96@gmail.com (O.T.); luispintoferreira@eu.ipp.pt (L.P.F.)
[2] Department of Management and Production Engineering (DIGEP), Politecnico di Torino, Corso Duca degli Abruzzi, 24, 10129 Torino (TO), Italy; eleonora.atzeni@polito.it (E.A.)
* Correspondence: fgs@isep.ipp.pt; Tel.: +351-228340500

Received: date; Accepted: date; Published: date

Abstract: Additive manufacturing (AM) can be seen as a disruptive process that builds complex components layer upon layer. Two of its distinct technologies are Selective Laser Melting (SLM) and Electron Beam Melting (EBM) which are powder bed fusion processes that create metallic parts with the aid of a beam source. One of the most studied and manufactured superalloys in metal AM is the Ti-6Al-4V which can be applied in the aerospace field due to its low density and high melting point, and biomedical area owing to its high corrosion resistance and excellent biocompatibility when in contact with tissues or bones of the human body. The research novelty of this work is the aggregation of all kinds of data from the last 20 years of investigation about Ti-6Al-4V parts manufactured via SLM and EBM, namely information related to residual stresses (RS), as well as the influence played by different heat treatments in reducing porosity and increasing mechanical properties. Throughout the report, it can be seen that the expected microstructure of the Ti-6Al-4V alloy is different in both manufacturing processes, mainly due to the distinct cooling rates. However, heat treatments can modify the microstructure, reduce RS, increase the ductility, fatigue life, and hardness of the components. Furthermore, distinct post-treatments can induce compressive RS on the part's surface, consequently, enhancing the fatigue life.

Keywords: Additive Manufacturing; Metal Powder Bed Fusion; Selective Laser Melting; Electron Beam Melting; Ti-6Al-4V; Residual Stresses; Heat Treatments; Microstructure.

1. Introduction

Additive manufacturing (AM), also known by many as three-dimensional printing (3DP), was born in 1981 through Hideo Kodama [1] and can be described, according to the International Organization for Standardization (ISO) 52900-15 standard [2], as a manufacturing process that creates 3D objects from scratch, typically layer after layer. As a matter of fact, this technology can be seen as a disruptive one, as it completely changed the creation of parts through the addition of material instead of the common subtraction of it, something that is characteristic of subtractive manufacturing [3]. Furthermore, it can be classified as a sustainable process as it enables the production of complex geometry components with minimal waste of material [4]. One of the process categories associated with this new manufacturing process is called Powder Bed Fusion, which agglomerates three distinct technologies, namely Selective Laser Sintering (SLS), Selective Laser Melting (SLM), and Electron Beam Melting (EBM) (Figure 1) [5]. However, if one desires to produce exclusively metal components then it must employ the last two mentioned technologies. Thus, from now on, this paper review will solely focus on SLM and EBM, as they are seen as metal Powder Bed Fusion technologies.

In fact, SLM appeared in 1996 through Wilhelm Meiners, Konrad Wissenbach, and Andres Gasser [6] and is a process that must be done in a closed chamber surrounded by an inert gas, such as argon or nitrogen, to avoid oxidation of the material after melting, remove spatter, metal vapor, and plasma plumes [7-10]. In addition, the parts are usually connected to a substrate plate by support structures, in order to reduce deformations when manufacturing. The operating method is done by firstly heating up the building platform in order to reduce deformations caused by temperature differences (only on some machines), then the powder cartridge rises, thanks to an actuator, and dispenses a predefined amount of powder. After that, the levelling roller/blade creates a uniform layer of powder on the construction platform and places the substrate excess in another cartridge opposite the first one and then, a high energy density laser melts the powder forming a melt pool of approximately 100 μm width [11]. Finally, the construction platform lowers according to the thickness of each layer, which usually varies between 20 and 100 μm depending on the material, and the process is repeated until the final part is completed [12].

ARCAM was founded in 1997 and is the only enterprise that manufactures EBM machines, as they own the patent [13]. This technology uses accelerated electrons in the order of 0.1 to 0.4 times the speed of light [14] as a beam source and the process is done in a vacuum chamber [15]. Furthermore, the additive manufacturing steps are the same as the SLM technology, however, the temperature of the build chamber is much higher (500-800 °C) [16-19], hence, one should expect fewer residual stresses (RS) because of the lower temperature gradient during manufacturing ($T_{melt} – T_{ambient}$). In addition, the typical layer thickness of the parts is between 50 μm and 200 μm, due to the deeper penetration and higher energy of the beam, making the manufacturing process quicker than SLM [16].

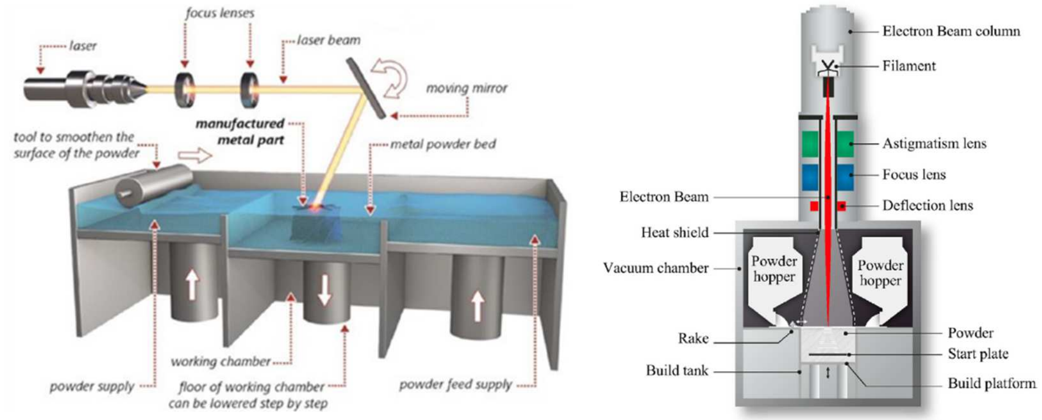

a) b)

Figure 1 - Main components of a) SLM machine, b) EBM machine. Adapted from [20]. Original sources: (a) Empa, (b) Arcam

Titanium alloys have been receiving special attention from the aerospace industry, thanks to the low density and the high melting point of this material (around 1650 °C) [21]. In other words, several companies turn to titanium when they need a light component capable of safely supporting high loads and/or when working temperatures are high [22]. In addition, it has also a high corrosion resistance [23-25], and often used in medical implants due to its excellent biocompatibility when in contact with tissues or bones of the human body [26]. Note that this material is quite difficult and expensive to machine, so its use and diffusion in AM is of great interest [27,28]. In fact, the titanium alloy most studied by the scientific community and used to manufacture final components is Ti-6Al-4V (UNS R56400) [29]. The crystalline structure of this alloy is composed of a compact hexagonal structure (phase α) and body-centred cubic (phase β). The existence of aluminium and vanadium causes the α and β phases to stabilize, respectively, maintaining the dual-phase at room temperature [22]. In general, the microstructure, when depositing material, presents a martensitic phase (α') due to the rapid cooling of the manufacturing process. In addition to the quick cooling, the α' phase will only form if the build temperature is kept below the martensite start temperature (Ms) [30]. The aforementioned temperature varies from 575 °C up to 800 °C [31-33] as the impure elements along with the initial microstructure and composition homogeneity affect the Ms temperature [34]. In Figure 2 it is possible to analyse how the phase transformation is affected by the distinct cooling rates, i.e. in the region of 525-410 °C/s the α' phase will be formed, however, if the cooling rate is kept under 20 °C/s it will lead to the formation of the phase α.

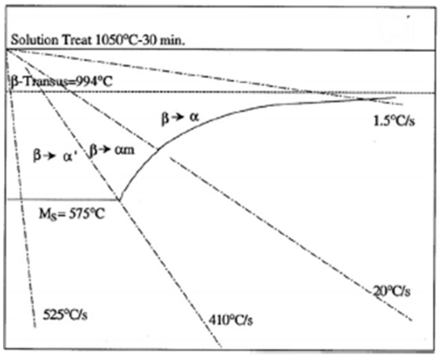

Figure 2 - Diagram that explains how the cooling rate affects the phase transformation. Obtained from [35]

In laser-based additive manufacturing processes, RS are induced by thermal principles as the gradient temperature is high because of the heating and thermal expansion upon deposition of a new layer, and its subsequent cooling and contraction [36]. Therefore, production errors in the components might occur due to geometrical distortion. Thus, it is mandatory to understand the expected orientation and magnitude of the RS in order to do accurate predictions of the final part properties. Moreover, high magnitude (100-500 MPa) RS are more prone to occur in the SLM rather than in the EBM process [37].

As a matter of fact, residual stresses can be divided into three different types, Type I, II, and III, depending on the operational length scale, Figure 3. Type I are macroscopic stresses that act on the scale of component geometry, Type II, often called intergranular stresses, are micro-stresses acting at the individual grain scale, and Type III act at the atomic scale [38]. Nowadays, multiple techniques are employed to measure residual stresses and they can be divided into two major groups, destructive, and non-destructive testing. In one hand, if one seeks to find residual stresses located on the surface level in a non-destructive way, X-Ray Diffraction (XRD) is one of the most suitable techniques for that effect due to its great accuracy (± 20 MPa), and the large variety of equipment available [39]. On the other hand, if the goal is to investigate internal residual stresses in a destructive way, one can use the stripping method, crack compliance method, or the contour method. Furthermore, there is also an economic semi-destructive way to discover surface residual stresses called hole-drilling strain-gage method [40]. It is considered a semi-destructive method as it does not affect, in a significant way, the structural integrity of the part. Currently an ISO standard does not exist, however, according to American Society for Testing and Materials (ASTM) E837-08 [41] standard, the aforementioned method can be described as a technique that computes residual stresses near the surface of a material by sticking a strain rosette to the part's surface and then drilling a hole at the centre of the rosette which later determines the relieved strains.

The research novelty of this work is the aggregation of all kinds of information from the last 20 years of research about the Ti-6Al-4V alloy in a structured way, namely information related to residual stresses, as well as the influence played by different heat treatments in reducing porosity, increasing mechanical properties, and stress relief of additive manufactured components. The authors strongly believe that the compilation of the aforementioned data is essential because it allows to understand the research evolution of this titanium alloy, and provides a good starting point for those who want to learn about additive manufacturing. Furthermore, the reading of this review paper can also be useful to understand some key aspects of the Ti-6Al-4V alloy, thus improving the quality and performance of the manufactured parts.

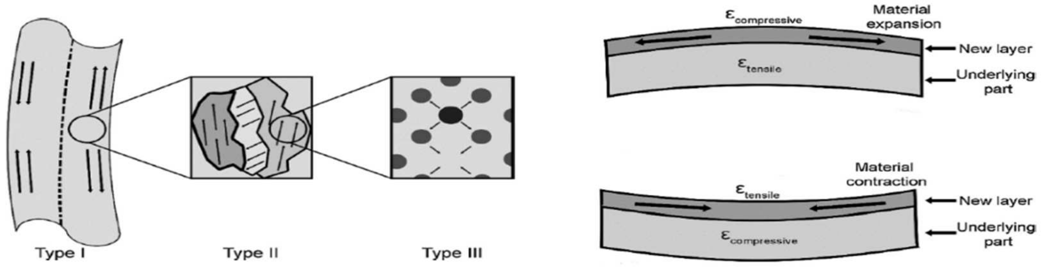

a) b)

Figure 3 - a) Residual stresses classification, and b) plastic deformation development. Adapted from [36]

2. Methodology

The methodology followed in this article started with the selection of the theme, which is heat treatments and residual stresses on metal powder bed fusion Ti-6Al-4V parts. In this way, the authors tried to analyse the amount of information available on the ScienceDirect platform in order to get a general idea of the number of articles published on this topic. When performing an advanced search by title, abstract, and keywords on the topics “Additive Manufacturing + Ti-6Al-4V”, 537 articles were found, being only 11 of them review articles, Figure 4.

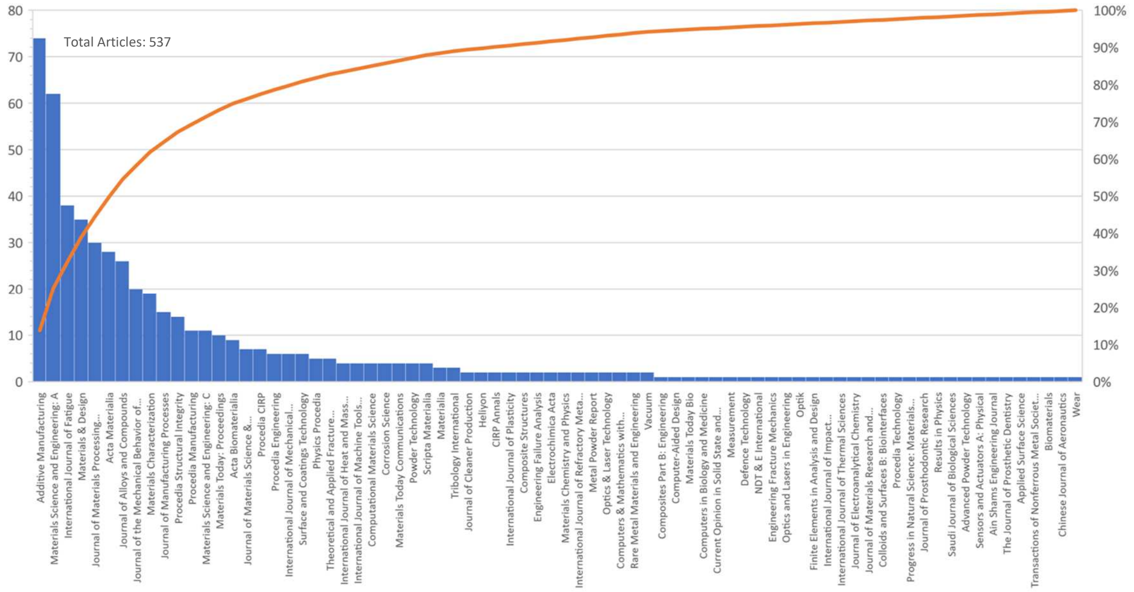

Figure 4 - Pareto’s chart of the research "Additive Manufacturing + Ti-6Al-4V" on ScienceDirect

Then, after a thorough research for the topics “Heat Treatments + Selective Laser Melting + Ti-6Al-4V”, Figure 5a, it was concluded that the number of results had decreased considerably, with a total of 61 research articles. After that, the authors searched for “Residual Stresses + Selective Laser Melting + Ti-6Al-4V”, Figure 5b, and found that there were only 31 research articles. Lastly, the authors removed the word “Selective Laser Melting” on the last two searches and added the word “Electron Beam Melting”, and found out 18 articles about heat treatments and 10 about residual stresses, Figure 6. Note that, if the research had not been done in an advanced way, the results would have been much higher, however, more than 50 % of the results would not be relevant for this review article.

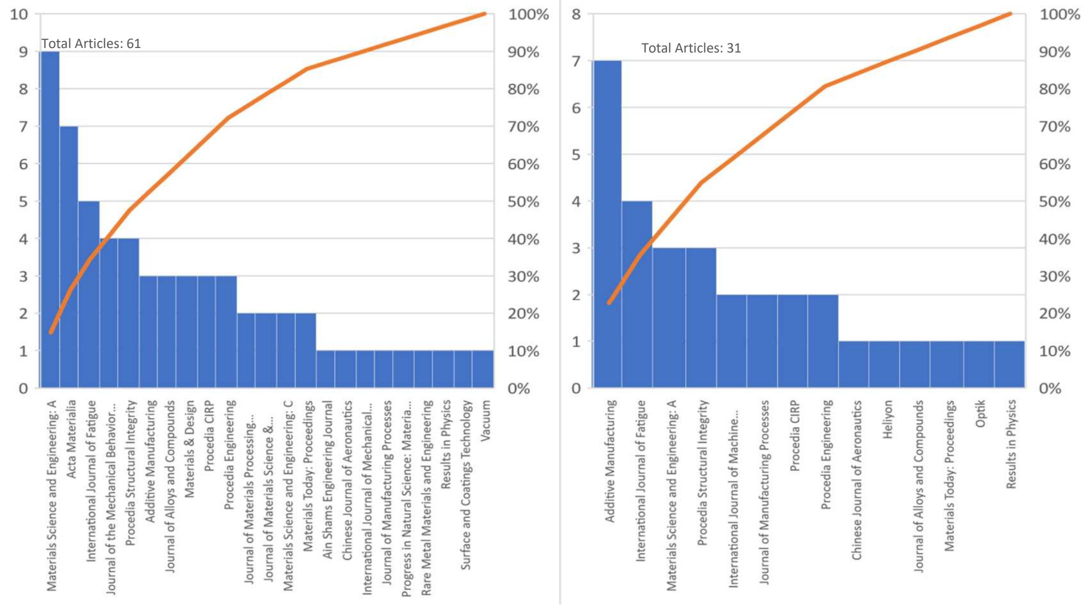

a) b)

Figure 5 – Pareto’s charts of the research, a) “Heat Treatments + Selective Laser Melting + Ti-6Al-4V”, and b) "Residual Stresses + Selective Laser Melting + Ti-6Al-4V", on ScienceDirect

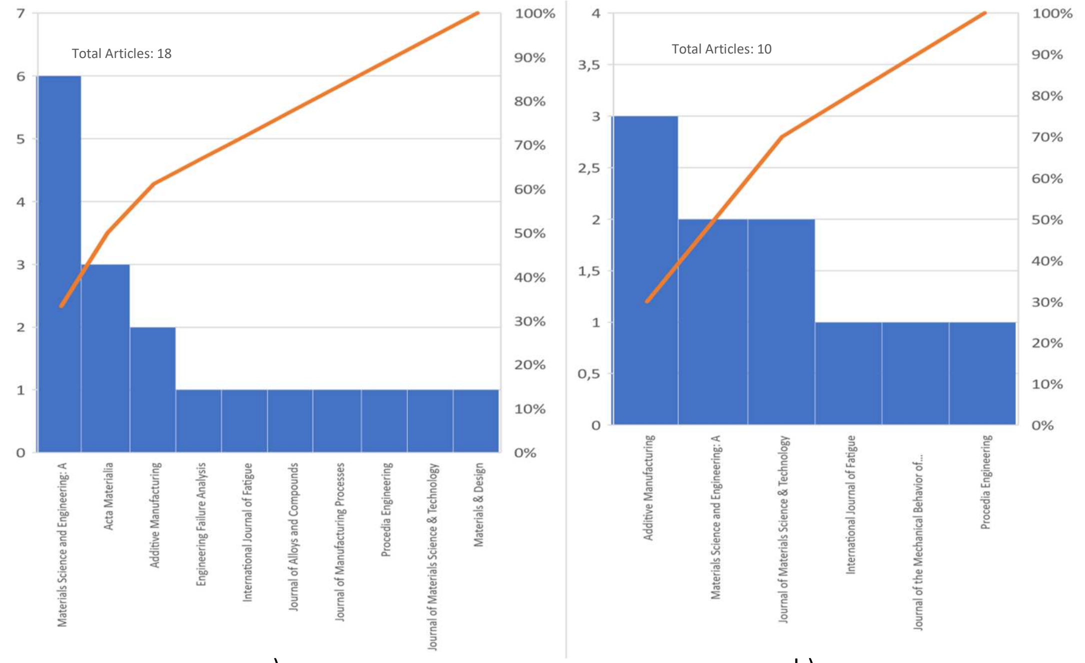

a) b)

Figure 6 – Pareto’s charts of the research, a) “Heat Treatments + Electron Beam Melting + Ti-6Al-4V”, and b) "Residual Stresses + Electron Beam Melting + Ti-6Al-4V", on ScienceDirect

3. Literature Review

Before heading to the first subsection of the literature review, the authors thought that the SLMed and EMBed as-built microstructure of the titanium alloy should be compared as it is heavily dependent on the manufacturing process. Furthermore, it also plays a crucial role in governing the material properties of the components. Therefore, several investigators studied the as-built microstructure of SLMed titanium samples [42-46]. Thijs et al. [42] reported that all the as-built specimens produced via SLM showed a microstructure with fine acicular α′ precipitates in columnar original β grains, due to the rapid cooling of the manufacturing process, Figure 7a. Similarly, Facchini et al. [43] and Gong et al. [44] found the same microstructure results as the aforementioned study, while Benedetti et al. [45] reported that the as-built titanium specimens had a very fine acicular α′ microstructure. On the contrary, Xu et al. [46] managed to accomplish an ultrafine lamellar α + β structure of SLMed titanium as-built specimens without having notable grain coarsening. The authors used the following process variables: layer thickness of 60 μm, focal offset distance of 2 mm, and energy density of 50.62 J/mm^3 and reported that a careful selection of the printing parameters was the key for such microstructure.

Several other authors studied the microstructure of as-built titanium specimens produced via EBM [47-51]. Xu et al. [47] reported that an α + β lamellar microstructure, Figure 7b, was achieved for the following processing parameters: accelerated voltage of 60 kV, beam current of 10 mA, filament current of 432 mA, focus current of 670 mA, gun vacuum pressure of 3,4 x 10^{-3} Pa, chamber vacuum pressure of 7 x 10^{-2} Pa, and work distance of 150 mm. Likewise, Galarraga et al. [48], Zhao et al. [49], Chern et al. [50], and Murr et al. [51] found an α + β lamellar microstructure in the EBMed as-built specimens.

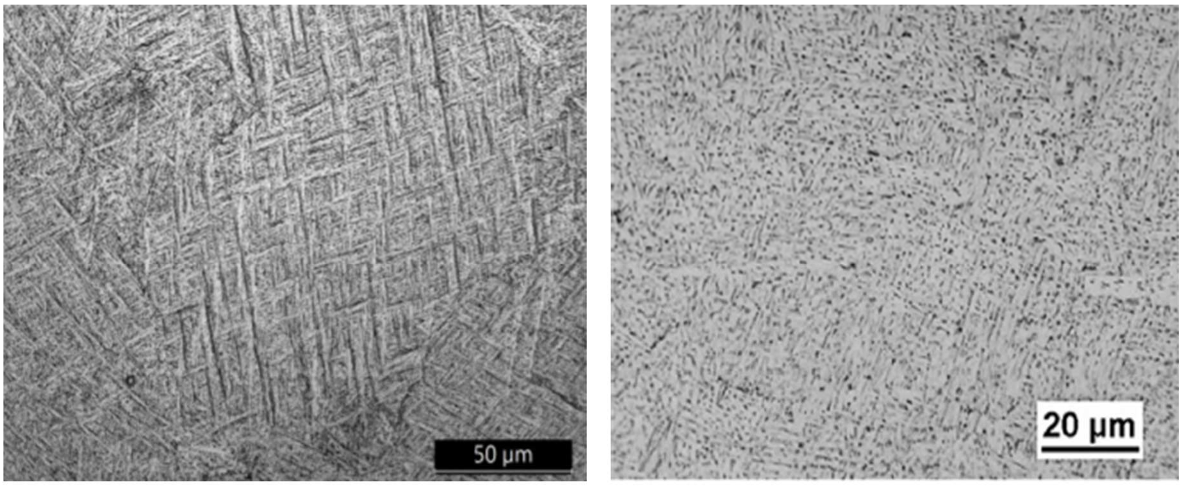

a) b)

Figure 7 - Characteristic microstructure of a) SLM process (fine acicular α' in columnar original β grains), and b) EBM process (α + β lamellar). Obtained from [45,48], respectively

Furthermore, it is also relevant to understand the influence played by distinct additive manufacturing processes on the mechanical properties, profile surface roughness (Ra), and porosity of Ti-6Al-4V components. Thus, in Table 1 it is possible to analyse the distinct as-built mechanical properties of titanium samples. From the aforementioned table, it is worth noting that the SLMed samples, when compared to the EBMed ones, exhibit a 20 to 30 % increase of the yield strength (YS) and ultimate tensile strength (UTS), however, the ductility is much lower due to inherent rapid cooling of the SLM process which promotes an α′ martensitic microstructure within long columnar prior β grains. Regarding the Ra, it is known that different scan speeds, powder sizes, and layer thicknesses of the EBM and SLM manufacturing processes promote distinct surface roughness [35]. Edwards et al. [52] stated that the titanium specimens produced via SLM had a Ra between 32 and 38.5 μm, depending on the build orientation. Moreover, Chan et al. [53] compared the surface roughness of Ti-6Al-4V samples manufactured via SLM and EBM and reported that the latter manufacturing process revealed a Ra of 131 μm, while the former presented 38.5 μm. The authors associated the high surface roughness of the EBMed sample to the presence of unfilled gaps and unmelted powder attached to the surface. Fousová et al. [54] studied the effect of internal defects and surface roughness on the mechanical properties of Ti-6Al-4V samples produced via SLM and EBM. In order to achieve a similar microstructure as the EBM as-built specimens, the SLM ones underwent a heat treatment at 820 °C for 5.5 hours. After analysing the microstructure and conducting a uniaxial tension test and a fatigue test, the authors reported that both EBMed and SLMed specimens exhibited a two-phase lamellar microstructure, however, internal defects were distinct due the manufacturing process. EBMed samples showed spherical pores resulting from gas entrapment, while SLMed ones revealed insufficient melting defects. Despite that, the researchers concluded that the static properties in tension of both samples reached comparable values, but the fatigue test demonstrated that the SLMed specimens exhibited a greater fatigue strength (220 ± 24 MPa) than the EBMed ones (115 ± 13 MPa) due to the lower surface roughness. Besides, Qiu et al. [55] studied the effect of laser power and layer thickness on surface roughness and porosity level of SLMed titanium as-built samples. The researchers reported that a low layer thickness combined with a high laser power leads to the production of specimens with a porosity level inferior to 1 vol%. In fact, when it comes to part porosity, several authors [44,49,56] reported that in the SLM process one should expect porosities between 0.1 and 0.5 vol% while others [44,57] stated that components produced through EBM present an inherent porosity between 0.1 and 0.3 vol%. Recently, Ning et al. [58] created an analytical model based on the relationship between porosity evolution and thermal behaviour of the material, which predicted part porosity in metal powder bed additive manufacturing without resorting to any iteration-based simulations or Finite Element Modelling (FEM). For that, the authors followed the algorithm that can be seen in Figure 8. The molten pool dimensions were computed through the comparison of the material's melting temperature with the expected temperatures using an analytical thermal model. The porosity evaluation was computed by subtracting the volume fraction of the powder bed void from the post-processed porosity of the part. The volume fraction of the powder was investigated by image analysis and through an advancing front approach. Then, after determining the analytical results of the expected porosity, the authors compared the values with additively manufactured Ti-6Al-4V specimens from the literature and concluded that their model could predict porosity with a high amount of precision. Furthermore, the authors stated that the computational time of the model was short, allowing a quick and precise prediction for distinct processing parameters.

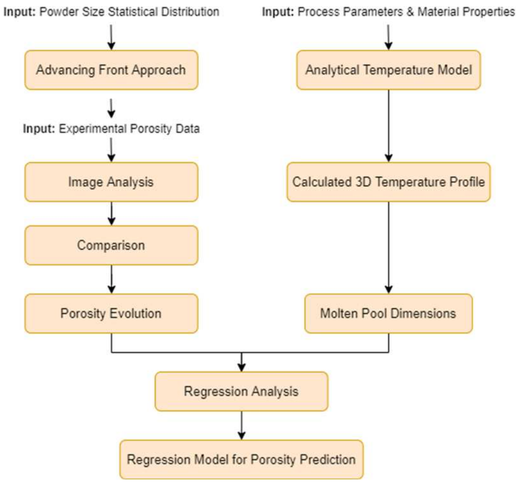

Figure 8 - Schematic illustration of the algorithm used in the porosity prediction model. Adapted from [58]

In another report, Zhang et al. [59] studied and compared the wear resistance of as-built SLM, as-built EBM, and forged Ti-6Al-4V samples. Then, the authors performed friction and wear tests to the three types of samples and concluded that, when compared to the forged specimens, the additively manufactured ones exhibited a better wear resistance owing to their weaker delamination and higher hardness. Moreover, the SLMed samples showed a higher wear rate than the EBMed ones due to the higher number of horizontal cracks of the former, Figure 9.

Table 1 - Mechanical properties of as-built Ti-6Al-4V specimens in tensile testing

Manufacturing Process	YS [MPa]	UTS [MPa]	ε [%]	Ref.
EBM	881 ± 12.5	978.5 ± 11.5	10.7 ± 1.5	[60]
EBM	851.8 ± 5.8	964.5 ± 0.3	16.3 ± 0.8	[61]
SLM	1056 ± 29	1351 ± 34	5.5 ± 0.8	[62]
SLM	1143 ± 30	1219 ± 20	4.9 ± 0.6	[63]

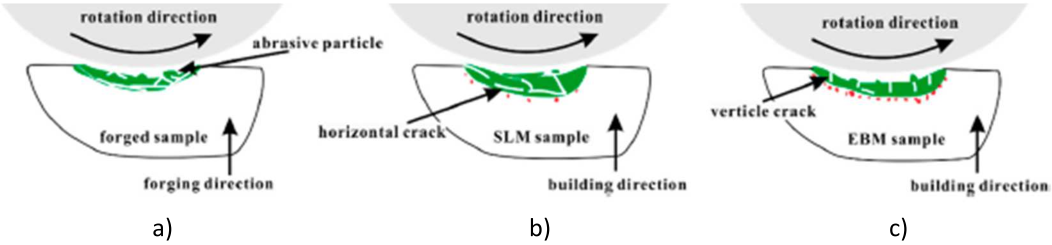

Figure 9 - Wear mechanisms in the Ti-6Al-4V samples built by a) forging, b) SLM, and c) EBM. Obtained from [59]

3.1. Heat Treatments

Heat treatments are known for reducing residual stresses, improve mechanical properties, and changing the microstructure of titanium components. Balyakin et al. [64] studied the heat treatment effect on the surface roughness of titanium specimens manufactured via SLM. The researchers conducted distinct heat treatments followed by mechanical brushing and chemical polishing and reported that, after heating the samples to 950 °C for 30 minutes followed by oil quenching and subsequent aging at 650 °C for 120 minutes, the specimens exhibited the worst surface roughness (Ra = 4.41 μm) measured just before undergoing mechanical polishing and chemical polishing, whilst the best final surface roughness (Ra = 0.27 μm) was achieved through the following preliminary heat treatments: annealing at 650 °C for 120 minutes followed by furnace cooling (FC) plus heating up to 950 °C for 30 minutes followed by water quenching (WQ). Vayssette et al. [65] investigated the roughness influence on multiaxial high-cycle fatigue of titanium samples manufactured via SLM and EBM. Firstly, when producing the specimens, the authors used processing parameters that minimized the RS formation due to high-thermal gradients. Secondly, the samples were post-treated with a stress relief heat treatment followed by Hot Isostatic Pressing (HIP) which aimed to reduce part's porosity. After that, the researchers analysed the microstructure and reported that both samples exhibited a lamellar microstructure with a mean 2 μm lamella size. Then, the authors measured the Ra of both samples before and after chemical polishing, which for the SLM samples was 18.9 μm and 11.2 μm, and for the EBM 38.9 μm and 17.7 μm, respectively. Finally, the researchers conducted fatigue tests and reported that, despite the roughness improvement induced by the chemical etching, the fatigue properties did not improve significantly. Similarly, Yuan et al. [66] investigated the heat treatment effect on the compressive fatigue properties of titanium samples produced via EBM. For that, after manufacturing the samples, the authors conducted an annealing treatment with three different temperatures (750 °C, 850 °C, and 950 °C) for 1.5 hours followed by FC to room temperature. Then, they compared the as-built microstructure to the post-treated one and concluded that the heat treatment promoted the decomposition of the acicular α' martensite into an α + β phase. After conducting fatigue tests, the researchers concluded that when annealing at 950 °C, near the phase boundary, the width of the α lamellae coarsens up to 20 μm and promotes a ductility improvement of the struts, an increase of the fatigue strength, and the fatigue endurance ratio raises to nearly 0.6 which is almost three times more than the reported in another work [67].

Several authors [68-73] studied the fatigue properties of the titanium alloy manufactured via metal powder bed fusion. Chastand et al. [68] investigated the influence of different manufacturing processes, build orientation, surface roughness, and HIP treatment on the fatigue life of titanium samples. To do that, the researchers manufactured several specimens in SLM and EBM machines with different build orientations, namely XY and Z. Then, all the SLMed specimens underwent a stress relief treatment at 640 °C for 4 hours, while others undertook a stress relief + HIP treatment at 920 °C under 1020 bar for 2 hours. After that, the authors conducted the same HIP treatment to 12 EBMed specimens and then machined and polished the surface of several SLMed and EBMed samples. After conducting the fatigue tests, Chastand et al. [68] reported that the manufacturing processes (SLM and EBM) effect is negligible on the fatigue properties as a similar type of defects were found in both cases. Moreover, machining and polishing improved the fatigue properties of the titanium alloy because it lowered the surface roughness and removed superficial defects. Furthermore, the HIP treatment led to the size decrease of the internal defects, hence improving the fatigue properties. To conclude, the authors also reported that the effect of the build direction highly depends on the presence of unmelted zones. In a similar study, Wu et al. [71] investigated the porosity and HIP treatment effect on the fatigue endurance ratio of SLMed titanium samples. For that, the researchers purposely manufactured cellular structures with three different porosities (33 vol%, 50 vol%, and 84 vol%) and then subjected some of them to a HIP treatment at 1000 °C and a pressure of 150 MPa for 1 hour. After studying the microstructure, the authors reported that the heat treatment promoted the transformation of the martensitic microstructure into a lamellar α + β phase. Then, the researchers conducted fatigue tests and concluded that the porosity increase in the as-built samples led to a decrease in the fatigue endurance ratio, Figure 10, due to the low ductility of α'. However, in the HIPed samples, as the porosity increased from 33 vol% to 50 vol%, the fatigue endurance ratio at 10^6 cycles increased from 0.5 up to nearly 0.55, Figure 10. Moreover, when compared to the as-built specimens, the HIPed ones exhibited far better fatigue endurance ratios as the porosity increased. Similarly, Vispoli et al. [72] investigated the surface roughness effect on the fatigue behaviour of Ti-6Al-4V samples produced via SLM. The authors reported that the fatigue resistance of the as-built specimens, when compared to the machined ones, evidenced a drastic reduction due to the elevated roughness.

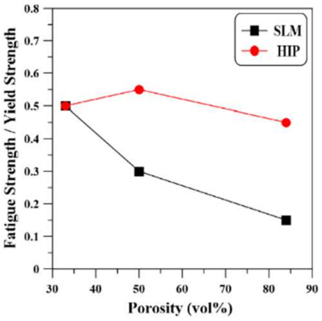

Figure 10 - Porosity influence on the fatigue endurance ratios at 10^6 cycles of as-built and HIPed specimens. Obtained from [71]

Likewise, Yu et al. [73] studied the influence of distinct heat treatments and surface finishing processes on the fatigue performance of titanium samples produced via SLM. The authors employed four different finishing processes, namely turning, 400 mesh sandpaper grinding, 400 mesh sandpaper grinding + sandblasting, and polishing. Furthermore, the researchers also conducted three distinct heat treatments, which can be seen in Table 2. After the fatigue tests, the authors concluded that all the surface finishing processes reduced the as-built arithmetic mean roughness (Ra = 12.16 μm), hence significantly improving the fatigue performance of the samples. Furthermore, as is possible to analyse in Figure 11a, when compared to the as-built specimens, the HIPed and HT-920 ones showed a lower YS and UTS, however, the ductility was greatly improved. On the contrary, the HT-850-550 specimens showed no obvious reduction in the YS and UTS when compared to the as-built ones, and the ductility of the former specimens was also better than the latter. Finally, the heat treatments promoted the increase of the fatigue limit, as the HT-920 and HT-850-550 samples exhibited a stress amplitude of ~400 MPa for 10^6 cycles and the HIPed samples showed a stress amplitude of ~500 MPa for the same number of cycles, Figure 11b.

Table 2 - Distinct heat treatments performed by Yu et al. [73]

Code Name in Figure a	Condition
SLMed	As-built
HIPed	HIP at 920 °C and a pressure of 100 MPa for 2 hours
HT-920	Heat treatment at 920 °C for 2 hours followed by FC
HT-850-550	Double heat treatment, firstly done at 850 °C for 2 hours followed by WQ and then 550 °C for 4 hours followed by AC

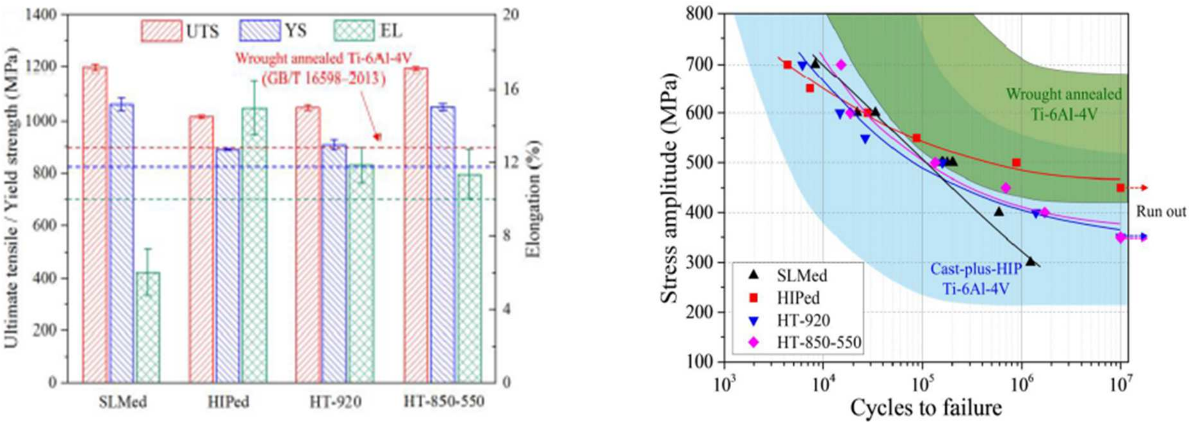

a) b)

Figure 11 - a) Tensile properties and elongation of the different specimens, b) Fatigue performances of the distinct specimens. Adapted from [73]

Kim et al. [74] investigated the effect of microstructure control trough heat treatments on the high temperature creep behaviour of Ti-6Al-4V specimens manufactured via SLM. The authors conducted a heat treatment at 1040 °C for 1 hour and then, analysed the microstructure of the as-built and heat-treated specimens. The former exhibit a typical martensitic microstructure while the latter showed a β phase at the interface of a large α colony area, meaning that a Widmanstätten's structure was formed. Subsequently, the researchers did two different mechanical tests, namely a compressive test at 500 °C and a high temperature creep test, and reported that the compressive yield strength of the as-built specimens was approximately 930 MPa and in the heat-treated specimens was 557 MPa. Nevertheless, the high temperature creep test results confirmed that the heat-treated samples exhibited a lower steady-state creep rate, proving that the martensitic microstructure has a lower creep performance than the Widmanstätten one.

In a different study, Ettefagh et al. [75] investigated the influence of the annealing heat treatment on the corrosion resistance of SLMed titanium components. For that, the authors conducted two distinct post-treatments at 600 °C and 800 °C for 2 hours. The microstructure analysis revealed that the heat treatment done at 600 °C did not provide the proper condition for the vanadium diffusion, hence the microstructure remained similar to the as-built one (α' needle-like). However, the 800 °C heat-treatment led to the formation of the β phase and the stress relief of the α' phase. Then, the researchers performed the corrosion tests and ascertained that as-built specimens corrosion rate was nearly 16 times worse than the cold-rolled commercial titanium samples, which were used as a benchmark. Moreover, the martensitic phase stress relief and the formation of the β phase on the 800 °C post-treated samples greatly improved the corrosion behaviour of the material, which exhibited results comparable to the benchmark.

Wang et al. [76] studied the heat treatment effect on the biocompatibility and osseointegration of SLMed titanium samples. For that, the researchers employed an annealing treatment at a temperature of 820 °C for 4 hours to half of the manufactured specimens. Then, all the specimens were ultrasonic degreased in acetone and anhydrous ethanol baths for 1 hour, respectively. Later, the authors applied human bone mesenchymal stem cells (hBMSCs) to both types of specimens and measured cell proliferation on the first, fourth, and seventh day of incubation and reported that the heat-treated specimens showed a significant enhancement of hBMSCs adhesion and proliferation. The authors concluded that the annealing treatment promoted better mechanical properties, a more homogeneous, rougher, and more hydrophilic surface, as well as the formation of a crystalline rutile (TiO_2) layer which elevated the corrosion resistance and biocompatibility of the implant. Similarly, Pazhanivel et al. [77] investigated the post-treatment effect on the corrosion resistance of titanium specimens produced via SLM. Firstly, the authors produced several specimens on an EOS M290 machine using different laser power and scan speed parameters. After performing a tensile test, the researchers reported that the specimen that achieved the best elongation (10.88 %) was manufactured with a laser power of 310 W and a scan speed of 1340 mm/s. Then, the researchers subjected some specimens to a heat treatment at 850 °C for 2 hours and continued for 2 hours more to go through isothermal heating. After that, the furnace temperature was set below 200 °C to reduce the specimen's temperature to 200 °C within 1 hour, and, besides, the samples were also shot-peened. Later, the authors studied the microstructure of the as-built and post-treated Ti-6Al-4V samples and reported that the former exhibited the α' as a major phase, while the latter was composed of ultra-fine grain lamellar α + β phases. Subsequently, corrosive tests were performed in a NaCl and Phosphate Buffer corrosion media, and the researchers concluded that, due to the microstructural change, the post-treated samples demonstrated lower corrosion rates. Likewise, Leon et al. [78] investigated the HIP effect on the corrosion performance of Ti-6Al-4V samples manufactured by EBM. After producing the specimens, the authors conducted a thermal treatment at 925 °C with a pressure of 100 MPa for 3 hours and then performed electrochemical measurements and stress-corrosion examination by means of slow strain-rate testing. After analysing the results, the authors concluded that the heat treatment had a slightly advantageous effect on the mechanochemical performance and corrosion resistance of the titanium alloy due to the reduction of α/β interphase area, the increased amount of β phase, as well as the amplified passivation film stability.

Despite not using any thermal treatment, Sharma et al. [79] investigated the corrosion resistance of as-built Ti-6Al-4V bioimplants manufactured through SLM having in mind that their dissolution inside the human body usually leads to inflammations in the internal organs. The authors used three types of corrosion media (NaOH, NaCl, and H_2SO_4), which varied from alkaline to acidic and also used a physiological simulated body fluid (SBF) medium as a comparison. Then, after manufacturing the samples, the researchers studied the microstructure of the SLMed and commercial cast titanium, used as a reference, and determined that the former exhibited a martensitic microstructure, while the latter showed a uniform distribution of $\alpha + \beta$ phases. Subsequently, the authors conducted several corrosion tests and reported that the SLMed samples had a worse corrosion resistance than the reference because of the α' phase and the higher surface porosity. Nevertheless, the charge transfer resistance, which measures the difficulty faced when an electron is moved from one atom/compound to another, and polarization of both samples were noticeably high in NaOH, NaCl, and SBF, meaning that the samples exhibited a good corrosion resistance in the aforementioned media. However, in a more acidic and aggressive solution (H_2SO_4) they showed an enormously poor corrosion resistance.

Nalli et al. [80] investigated the barrel finishing and heat treatment effect on the mechanical properties of Ti-6Al-4V samples manufactured through SLM. For that, some specimens were heat-treated with distinct temperatures (482 °C, 704 °C, 788 °C, and 800 °C) and holding times (3 h, 4 h, 5 h, 6 h, 8 h, and 10 h). Furthermore, others were barrel finished at 30 and 42 rpm, and as a reference, the authors left some specimens in the as-built state. Then, mechanical tests were performed and, after analysing the results, the researchers reported that as the temperature of the heat treatment and the intensity of the barrel finishing increased, the elongation at break of the specimens improved as well. However, as the elongation increased the YS and UTS decreased, nevertheless, the authors concluded that the heat treatment temperature of 788 °C and barrel finishing speed of 30 rpm provided the best results in terms of ductility versus strength.

In order to have a better understanding of the effects caused by distinct post-treatments on the mechanical properties of Ti-6Al-4V components, the authors of the current work agglomerated distinct information from diverse scientific reports related to YS, UTS, and elongation at break (ε), which can be analysed in Table 3.

Table 3 - Manufacturing process and post-treatment effect on the mechanical properties of the Ti-6Al-4V alloy

Mnf. Process	Condition	Orientation	YS [MPa]	UTS [MPa]	ε [%]	Ref.
Wrought	-	Vertical	836 ± 9	942 ± 8	12.5 ± 1.2	[81]
Wrought	-	Horizontal	832 ± 10	933 ± 7	13.0 ± 1.5	[81]
Forged	Mill Annealed	-	970	1030	16	[82]
Forged	Mill Annealed	-	960 ± 10	1006 ± 10	18.37 ± 0.88	[83]
Cast	-	-	865	980	13.5	[84]
Cast	-	-	750 ± 2	875 ± 10	4.5 ± 0.2	[85]
ASTM F136	-	-	≥ 795	≥ 860	≥ 10	[86]
EBM	As-built	Vertical	812 ± 12	851 ± 19	3.6 ± 0.9	[87]
EBM	As-built	Horizontal	783 ± 15	833 ± 22	2.7 ± 0.4	[87]
EBM	As-built	Vertical	869 ± 7.2	928 ± 9.8	9.9 ± 1.7	[63]

Mnf. Process	Condition	Orientation	YS [MPa]	UTS [MPa]	ε [%]	Ref.
EBM	As-built	Horizontal	899 ± 4.7	978 ± 3.2	9.5 ± 1.2	[63]
EBM	As-built	Vertical	1001 – 1051	1073 – 1116	11 – 15	[82]
EBM	As-built	Horizontal	973 – 1006	1032 – 1066	12 – 15	[82]
EBM	HIPed	-	723 – 817	817 – 918	3 – 9	[88]
EBM	Two-stage HIPed	-	885 ± 6	985 ± 12	-	[92]
EBM	Annealed	-	741 – 842	837 – 918	3 – 9	[88]
EBM	Stress Relieved	-	778 – 943	885 – 1015	3 – 9	[88]
SLM	As-built	Vertical	1150 ± 67	1246 ± 134	1.4 ± 0.5	[81]
SLM	As-built	Horizontal	1273 ± 53	1421 ± 120	3.2 ± 0.5	[81]
SLM	As-built	Vertical	1143 ± 30	1219 ± 20	4.89 ± 0.6	[63]
SLM	As-built	Horizontal	1195 ± 19	1269 ± 9	5.0 ± 0.5	[63]
SLM	HIPed	Vertical	883 – 888	973 – 974	18.5 – 19.4	[89]
SLM	HIPed	-	912 ± 30	1005 ± 30	8.3 ± 2	[90]
SLM	Annealed	Vertical	1045 – 1054	1115 – 1116	9.5 – 12.4	[89]
SLM	Annealed	Vertical	905 – 911	987 – 989	7.4 – 12.5	[89]
SLM	Annealed	Horizontal	913 ± 7	1019 ± 11	8.9 ± 1	[84]
SLM	Annealed	Horizontal	944 ± 8	1036 ± 30	8.5 ± 1	[84]
SLM	Stress Relieved	Vertical	937 ± 9	1052 ± 11	9.6 ± 0.9	[91]

Similarly, several authors [92-100] also studied the heat treatment effect on the mechanical properties and microstructure of Ti-6Al-4V components. For instance, Benzing et al. [92] demonstrated the efficiency of a novel HIP treatment strategy employed to EBMed specimens. The heat treatment consisted in a two-stage HIP, which can be described as follows: 1050 °C with a pressure of 100 MPa for 2 hours with a 12 °C/min heating rate and nearly 1600 °C/min cooling rate done between 1050 °C and 500 °C + temper HIP at 800 °C with a pressure of 30 MPa for 2 hours and 12 °C/min heating and cooling rates. After studying the microstructure and performing mechanical tests, the authors reported that the new heat-treatment maintained the α lath thickness of 1.20 μm ± 0.32 μm, created prior-β grains, sealed the internal porosity, removed microstructural heterogeneities, and maintained the YS and UTS identical to the as-built specimens. In another report, Sabban et al. [96] applied an innovative heat treatment strategy that achieves a bimodal globularized microstructure without the need of a previous plastic deformation process. After manufacturing the specimens in a SLM machine, the researchers employed a heat treatment, Figure 12, with a thermal cycle between 875 °C and 975 °C, a heating rate of 2.5 °C/min, and a cooling rate of 1 °C/min. The authors reported that the numerous heating cycles transformed the lamellar α phase into β phase which later transformed into globular α upon slow cooling. Moreover, the Electron Backscatter Diffraction (EBSD) micrograph showed that the heating cycles also aided to break the α lamella into smaller segments which, subsequently, were converted into spatially separated globular α. Besides, the ductility of the heat-treated specimens, when compared to the as-built ones, was enhanced, the YS and UTS suffered a small decrease, the toughness increased from 98 to 163 MJ/m^3, and beneficial compressive residual stresses were created at the surface level. Likewise, Galarraga et al. [98] submitted EBMed titanium specimens to different solution heat treatments with distinct cooling rates and reported that the water-cooled samples, when compared to the furnace-cooled ones, exhibited an utterly α' martensitic microstructure which promoted an increase of 31 % of the UTS, however, lowered the ductility by 86 %. Haar et al. [100] developed a novel duplex anneal treatment that was firstly done at 910 °C for 8 hours followed by water-quenching and then 750 °C for 4 hours followed by furnace-cooling. The first step of the heat-treatment created a bi-modal microstructure of α in the α' matrix, while the second step promoted the decomposition of α' into α + β lamellar. Subsequently, the authors conducted tensile tests and verified that, when compared to the as-built SLMed and conventionally annealed samples, the duplex annealed ones demonstrated a far greater ductility.

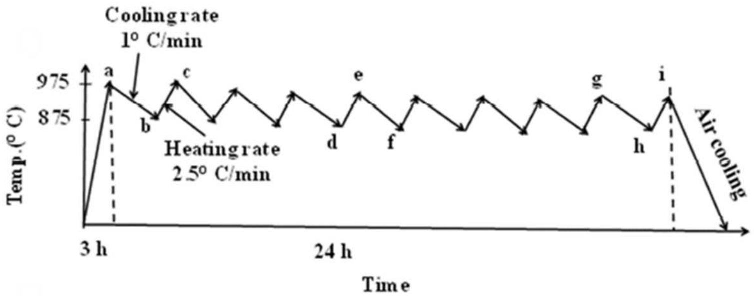

Figure 12 - Schematic of the heat treatment employed for a period of 24 hours. Obtained from [96]

3.2. Residual Stresses

In additive manufacturing, residual stresses are spatially nonuniform and can lead to worse fatigue life and mechanical properties of the built components, as well as layer delamination and part distortion [101]. Moreover, the length of the scan vectors used when producing the components can also influence the distribution and magnitude of RS, as a longer scan vector results in a higher temperature gradient, opposite to shorter scan vectors which are preferable to create lower residual stresses [102]. Hence, one of the most usual scanning strategies employed is the chessboard scanning [103]. Ali et al. [104] investigated the effect of the scan strategy and vector length on SLMed Ti-6Al-4V specimens. For that, the authors used distinct scan strategies, namely 45° alternating, 90° alternating, 2 x 2 mm chessboard, 3 x 3 mm chessboard, 5 x 5 mm chessboard, 5 x 5 mm chessboard with scan vectors rotated 45° in adjacent blocks, and 5 x 5 mm chessboard with scan vectors rotated 90° in adjacent blocks. After analysing the finite element simulation results, the researchers reported that 90° alternating scan strategy caused the lowest residual stresses. Furthermore, the growth of the scan vector length in the chessboard scanning strategy resulted in increased residual stresses. Likewise, Song et al. [105] used finite element simulation and experimental verification to ascertain the effect of scanning strategies on the residual stresses of SLMed Ti-6Al-4V samples. The authors employed three distinct scan strategies which were line scan, 15° alternating scan, and 90° alternating scan. After conducting several tests, they reported that the scan strategy had little to no influence on the molten pool size and the 15° alternating scan strategy produced the lowest residual stresses. Lu et al. [106] investigated the RS evolution on distinct chessboard scanning areas through Vickers micro-indentation. After performing the aforementioned test, the authors reported that the lowest RS were found in the 2 x 2 mm^2 sample, however, that only happened because cracks were formed, and stresses were released. Thus, the authors concluded that the 5 x 5 mm^2 scanning area was the best to produce end parts with the lowest RS.

Laser Shock Peening (LSP) has been widely studied by several authors [107-114] which state that the aforementioned post-treatment refines the microstructure and induces compressive residual stresses on the surface level, thus enhancing the fatigue lifetime of the components made from distinct titanium alloys. Zhang et al. [110] conducted a residual stress analysis through XRD and a micro-hardness test through Vickers indentation and reported that the LSP treatment induced compressive residual stresses and enhanced the micro-hardness of the Ti-6Al-4V samples. Plus, multiple laser shocks had a positive effect on the surface hardening. Furthermore, the authors also ascertained that the number of overlapped laser spots, which were meant to act as the laser peening intensity, provided better fatigue life properties when set to 3. In another study, Ren et al. [111] reported that the LSP treatment was able to reduce the surface roughness and repair surface details of Ti-6Al-4V samples if done with a lower laser pulse energy (6.3 J). Besides, when the authors employed a higher laser pulse energy (7.9 J), the surface hardness significantly increased. Likewise, Jin et al. [113] investigated the influence of LSP on the fatigue behaviour and microstructure of Ti-6Al-4V samples manufactured via EBM. For the post-treatment, the authors used a Nd:YAG laser with a frequency of 1 Hz, a wavelength of 1064 nm, beam diameter of 2.5 mm, and pulse duration of 12 ns. Then, the microstructure was studied, and the researchers reported that the EBMed specimens showed a microstructure composed of α + β phases, Figure 13a. Besides, the LSP treatment caused grain refinement of the α phase via deformation twinning, Figure 13b. Subsequently, the authors performed mechanical tests and concluded that the LSPed samples, when compared to the as-built ones, exhibited a microhardness increase of 11 %, as well as a run-out fatigue strength (2 x 10^6 cycles) increase of 100 MPa. Moreover, the LSP treatment inhibited the crack initiation and enhanced the required work of fatigue fracture, which, according to the literature reviewed by the authors, was due to the formation of compressive residual stresses and the grain refinement. In a similar study, Lan et al. [114] investigated the effect of the LSP treatment on the microstructural evolution and mechanical properties of Ti-6Al-4V specimens. The authors employed the same LSP parameters than Jin et al. [113] and then studied the microstructural evolution of the as-built and post-treated samples. They reported that, when compared to the as-built samples, the post-treated ones exhibited a refined α lamella into sub-micro-equiaxed grains and nano-equiaxed grains. Later, the researchers measured the residual stresses of both types of samples through XRD and concluded that the LSP treatment changed the surface stress state from nearly 45 MPa to -380 MPa. Finally, the authors conducted a tensile test and ascertained that the LSP-treated samples possessed a higher tensile strength and elongation, due to the grain refinement and the induced compressive RS.

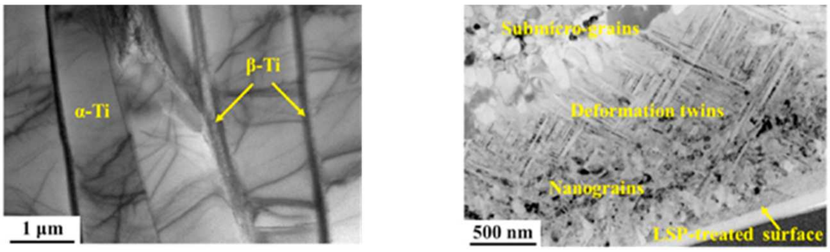

a) b)

Figure 13 - Transmission Electron Microscopy (TEM) image of a) EBM as-built specimens, and b) LSP treated specimens. Adapted from [113]

Eyzat et al. [115] studied the effect of distinct post-treatments on the mechanical properties, residual stresses, and roughness of Ti-6Al-4V samples manufactured via SLM. For that, the researchers employed a stress relief heat treatment at 400 °C for 2 hours to some specimens and the previous heat treatment + Surface Mechanical Attrition Treatment (SMAT) to the others. The latter post-treatment uses a high frequency (20 kHz) ultrasonic generator which leads to the vibration and subsequent impact of spherical balls into the specimen's surface and promotes plastic deformation. After performing mechanical tests, investigating the specimen's surface roughness, and analysing the residual stresses through the XRD method, the authors concluded that SMAT treatment changed the RS from tensile (approx. 100 MPa) to compressive (approx. -300 MPa) as it can be seen in Figure 14, reducing by 80 % the high surface roughness, and boosting the mechanical properties (YS, UTS, and micro-hardness) by 10 % to 15 %. Yakout et al. [116] studied the correlation between residual stresses and process parameters of SLMed Ti-6Al-4V samples. For that, the authors used the Renishaw AM 400 machine and the titanium grade 23 powder from the same enterprise. Then, several specimens were manufactured using distinct laser power (P), scanning speed (v), and hatch spacing (h), while the layer thickness (t) was kept constant at 40 μm. Note that, the aforementioned process parameters are all correlated in the Volumetric Energy Density (Ev) formula, which is:

$$E_v = \frac{P}{v \times h \times t} \tag{1}$$

Later, after conducting distinct studies of the produced samples, the researchers concluded that the Ev increase led to a growth in the part's thermal expansion and density up to a maximum point which was considered the critical energy density (Ev = 86.8 J/mm^3). Furthermore, the components manufactured with a volumetric energy density inferior to the critical one exhibited less residual stresses, as the XRD analysis exposed.

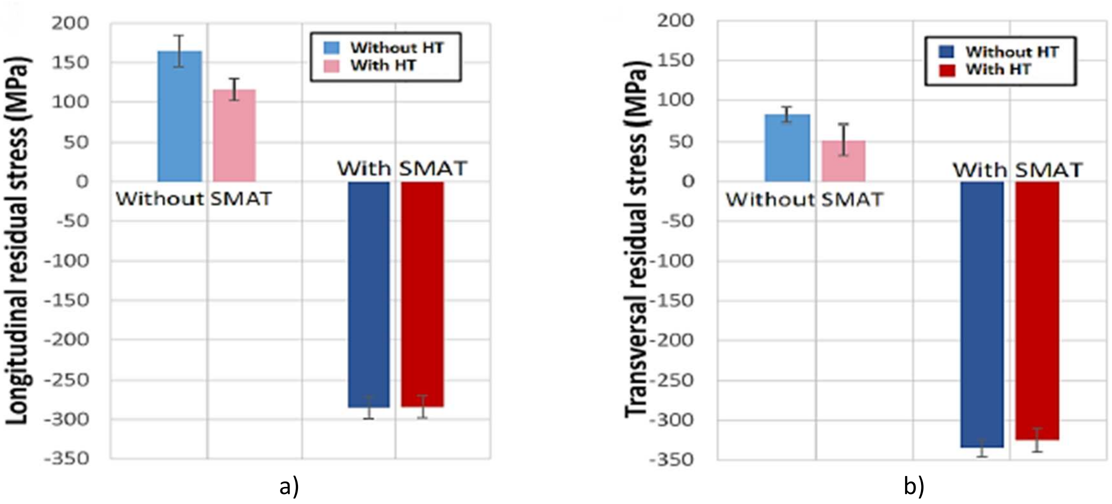

Figure 14 - Post treatments effect on a) longitudinal residual stresses, and b) transversal residual stresses. Adapted from [115]

In a similar study, Vastola et al. [117] investigated, through FEM, the effect of beam scan speed, beam power density, beam size, and chamber bed temperature on the distribution and magnitude of residual stresses on EBMed Ti-6Al-4V samples. The authors reported that lower scan speeds deepened the Heat Affected Zone (HAZ), while higher speeds reduce the HAZ. Furthermore, a 20 % increase of the beam power caused an approximate 15 % growth of the HAZ. Moreover, the researchers also stated that small beam sizes provided higher stresses within a smaller heat-affected zone. Finally, it was concluded that the bed pre-heating temperature was the most crucial parameter for reducing the residual stresses, as a 50 °C increase of the pre-heating temperature promoted an approximate 20 % decrease of residual stresses, Figure 15.

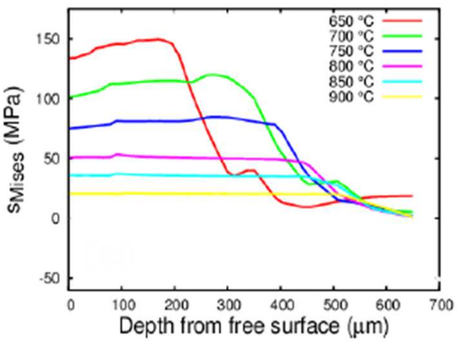

Figure 15 - Quantitative effect of bed pre-heating temperature on residual stresses, where SMises is the Von Mises Stress. Adapted from [117]

In another study, Ning et al. [118] developed an analytical model that predicts RS and part distortion without the need for any iteration-based simulations or FEM. The inputs for the aforementioned model were the laser parameters, scan parameters, and material parameters and the thermal model was calculated by a moving point heat source solution along with a heat sink solution. Then, the thermal stress model was calculated from the thermal model and the RS were computed from the thermal stress model by applying an elastoplastic relaxation method. After that, part distortion was computed using a surface displacement model which, finally, outputted the distortion at distinct locations. The authors validated the accuracy of their analytical model by manufacturing several cantilever-like Ti-6Al-4V specimens on a SLM machine and measuring the part distortion on a Coordinate Measuring Machine (CMM). After comparing the experimental results with the analytical ones, the researchers ascertained that similar agreements were seen in terms of part distortion at distinct locations. Furthermore, the authors also emphasized that the computational time of the analytical model was only 10 seconds on a personal computer, thus allowing a high computational efficiency.

Finally, in Figure 16 and Figure 17 it is possible to analyse two similar diagrams which explain and summarize the expected mechanical properties and microstructures of as-built and heat-treated EBMed and SLMed Ti-6Al-4V components, respectively.

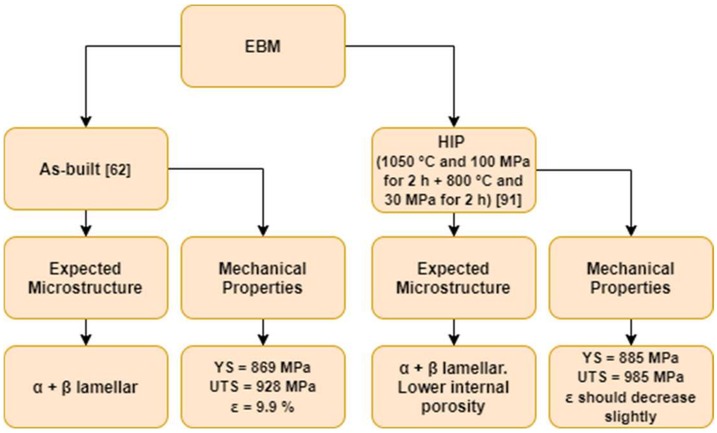

Figure 16 - Diagram of the expected microstructure and mechanical properties of as-built and heat-treated EBMed Ti-6Al-4V samples

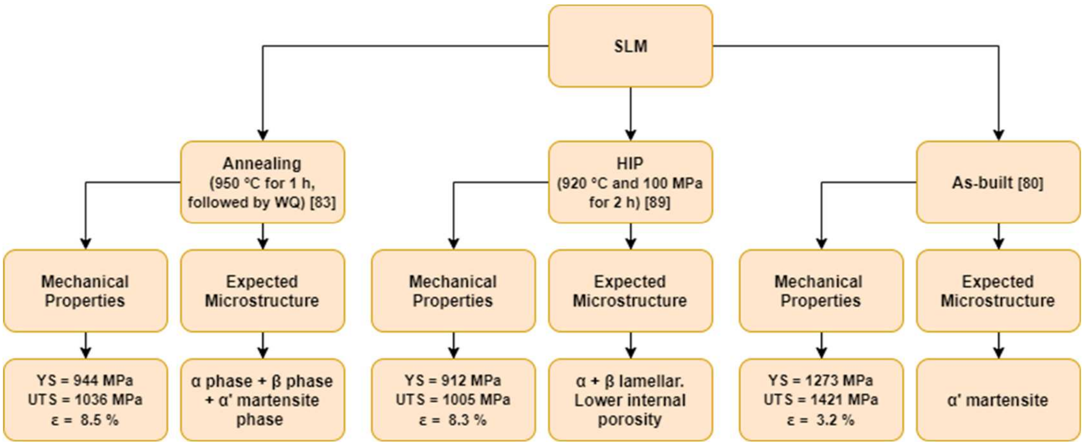

Figure 17 - Diagram of the expected microstructure and mechanical properties of as-built and heat-treated SLMed Ti-6Al-4V samples

4. Concluding Remarks and Outlook

One of the most used and studied superalloys in additive manufacturing is the Ti-6Al-4V, which can be applied in several distinct areas, namely in the aerospace field due to its low density and high melting point (around 1650 °C), and biomedical area owing to its high corrosion resistance and excellent biocompatibility when in contact with tissues or bones of the human body. For this review work, the authors analysed roughly 22 % of the 537 different publications seen in Figure 4, and more than half of those 22 % were about heat treatments and residual stresses of Ti-6Al-4V components produced via SLM and/or EBM in order to provide a solid and unbiased overview. The main ideas can be described as follows:

- Owing to the inherent characteristics of the SLM process, i.e. high cooling rates and quick solidification, the expected microstructure in the as-built state is characterized by fine acicular α′ martensitic precipitates in columnar original β grains, opposed to an α + β lamellar microstructure obtained through EBM. The latter manufacturing process achieves superior building chamber temperatures, therefore reduces the part's cooling rate and forms a bimodal microstructure.
- If one seeks to improve the mechanical properties, such as ductility and hardness, and decrease residual stresses of SLMed Ti-6Al-4V parts, then heat treatments should be conducted. A duplex anneal treatment can be firstly done at 910 °C for 8 hours followed by water-quenching and then 750 °C for 4 hours followed by furnace-cooling. The first step of the heat-treatment creates a bi-modal microstructure of α in the α′ matrix, while the second step promotes the decomposition of α′ into α + β lamellar.
- Hot Isostatic Pressing must be done if one desires to increase the density and fatigue life of the manufactured component, as the aforementioned treatment is responsible for decreasing the size of the internal defects. Besides, one can also predict the expected porosity of the final pieces due to recent developments of trustworthy and efficient computer analytical models. Furthermore, the surface roughness also plays a crucial role in the fatigue life of the final part and is heavily dependent of the manufacturing process, i.e., SLM leads to lower Ra values than EBM, nevertheless, post-machining, sandblasting, and polishing can greatly decrease the Ra values, consequently weaken the crack initiation and improving the fatigue life.
- It has been seen that residual stresses can be lowered through heat treatments as well as optimized printing parameters, such as the bed pre-heating temperature in EBM or the correlation of distinct process parameters in the Volumetric Energy Density formula on SLMed components. Besides, a high scanning speeds coupled with shorter scan vectors, i.e. chessboard scanning, has been demonstrated to lower the residual

stresses. Furthermore, LSP and SMAT post-treatments can also enhance the fatigue life as they induce compressive residual stresses on the surface and increase the microhardness of the components.

Despite the tremendous research over the last years about additively manufactured Ti-6Al-4V parts, there are still some problems to overcome. Namely, the mechanical properties variability when subjected to different heat treatments and process parameters. Furthermore, heat treatments should be further investigated and improved because often one sacrifices yield and ultimate tensile strength for ductility. Also, there is still room to improve regarding residual stresses of Ti-6Al-4V components, i.e. research the RS evolution under different heat treatments and printing parameters.

Lastly, the main limitations felt by the authors upon writing this review paper were the restricted access of several scientific articles as well as the comprehension of a small number of results exhibited by distinct authors. Moreover, as one can analyse in the Pareto's charts (Figure 5 and Figure 6) the scientific community has studied more SLMed Ti-6Al-4V components than EBMed ones, and only a few works focus on residual stresses, which, ultimately, contributed as a big limitation of information.

Author Contributions: Conceptualization: O.T. and F.J.G.S.; methodology: O.T., L.P.F., E.A. and F.J.G.S.; investigation: O.T.; formal analysis: E.A., L.P.F. and F.J.G.S.; Supervision: F.J.G.S. and E.A.; validation: F.J.G.S., L.P.F. and E.A.; writing original draft: O.T.; writing, reviewing and editing: F.J.G.S; resources: E.A.; project administration: F.J.G.S., L.P.F. and E.A.

Funding: This research received no external funding.

Acknowledgements: The main author would like to acknowledge his mentor for all the help and support given through the writing of this report.

Conflicts of Interest: The authors declare no conflict of interest.

List of Symbols and Abbreviations:

3DP	Three-dimensional Printing
AM	Additive Manufacturing
ASTM	American Society for Testing and Materials
CMM	Coordinate Measuring Machine
EBM	Electron Beam Melting
EBSD	Electron Backscatter Diffraction
Ev	Volumetric Energy Density
FC	Furnace Cooling
FEM	Finite Element Modelling
h	Hatch Spacing
H_2SO_4	Sulfuric Acid
HAZ	Heat Affected Zone
hBMSCs	Human Bone Mesenchymal Stem Cells
HIP	Hot Isostatic Pressing
ISO	International Organization for Standardization
LSP	Laser Shock Peening
Ms	Martensite Start Temperature

NaCl	Sodium Chloride
NaOH	Sodium Hydroxide
P	Laser Power
Ra	Surface Roughness
Ref.	Reference
RS	Residual Stresses
SBF	Simulated Body Fluid
SLM	Selective Laser Melting
SLS	Selective Laser Sintering
SMAT	Surface Mechanical Attrition Treatment
t	Layer Thickness
$T_{ambient}$	Ambient Temperature
T_{melt}	Melting Temperature
UTS	Ultimate Tensile Strength
v	Scanning Speed
WQ	Water Quenching
XRD	X-Ray Diffraction
YS	Yield Strength
ε	Elongation at Break

References

1. Goldberg, D. (2018). History of 3D Printing: It’s Older Than You Are (That Is, If You’re Under 30), AutoDesk. [Online], available on: https://www.autodesk.com/redshift/history-of-3d-printing/ [Accessed on 04/12/2019].
2. ISO/ASTM 52900-15, Standard Terminology for Additive Manufacturing – General Principles – Terminology, ASTM International, West Conshohocken, PA, 2015.
3. Silva, F. J. G., Campilho, R. D. S. G., Gouveia, R. M., Pinto, G., & Baptista, A. (2018). A Novel Approach to Optimize the Design of Parts for Additive Manufacturing. *Procedia Manufacturing*, *17*, 53–61. https://doi.org/10.1016/j.promfg.2018.10.012.
4. Gouveia, R. M., Silva, F. J. G., Atzeni, E., Sormaz, D., Alves, J. L., & Pereira, A. B. (2020). Effect of Scan Strategies and Use of Support Structures on Surface Quality and Hardness of L-PBF AlSi10Mg Parts, *Materials, 13*(10), 2248 (20 pp.). https://doi.org/10.3390/ma13102248.
5. ASTM F2792-12a, “Standard Terminology for Additive Manufacturing Technologies”, (Withdrawn 2015) ASTM International, pp. 1–3, West Conshohocken, PA, 2012.
6. W. Meiners. *Shaped body especially prototype or replacement part production*, German patent 19649865 filled on December 2nd of 1996, issued on February 12th of 1998.
7. Giganto, S., Zapico, P., Castro-Sastre, M. Á., Martínez-Pellitero, S., Leo, P., & Perulli, P. (2019). Influence of the scanning strategy parameters upon the quality of the SLM parts. *Procedia Manufacturing*, *41*, 698–705. https://doi.org/10.1016/j.promfg.2019.09.060.
8. Anwar, A. B., Ibrahim, I. H., & Pham, Q. C. (2019). Spatter transport by inert gas flow in selective laser melting: A simulation study. *Powder Technology*, *352*, 103–116, https://doi.org/10.1016/j.powtec.2019.04.044.

9. Ferrar, B., Mullen, L., Jones, E., Stamp, R., & Sutcliffe, C. J. (2012). Gas flow effects on selective laser melting (SLM) manufacturing performance. *Journal of Materials Processing Technology*, *212*(2), 355–364. https://doi.org/10.1016/j.jmatprotec.2011.09.020.
10. Konečná, R., Nicoletto, G., & Riva, E. (2019). Notch fatigue behavior of Inconel 718 produced by selective laser melting. *Procedia Structural Integrity*, *17*, 138–145, https://doi.org/10.1016/j.prostr.2019.08.019.
11. Contuzzi, N., Campanelli, S. L., & Ludovico, A. D. (2011). 3D finite element analysis in the Selective Laser Melting process. *International Journal of Simulation Modelling*, *10*(3), 113–121. https://doi.org/10.2507/IJSIMM10(3)1.169.
12. Nguyen, Q. B., Luu, D. N., Nai, S. M. L., Zhu, Z., Chen, Z., & Wei, J. (2018). The role of powder layer thickness on the quality of SLM printed parts. *Archives of Civil and Mechanical Engineering*, *18*(3), 948–955. https://doi.org/10.1016/j.acme.2018.01.015.
13. Arcam AB. *Arrangement for the production of a three-dimensional product*, United States patent 20060141089 filled on December 10th of 2003, issued on June 29th of 2006.
14. Körner, C., Attar, E., & Heinl, P. (2011). Mesoscopic simulation of selective beam melting processes. *Journal of Materials Processing Technology*, *211*(6), 978–987. https://doi.org/10.1016/j.jmatprotec.2010.12.016.
15. Galati, M., & Iuliano, L. (2018, January 1). A literature review of powder-based electron beam melting focusing on numerical simulations. *Additive Manufacturing*. https://doi.org/10.1016/j.addma.2017.11.001.
16. Li, P., Warner, D. H., Fatemi, A., & Phan, N. (2016). Critical assessment of the fatigue performance of additively manufactured Ti-6Al-4V and perspective for future research. *International Journal of Fatigue*, *85*, 130–143. https://doi.org/10.1016/j.ijfatigue.2015.12.003.
17. Prabhakar, P., Sames, W. J., Dehoff, R., & Babu, S. S. (2015). Computational modeling of residual stress formation during the electron beam melting process for Inconel 718. *Additive Manufacturing*, *7*, 83–91. https://doi.org/10.1016/j.addma.2015.03.003.
18. Smith, C. J., Derguti, F., Hernandez Nava, E., Thomas, M., Tammas-Williams, S., Gulizia, S., Fraser, D., & Todd, I. (2016). Dimensional accuracy of Electron Beam Melting (EBM) additive manufacture with regard to weight optimized truss structures. *Journal of Materials Processing Technology*, *229*, 128–138. https://doi.org/10.1016/j.jmatprotec.2015.08.028.
19. Gokuldoss, P. K., Kolla, S., & Eckert, J. (2017). Additive manufacturing processes: Selective laser melting, electron beam melting and binder jetting-selection guidelines. *Materials, 10*(6), 672 (12 pp.). https://doi.org/10.3390/ma10060672.
20. Azam, F. I., Abdul Rani, A. M., Altaf, K., Rao, T. V. V. L. N., & Zaharin, H. A. (2018). An In-Depth Review on Direct Additive Manufacturing of Metals. *IOP Conference Series: Materials Science and Engineering*, *328*(1), (8 pp.). https://doi.org/10.1088/1757-899X/328/1/012005.
21. Unknown author. *Properties of Titanium Ti-6Al-4V (Grade 5)*, Matweb. [Online], available on: http://www.matweb.com/search/datasheet.aspx?MatGUID=10d463eb3d3d4ff48fc57e0ad1037434 [Accessed on 06/12/2019].
22. Zuback, J. S., & DebRoy, T. (2018). The hardness of additively manufactured alloys. *Materials*, *11*(11), 2070 (41 pp.). https://doi.org/10.3390/ma11112070.
23. Dai, N., Zhang, L. C., Zhang, J., Zhang, X., Ni, Q., Chen, Y., Wu, M., & Yang, C. (2016). Distinction in corrosion resistance of selective laser melted Ti-6Al-4V alloy on different planes. *Corrosion Science*, *111*, 703–710. https://doi.org/10.1016/j.corsci.2016.06.009.
24. Lin, J., Lv, Y., Liu, Y., Sun, Z., Wang, K., Li, Z., Wu, Y., & Xu, B. (2017). Microstructural evolution and mechanical property of Ti-6Al-4V wall deposited by continuous plasma arc additive manufacturing without post heat treatment. *Journal of the Mechanical Behavior of Biomedical Materials*, *69*, 19–29. https://doi.org/10.1016/j.jmbbm.2016.12.015.
25. Tamilselvi, S., Raman, V., & Rajendran, N. (2006). Corrosion behaviour of Ti–6Al–7Nb and Ti–6Al–4V ELI alloys in the simulated body fluid solution by electrochemical impedance spectroscopy. *Electrochimica Acta, 52*(3), 839–846. https://doi.org/10.1016/j.electacta.2006.06.018.

26. Castellanos, S. D., Alves, J. L., & Neto, R. J. (2017). A comparative study of manufacturing processes of complex surface parts in Titanium Ti6Al4V. *Ciência e Tecnologia Dos Materiais*, *29* (2), 73–78. https://doi.org/10.1016/j.ctmat.2017.03.002.
27. Lütjering, G., Williams, J. C. (2007). Titanium, second edition. Springer, New York. https://doi.org/10.1007/978-3-540-73036-1.
28. Huang, R., Riddle, M., Graziano, D., Warren, J., Das, S., Nimbalkar, S., Cresko, J., & Masanet, E. (2016). Energy and emissions saving potential of additive manufacturing: the case of lightweight aircraft components. *Journal of Cleaner Production*, *135*, 1559–1570. https://doi.org/10.1016/j.jclepro.2015.04.109.~
29. Ngo, T. D., Kashani, A., Imbalzano, G., Nguyen, K. T. Q., & Hui, D. (2018). Additive manufacturing (3D printing): A review of materials, methods, applications and challenges. *Composites Part B: Engineering*, *143*, 172-196. https://doi.org/10.1016/j.compositesb.2018.02.012.
30. Ducato, A., Fratini, L., La Cascia, M., & Mazzola, G. (2013). An automated visual inspection system for the classification of the phases of Ti-6Al-4V titanium alloy. *Lecture Notes in Computer*, *8048*, 362–369. https://doi.org/10.1007/978-3-642-40246-3_45.
31. Ahmed, T., & Rack, H. J. (1998). Phase transformations during cooling in α+β titanium alloys. *Materials Science and Engineering: A*, *243*(1-2), 206–211. https://doi.org/10.1016/s0921-5093(97)00802-2.
32. Boyer, R., Collings, E. W., & Welsch, G. (1994). Materials Properties Handbook: Titanium Alloys. , ASM International.
33. Gil Mur, F. X., Rodríguez, D., & Planell, J. A. (1996). Influence of tempering temperature and time on the α′-Ti-6Al-4V martensite. *Journal of Alloys and Compounds*, *234*(2), 287–289. https://doi.org/10.1016/0925-8388(95)02057-8.
34. Reisgen, U., Olschok, S., Sharma, R., & Gach, S. (2017). Influence on martensite-start-temperature and volume expansion of low-transformation-temperature materials used for residual stress relief in beam welding. *Materials Science & Engineering Technology*, *48*(12), 1276–1282. https://doi.org/10.1002/mawe.201700159.
35. Liu, S., & Shin, Y. C. (2019). Additive manufacturing of Ti6Al4V alloy: A review. *Materials and Design*, *164*., 107552 (23 pp.). https://doi.org/10.1016/j.matdes.2018.107552.
36. Bartlett, J. L., & Li, X. (2019). An overview of residual stresses in metal powder bed fusion. *Additive Manufacturing*, *27*, 131-149. https://doi.org/10.1016/j.addma.2019.02.020.
37. Vayssette, B., Saintier, N., Brugger, C., Elmay, M., & Pessard, E. (2018). Surface roughness of Ti-6Al-4V parts obtained by SLM and EBM: Effect on the High Cycle Fatigue life. *Procedia Engineering*, *213*, 89–97. https://doi.org/10.1016/j.proeng.2018.02.010.
38. Liu, D., & Flewitt, P. E. J. (2014). Raman measurements of stress in films and coatings. *Spectroscopic Properties of Inorganic and Organometallic Compounds*, *45*, 141–177. https://doi.org/10.1039/9781782621485-00141.
39. Guo, J., Fu, H., Pan, B., & Kang, R. (2020). Recent progress of residual stress measurement methods: A review. *Chinese Journal of Aeronautics*. In press, https://doi.org/10.1016/j.cja.2019.10.010.
40. Barros, R., Silva, F. J. G., Gouveia, R. M., Saboori, A., Marchese, G., Biamino, S., Salmi, A., & Atzeni, E. (2019). Laser Powder Bed Fusion of Inconel 718: Residual Stress Analysis Before and After Heat Treatment. *Metals*, *9*(12), 1290 (17 pp.). https://doi.org/10.3390/met9121290.
41. ASTM E 837-08. (2008). Standard Test Method for Determining Residual Stresses by the Hole-Drilling Strain-Gages, *1*, 1–17.
42. Thijs, L., Verhaeghe, F., Craeghs, T., Humbeeck, J. V., & Kruth, J. P. (2010). A study of the microstructural evolution during selective laser melting of Ti-6Al-4V. *Acta Materialia*, *58*(9), 3303–3312. https://doi.org/10.1016/j.actamat.2010.02.004.
43. Facchini, L., Magalini, E., Robotti, P., Molinari, A., Höges, S., & Wissenbach, K. (2010). Ductility of a Ti-6Al-4V alloy produced by selective laser melting of prealloyed powders. *Rapid Prototyping Journal*, *16*(6), 450–459. https://doi.org/10.1108/13552541011083371.

44. Gong, H., Rafi, K., Gu, H., Janaki Ram, G. D., Starr, T., & Stucker, B. (2015). Influence of defects on mechanical properties of Ti-6Al-4V components produced by selective laser melting and electron beam melting. *Materials and Design*, *86*, 545–554. https://doi.org/10.1016/j.matdes.2015.07.147.
45. Benedetti, M., Torresani, E., Leoni, M., Fontanari, V., Bandini, M., Pederzolli, C., & Potrich, C. (2017). The effect of post-sintering treatments on the fatigue and biological behavior of Ti-6Al-4V ELI parts made by selective laser melting. *Journal of the Mechanical Behavior of Biomedical Materials*, *71*, 295–306. https://doi.org/10.1016/j.jmbbm.2017.03.024.
46. Xu, W., Sun, S., Elambasseril, J., Liu, Q., Brandt, M., & Qian, M. (2015). Ti-6Al-4V Additively Manufactured by Selective Laser Melting with Superior Mechanical Properties. *JOM*, *67*(3), 668–673. https://doi.org/10.1007/s11837-015-1297-8.
47. Xu, J., Zhu, J., Fan, J., Zhou, Q., Peng, Y., & Guo, S. (2019). Microstructure and mechanical properties of Ti–6Al–4V alloy fabricated using electron beam freeform fabrication. *Vacuum*, *167*, 364–373. https://doi.org/10.1016/j.vacuum.2019.06.030.
48. Galarraga, H., Lados, D. A., Dehoff, R. R., Kirka, M. M., & Nandwana, P. (2016). Effects of the microstructure and porosity on properties of Ti-6Al-4V ELI alloy fabricated by electron beam melting (EBM). *Additive Manufacturing*, *10*, 47–57. https://doi.org/10.1016/j.addma.2016.02.003.
49. Zhao, X., Li, S., Zhang, M., Liu, Y., Sercombe, T. B., Wang, S., Hao, Y., Yang, R., & Murr, L. E. (2016). Comparison of the microstructures and mechanical properties of Ti-6Al-4V fabricated by selective laser melting and electron beam melting. *Materials and Design*, *95*, 21–31. https://doi.org/10.1016/j.matdes.2015.12.135.
50. Chern, A. H., Nandwana, P., McDaniels, R., Dehoff, R. R., Liaw, P. K., Tryon, R., & Duty, C. E. (2020). Build orientation, surface roughness, and scan path influence on the microstructure, mechanical properties, and flexural fatigue behavior of Ti–6Al–4V fabricated by electron beam melting. *Materials Science and Engineering A*, *772*, 138740 (45 pp.). https://doi.org/10.1016/j.msea.2019.138740.
51. Murr, L. E., Esquivel, E. V., Quinones, S. A., Gaytan, S. M., Lopez, M. I., Martinez, E. Y., Medina, F., Hernandez, D. H., Martinez, E., Martinez, J. L., Stafford, S. W., Brown, D. K., Hoppe, T., Meyers, W., Lindhe, U., & Wicker, R. B. (2009). Microstructures and mechanical properties of electron beam-rapid manufactured Ti-6Al-4V biomedical prototypes compared to wrought Ti-6Al-4V. *Materials Characterization*, *60*(2), 96–105. https://doi.org/10.1016/j.matchar.2008.07.006.
52. Edwards, P., & Ramulu, M. (2014). Fatigue performance evaluation of selective laser melted Ti-6Al-4V. *Materials Science and Engineering A*, *598*, 327–337. https://doi.org/10.1016/j.msea.2014.01.041.
53. Chan, K. S., Koike, M., Mason, R. L., & Okabe, T. (2013). Fatigue life of titanium alloys fabricated by additive layer manufacturing techniques for dental implants. *Metallurgical and Materials Transactions A: Physical Metallurgy and Materials Science*, *44*(2), 1010–1022. https://doi.org/10.1007/s11661-012-1470-4.
54. Fousová, M., Vojtěch, D., Doubrava, K., Daniel, M., & Lin, C. F. (2018). Influence of inherent surface and internal defects on mechanical properties of additively manufactured Ti6Al4V alloy: Comparison between selective laser melting and electron beam melting. *Materials*, *11*(4), 537 (18 pp.). https://doi.org/10.3390/ma11040537.
55. Qiu, C., Panwisawas, C., Ward, M., Basoalto, H. C., Brooks, J. W., & Attallah, M. M. (2015). On the role of melt flow into the surface structure and porosity development during selective laser melting. *Acta Materialia*, *96*, 72–79. https://doi.org/10.1016/j.actamat.2015.06.004.
56. Stef, J., Poulon-Quintin, A., Redjaimia, A., Ghanbaja, J., Ferry, O., De Sousa, M., & Gouné, M. (2018). Mechanism of porosity formation and influence on mechanical properties in selective laser melting of Ti-6Al-4V parts. *Materials and Design*, *156*, 480–493. https://doi.org/10.1016/j.matdes.2018.06.049.
57. Tammas-Williams, S., Zhao, H., Léonard, F., Derguti, F., Todd, I., & Prangnell, P. B. (2015). XCT analysis of the influence of melt strategies on defect population in Ti-6Al-4V components manufactured by Selective Electron Beam Melting. *Materials Characterization*, *102*, 47–61. https://doi.org/10.1016/j.matchar.2015.02.008.

58. Ning, J., Sievers, D. E., Garmestani, H., & Liang, S. Y. (2020). Analytical modeling of part porosity in metal additive manufacturing. *International Journal of Mechanical Sciences*, *172*, 105428 (20 pp.). https://doi.org/10.1016/j.ijmecsci.2020.105428.
59. Zhang, W., Qin, P., Wang, Z., Yang, C., Kollo, L., Grzesiak, D., & Prashanth, K. G. (2019). Superior wear resistance in EBM-Processed TC4 alloy compared with SLM and forged samples. *Materials*, *12*(5), 782 (11 pp.). https://doi.org/10.3390/ma12050782.
60. Mohammadhosseini, A., Fraser, D., Masood, S. H., & Jahedi, M. (2013). Microstructure and mechanical properties of Ti–6Al–4V manufactured by electron beam melting process. *Materials Research Innovations*, *17*, 106–112. https://doi.org/10.1179/1432891713z.000000000302.
61. Tan, X., Kok, Y., Tan, Y. J., Descoins, M., Mangelinck, D., Tor, S. B., Leong, K. F., & Chua, C. K. (2015). Graded microstructure and mechanical properties of additive manufactured Ti-6Al-4V via electron beam melting. *Acta Materialia*, *97*, 1–16. https://doi.org/10.1016/j.actamat.2015.06.036.
62. Losertová, M., & Kubeš, V. (2017). Microstructure and mechanical properties of selective laser melted Ti6Al4V alloy. *IOP Conference Series: Materials Science and Engineering*, *266*, 012009 (6 pp.). https://doi.org/10.1088/1757-899x/266/1/012009.
63. Rafi, H. K., Karthik, N. V., Gong, H., Starr, T. L., & Stucker, B. E. (2013). Microstructures and mechanical properties of Ti6Al4V parts fabricated by selective laser melting and electron beam melting. *Journal of Materials Engineering and Performance*, *22*(12), 3872–3883. https://doi.org/10.1007/s11665-013-0658-0.
64. Balyakin, A., Zhuchenko, E., & Nosova, E. (2019). Study of heat treatment impact on the surface defects appearance on samples obtained by selective laser melting of Ti-6Al-4V during chemical polishing. *Materials Today: Proceedings*, *19*, pp. 2307–2311. https://doi.org/10.1016/j.matpr.2019.07.676.
65. Vayssette, B., Saintier, N., Brugger, C., & El May, M. (2020). Surface roughness effect of SLM and EBM Ti-6Al-4V on multiaxial high cycle fatigue. *Theoretical and Applied Fracture Mechanics*, *108*, 102581 (35 pp.). https://doi.org/10.1016/j.tafmec.2020.102581.
66. Yuan, W., Hou, W., Li, S., Hao, Y., Yang, R., Zhang, L. C., & Zhu, Y. (2018). Heat treatment enhancing the compressive fatigue properties of open-cellular Ti-6Al-4V alloy prototypes fabricated by electron beam melting. *Journal of Materials Science and Technology*, *34*(7), 1127–1131. https://doi.org/10.1016/j.jmst.2017.12.003.
67. Zhao, S., Li, S. J., Hou, W. T., Hao, Y. L., Yang, R., & Misra, R. D. K. (2016). The influence of cell morphology on the compressive fatigue behavior of Ti-6Al-4V meshes fabricated by electron beam melting. *Journal of the Mechanical Behavior of Biomedical Materials*, *59*, 251–264. https://doi.org/10.1016/j.jmbbm.2016.01.034.
68. Chastand, V., Quaegebeur, P., Maia, W., & Charkaluk, E. (2018). Comparative study of fatigue properties of Ti-6Al-4V specimens built by electron beam melting (EBM) and selective laser melting (SLM). *Materials Characterization*, *143*, 76–81. https://doi.org/10.1016/j.matchar.2018.03.028.
69. Pegues, J. W., Shao, S., Shamsaei, N., Sanaei, N., Fatemi, A., Warner, D. H., Li, P., & Phan, N. (2020). Fatigue of additive manufactured Ti-6Al-4V, Part I: The effects of powder feedstock, manufacturing, and post-process conditions on the resulting microstructure and defects. *International Journal of Fatigue*, *132*, 105358 (74 pp.). https://doi.org/10.1016/j.ijfatigue.2019.105358.
70. Molaei, R., Fatemi, A., Sanaei, N., Pegues, J., Shamsaei, N., Shao, S., Li, P., Warner, D. H., & Phan, N. (2020). Fatigue of additive manufactured Ti-6Al-4V, Part II: The relationship between microstructure, material cyclic properties, and component performance. *International Journal of Fatigue*, *132*, 105363 (82 pp.). https://doi.org/10.1016/j.ijfatigue.2019.105363.
71. Wu, M.-W., Chen, J.-K., Lin, B.-H., Chiang, P.-H., & Tsai, M.-K. (2020). Compressive fatigue properties of additive-manufactured Ti-6Al-4V cellular material with different porosities. *Materials Science and Engineering: A*, 139695. In press, https://doi.org/10.1016/j.msea.2020.139695.
72. Viespoli, L. M., Bressan, S., Itoh, T., Hiyoshi, N., Prashanth, K. G., & Berto, F. (2020). Creep and high temperature fatigue performance of as build selective laser melted Ti-based 6Al-4V titanium

alloy. *Engineering Failure Analysis*, *111*, 104477 (7 pp.). https://doi.org/10.1016/j.engfailanal.2020.104477.

73. Yu, H., Li, F., Wang, Z., & Zeng, X. (2019). Fatigue performances of selective laser melted Ti-6Al-4V alloy: Influence of surface finishing, hot isostatic pressing and heat treatments. *International Journal of Fatigue*, *120*, 175–183. https://doi.org/10.1016/j.ijfatigue.2018.11.019.
74. Kim, Y. K., Park, S. H., Yu, J. H., AlMangour, B., & Lee, K. A. (2018). Improvement in the high-temperature creep properties via heat treatment of Ti-6Al-4V alloy manufactured by selective laser melting. *Materials Science and Engineering A*, *715*, 33–40. https://doi.org/10.1016/j.msea.2017.12.085.
75. Hemmasian Ettefagh, A., Zeng, C., Guo, S., & Raush, J. (2019). Corrosion behavior of additively manufactured Ti-6Al-4V parts and the effect of post annealing. *Additive Manufacturing*, *28*, 252–258. https://doi.org/10.1016/j.addma.2019.05.011.
76. Wang, M., Wu, Y., Lu, S., Chen, T., Zhao, Y., Chen, H., & Tang, Z. (2016). Fabrication and characterization of selective laser melting printed Ti–6Al–4V alloys subjected to heat treatment for customized implants design. *Progress in Natural Science: Materials International*, *26*(6), 671–677. https://doi.org/10.1016/j.pnsc.2016.12.006.
77. Pazhanivel, B., Sathiya, P., & Sozhan, G. (2020). Ultra-fine bimodal ($\alpha + \beta$) microstructure induced mechanical strength and corrosion resistance of Ti-6Al-4V alloy produced via laser powder bed fusion process. *Optics and Laser Technology*, *125*, 106017 (9 pp.). https://doi.org/10.1016/j.optlastec.2019.106017.
78. Leon, A., Levy, G. K., Ron, T., Shirizly, A., & Aghion, E. (2020). The effect of hot isostatic pressure on the corrosion performance of Ti-6Al-4 V produced by an electron-beam melting additive manufacturing process. *Additive Manufacturing*, *33*, 101039 (30 pp.). https://doi.org/10.1016/j.addma.2020.101039.
79. Sharma, A., Oh, M. C., Kim, J. T., Srivastava, A. K., & Ahn, B. (2020). Investigation of electrochemical corrosion behavior of additive manufactured Ti–6Al–4V alloy for medical implants in different electrolytes. *Journal of Alloys and Compounds*, *830*, 154620 (38 pp.). https://doi.org/10.1016/j.jallcom.2020.154620.
80. Nalli, F., Bottini, L., Boschetto, A., Cortese, L., & Veniali, F. (2020). Effect of industrial heat treatment and barrel finishing on the mechanical performance of Ti6AL4V processed by selective laser melting. *Applied Sciences*, *10*(7), 2280 (16 pp.). https://doi.org/10.3390/app10072280.
81. Wysocki, B., Maj, P., Sitek, R., Buhagiar, J., Kurzydłowski, K. J., & Świeszkowski, W. (2017). Laser and electron beam additive manufacturing methods of fabricating titanium bone implants. *Applied Sciences*, *7*(7), 657 (20 pp.). https://doi.org/10.3390/app7070657.
82. Zhai, Y., Galarraga, H., & Lados, D. A. (2016). Microstructure, static properties, and fatigue crack growth mechanisms in Ti-6Al-4V fabricated by additive manufacturing: LENS and EBM. *Engineering Failure Analysis*, *69*, 3–14. https://doi.org/10.1016/j.engfailanal.2016.05.036.
83. Vrancken, B., Thijs, L., Kruth, J. P., & Van Humbeeck, J. (2012). Heat treatment of Ti6Al4V produced by Selective Laser Melting: Microstructure and mechanical properties. *Journal of Alloys and Compounds*, *541*, 177–185. https://doi.org/10.1016/j.jallcom.2012.07.022.
84. Vilaro, T., Colin, C., & Bartout, J. D. (2011). As-fabricated and heat-treated microstructures of the Ti-6Al-4V alloy processed by selective laser melting. *Metallurgical and Materials Transactions A: Physical Metallurgy and Materials Science*, *42*(10), 3190–3199. https://doi.org/10.1007/s11661-011-0731-y.
85. Koike, M., Greer, P., Owen, K., Lilly, G., Murr, L. E., Gaytan, S. M., Martinez, E., & Okabe, T. (2011). Evaluation of titanium alloys fabricated using rapid prototyping technologies-electron beam melting and laser beam melting. *Materials*, *4*(10), 1776–1792. https://doi.org/10.3390/ma4101776.
86. ASTM F136-08, Standard Specification for Wrought Titanium-6Aluminum-4Vanadium ELI (Extra Low Interstitial) Alloy for Surgical Implant Applications (UNS R56401), ASTM International, West Conshohocken, PA, 2008, www.astm.org.

87. Edwards, P., O'Conner, A., & Ramulu, M. (2013). Electron Beam Additive Manufacturing of Titanium Components: Properties and Performance. *Journal of Manufacturing Science and Engineering*, *135*(6), 061016 (8 pp.). https://doi.org/doi:10.1115/1.4025773.
88. Hayes, B. J., Martin, B. W., Welk, B., Kuhr, S. J., Ales, T. K., Brice, D. A., Ghamarian, I., Baker, A. H., Haden, C. V., Harlow, D. G., Fraser, H. L., & Collins, P. C. (2017). Predicting tensile properties of Ti-6Al-4V produced via directed energy deposition. *Acta Materialia*, *133*, 120–133. https://doi.org/10.1016/j.actamat.2017.05.025.
89. Kasperovich, G., & Hausmann, J. (2015). Improvement of fatigue resistance and ductility of TiAl6V4 processed by selective laser melting. *Journal of Materials Processing Technology*, *220*, 202–214. https://doi.org/10.1016/j.jmatprotec.2015.01.025.
90. Leuders, S., Thöne, M., Riemer, A., Niendorf, T., Tröster, T., Richard, H. A., & Maier, H. J. (2013). On the mechanical behaviour of titanium alloy TiAl6V4 manufactured by selective laser melting: Fatigue resistance and crack growth performance. *International Journal of Fatigue*, *48*, 300–307. https://doi.org/10.1016/j.ijfatigue.2012.11.011.
91. Simonelli, M., Tse, Y. Y., & Tuck, C. (2014). Effect of the build orientation on the mechanical properties and fracture modes of SLM Ti-6Al-4V. *Materials Science and Engineering A*, *616*, 1–11. https://doi.org/10.1016/j.msea.2014.07.086.
92. Benzing, J., Hrabe, N., Quinn, T., White, R., Rentz, R., & Ahlfors, M. (2019). Hot isostatic pressing (HIP) to achieve isotropic microstructure and retain as-built strength in an additive manufacturing titanium alloy (Ti-6Al-4V). *Materials Letters*, *257*, 126690 (5 pp.). https://doi.org/10.1016/j.matlet.2019.126690.
93. Galati, M., Saboori, A., Biamino, S., Calignano, F., Lombardi, M., Marchiandi, G., Minetola, P., Fino, P., & Iuliano, L. (2020). Ti-6Al-4V lattice structures produced by EBM: Heat treatment and mechanical properties. *Procedia CIRP*, *88*, 411–416. https://doi.org/10.1016/j.procir.2020.05.071.
94. Morita, T., Tsuda, C., & Nakano, T. (2017). Influences of scanning speed and short-time heat treatment on fundamental properties of Ti-6Al-4V alloy produced by EBM method. *Materials Science and Engineering A*, *704*, 246–251. https://doi.org/10.1016/j.msea.2017.08.020.
95. Zhang, X. Y., Fang, G., Leeflang, S., Böttger, A. J., A. Zadpoor, A., & Zhou, J. (2018). Effect of subtransus heat treatment on the microstructure and mechanical properties of additively manufactured Ti-6Al-4V alloy. *Journal of Alloys and Compounds*, *735*, 1562–1575. https://doi.org/10.1016/j.jallcom.2017.11.263.
96. Sabban, R., Bahl, S., Chatterjee, K., & Suwas, S. (2019). Globularization using heat treatment in additively manufactured Ti-6Al-4V for high strength and toughness. *Acta Materialia*, *162*, 239–254. https://doi.org/10.1016/j.actamat.2018.09.064.
97. Tsai, M. T., Chen, Y. W., Chao, C. Y., Jang, J. S. C., Tsai, C. C., Su, Y. L., & Kuo, C. N. (2020). Heat-treatment effects on mechanical properties and microstructure evolution of Ti-6Al-4V alloy fabricated by laser powder bed fusion. *Journal of Alloys and Compounds*, *816*, 152615 (11 pp.). https://doi.org/10.1016/j.jallcom.2019.152615.
98. Galarraga, H., Warren, R. J., Lados, D. A., Dehoff, R. R., Kirka, M. M., & Nandwana, P. (2017). Effects of heat treatments on microstructure and properties of Ti-6Al-4V ELI alloy fabricated by electron beam melting (EBM). *Materials Science and Engineering A*, *685*, 417–428. https://doi.org/10.1016/j.msea.2017.01.019.
99. Zhang, D., Wang, L., Zhang, H., Maldar, A., Zhu, G., Chen, W., Park, J. S., Wang, J., & Zeng, X. (2020). Effect of heat treatment on the tensile behavior of selective laser melted Ti-6Al-4V by in situ X-ray characterization. *Acta Materialia*, *189*, 93–104. https://doi.org/10.1016/j.actamat.2020.03.003.
100. Ter Haar, G. M., & Becker, T. H. (2018). Selective laser melting produced Ti-6Al-4V: Post-process heat treatments to achieve superior tensile properties. *Materials*, *11*(1), 146 (15 pp.). https://doi.org/10.3390/ma11010146.
101. Mercelis, P., & Kruth, J. P. (2006). Residual stresses in selective laser sintering and selective laser melting. *Rapid Prototyping Journal*, *12*(5), 254–265. https://doi.org/10.1108/13552540610707013.
102. Kruth, J. P., Deckers, J., Yasa, E., & Wauthlé, R. (2012). Assessing and comparing influencing factors of residual stresses in selective laser melting using a novel analysis method. *Proceedings of*

the Institution of Mechanical Engineers, Part B: Journal of Engineering Manufacture, 226(6), 980-991. https://doi.org/10.1177/0954405412437085.

103. Zaeh, M. F., & Branner, G. (2010). Investigations on residual stresses and deformations in selective laser melting. *Production Engineering*, *4*(1), 35–45. https://doi.org/10.1007/s11740-009-0192-y.
104. Ali, H., Ghadbeigi, H., & Mumtaz, K. (2018). Effect of scanning strategies on residual stress and mechanical properties of Selective Laser Melted Ti6Al4V. *Materials Science and Engineering A*, *712*, 175–187. https://doi.org/10.1016/j.msea.2017.11.103.
105. Song, J., Wu, W., Zhang, L., He, B., Lu, L., Ni, X., Long, Q., & Zhu, G. (2018). Role of scanning strategy on residual stress distribution in Ti-6Al-4V alloy prepared by selective laser melting. *Optik*, *170*, 342–352. https://doi.org/10.1016/j.ijleo.2018.05.128.
106. Lu, Y., Wu, S., Gan, Y., Huang, T., Yang, C., Junjie, L., & Lin, J. (2015). Study on the microstructure, mechanical property and residual stress of SLM Inconel-718 alloy manufactured by differing island scanning strategy. *Optics and Laser Technology*, *75*, 197–206. https://doi.org/10.1016/j.optlastec.2015.07.009.
107. Maawad, E., Sano, Y., Wagner, L., Brokmeier, H. G., & Genzel, C. (2012). Investigation of laser shock peening effects on residual stress state and fatigue performance of titanium alloys. *Materials Science and Engineering A*, *536*, 82–91. https://doi.org/10.1016/j.msea.2011.12.072.
108. Tong, Z., Ren, X., Ren, Y., Dai, F., Ye, Y., Zhou, W., Chen, L., & Ye, Z. (2018). Effect of laser shock peening on microstructure and hot corrosion of TC11 alloy. *Surface and Coatings Technology*, *335*, 32–40. https://doi.org/10.1016/j.surfcoat.2017.12.003.
109. Huang, S., Zhu, Y., Guo, W., Peng, P., & Diao, X. (2017). Impact toughness and microstructural response of Ti-17 titanium alloy subjected to laser shock peening. *Surface and Coatings Technology*, *327*, 32–41. https://doi.org/10.1016/j.surfcoat.2017.07.045.
110. Zhang, X. C., Zhang, Y. K., Lu, J. Z., Xuan, F. Z., Wang, Z. D., & Tu, S. T. (2010). Improvement of fatigue life of Ti-6Al-4V alloy by laser shock peening. *Materials Science and Engineering A*, *527*(15), 3411–3415. https://doi.org/10.1016/j.msea.2010.01.076.
111. Ren, X. D., Zhou, W. F., Liu, F. F., Ren, Y. P., Yuan, S. Q., Ren, N. F., Xu, S. D., & Yang, T. (2016). Microstructure evolution and grain refinement of Ti-6Al-4V alloy by laser shock processing. *Applied Surface Science*, *363*, 44–49. https://doi.org/10.1016/j.apsusc.2015.11.192.
112. Guo, W., Sun, R., Song, B., Zhu, Y., Li, F., Che, Z., Li, B., Guo, C., Liu, L., & Peng, P. (2018). Laser shock peening of laser additive manufactured Ti6Al4V titanium alloy. *Surface and Coatings Technology*, *349*, 503–510. https://doi.org/10.1016/j.surfcoat.2018.06.020.
113. Jin, X., Lan, L., Gao, S., He, B., & Rong, Y. (2020). Effects of laser shock peening on microstructure and fatigue behavior of Ti–6Al–4V alloy fabricated via electron beam melting. *Materials Science and Engineering A*, *780*, 139199 (9 pp.). https://doi.org/10.1016/j.msea.2020.139199.
114. Lan, L., Jin, X., Gao, S., He, B., & Rong, Y. (2020). Microstructural evolution and stress state related to mechanical properties of electron beam melted Ti-6Al-4V alloy modified by laser shock peening. *Journal of Materials Science and Technology*, *50*, 153–161. https://doi.org/10.1016/j.jmst.2019.11.039.
115. Eyzat, Y., Chemkhi, M., Portella, Q., Gardan, J., Remond, J., & Retraint, D. (2019). Characterization and mechanical properties of As-Built SLM Ti-6Al-4V subjected to surface mechanical post-treatment. *Procedia CIRP*, *81*, 1225–1229. https://doi.org/10.1016/j.procir.2019.03.298.
116. Yakout, M., Elbestawi, M. A., & Veldhuis, S. C. (2020). A study of the relationship between thermal expansion and residual stresses in selective laser melting of Ti-6Al-4V. *Journal of Manufacturing Processes*, *52*, 181–192. https://doi.org/10.1016/j.jmapro.2020.01.039.
117. Vastola, G., Zhang, G., Pei, Q. X., & Zhang, Y. W. (2016). Controlling of residual stress in additive manufacturing of Ti6Al4V by finite element modeling. *Additive Manufacturing*, *12*, 231–239. https://doi.org/10.1016/j.addma.2016.05.010.
118. Ning, J., Praniewicz, M., Wang, W., Dobbs, J. R., & Liang, S. Y. (2020). Analytical modeling of part distortion in metal additive manufacturing. International Journal of Advanced Manufacturing Technology, 107(1–2), 49–57. https://doi.org/10.1007/s00170-020-05065-8.

CONCLUSIONS

6 CONCLUSIONS

Additive manufacturing can be considered a disruptive technology because it creates complex parts by adding material instead of removing. This means that there is less waste of raw material during the process and, in addition, there is also no wear of the tool since this technology does not require milling tools or punches.

Currently, PBF-LB is capable of manufacturing polymeric, metallic, ceramic, and composite components. The latter are increasingly being studied, as the scientific community believes in their potential. Furthermore, it is important to emphasize that this process is not able to replace, for now, subtractive manufacturing (SM) completely, because it has high manufacturing roughness. Therefore, when it is necessary to comply with dimensional tolerances, low roughness, or thread components, AM is combined with SM. Besides, one should only employ this manufacturing technology to high-complexity geometrical parts and low volume production since simple components can be made from other manufacturing processes in a quicker way. In addition, the astronomical prices of the AM machines combined with the high prices of the substrate, highly influence the cost of an additively manufactured part. Moreover, it was also seen that, due to the inherent high temperature gradient of the process, residual stresses are created, and parts can suffer geometrical distortion and cause production errors such as layer delamination. A semi-destructive way to compute RS is the hole-drilling strain-gage method, while X-ray CT can be used to quantify internal build defects and part porosity.

From the first scientific article one can conclude that due to the inherent characteristics of the SLM process, i.e. high cooling rates and quick solidification, the expected microstructure of the IN718 in the as-built state is characterized by fine columnar grains and a saturated γ matrix with the presence of the Laves phase and carbides. This heterogeneous microstructure eventually promotes weak and anisotropic mechanical properties, meaning that, for high and cyclic loads applications, heat treatments should be employed. If one seeks to improve the mechanical properties, such as yield and ultimate tensile strength, as well as the hardness of IN718 parts, then a SA heat treatment followed by DA should be conducted. The former is responsible for dissolving the undesired phases, such as carbides and Laves, while the latter promotes the formation of the strengthening phases γ’ and γ’’. The temperature of the SA treatment dictates the expected microstructure, i.e. 1065 °C promotes the full dissolution of the Laves phase, however, if done at 980 °C the Laves phase will not be completely dissolved and results in the formation of the δ phase, since the solution temperature is inferior to the solvus temperature of both phases. Usually, when the printing parameters are optimized, one can obtain a component with a density over 99 %, however, sometimes it may be necessary to conduct a HIP treatment to increase the density of the printed components. In that case, the expected final density of the part is nearly 100 % and normally, leads to microstructure recrystallization. Furthermore, it was also shown that for reducing the part porosity the HIP temperature is more critical than the pressure, and for obtaining optimized results one should use a temperature over 1150 °C and a pressure greater than 100 MPa. It has been seen that residual stresses can be lowered through heat treatments as well as optimized printing parameters, such as a lower beam power and number of layers. In addition, a high scanning speed coupled with shorter scan vectors, i.e. chessboard scanning, has been demonstrated to lower the residual stresses on IN718 parts. Despite that, it was also shown that some researchers found contrary results from the literature as the RS distribution changed after conducting heat treatments. Regarding the RS computation through FEM, it can be concluded that a meticulous study is not viable as it would take days to run in an ordinary computer, however, approximations, i.e. gathering thin layers together, can be successfully done with a 10% degree of error.

From the second paper a few conclusions can be withdrawn, namely the SLM Ti-6Al-4V expected microstructure in the as-built state is characterized by fine acicular α’ martensitic precipitates in columnar original β grains, opposed to an α + β lamellar microstructure obtained through EBM. The latter manufacturing process achieves superior building chamber temperatures, therefore reduces the part’s cooling rate and forms a bimodal microstructure. If one seeks to improve the mechanical properties, such as ductility and hardness, and decrease residual stresses of SLMed Ti-6Al-4V parts, then heat treatments should be conducted. A duplex anneal treatment can be firstly done at 910 °C for 8 hours followed by water-quenching and then 750 °C for 4 hours followed by furnace-cooling. The first step of the heat-treatment creates a bi-modal microstructure of α in the α’ matrix, while the second step promotes the decomposition of α’ into α + β lamellar. Moreover, Hot Isostatic Pressing must be done if one desires to increase the density and fatigue life of the manufactured component, as the aforementioned treatment is responsible for decreasing the size of the internal defects. Besides, one can also predict the expected porosity of the final pieces due to recent developments of trustworthy and efficient computer analytical models. Furthermore, the surface roughness also plays a crucial role in the fatigue life of the final part and is heavily dependent of the manufacturing process, i.e., SLM leads to lower Ra values than EBM, nevertheless, post-machining, sandblasting, and polishing can greatly decrease the Ra values, consequently weaken the crack initiation and improving the fatigue life. Also, it has been seen that residual stresses can be lowered through heat treatments as well as optimized printing parameters, such as the bed pre-heating temperature in EBM or the correlation of distinct process parameters in the Volumetric Energy Density formula on SLMed components. Furthermore, LSP and SMAT post-treatments can also enhance the fatigue life as they induce compressive residual stresses on the surface and increase the microhardness of the components.

Finally, despite all the research over the last years about additively manufactured Inconel 718 and Ti-6Al-4V parts, there are still some problems to overcome. Namely, the mechanical properties variability when subjected to different heat treatments and process parameters. Furthermore, heat treatments should be further investigated and improved because often one sacrifices yield and ultimate tensile strength for ductility. Also, there is still room to improve regarding residual stresses of Inconel 718 and Ti-

6Al-4V components, i.e. research the RS evolution under different heat treatments and printing parameters.

REFERENCES AND OTHER SOURCES OF INFORMATION

BOOKS, SCIENTIFIC PAPERS, INTERNATIONAL STANDARDS AND WEBSITES

7 REFERENCES AND OTHER SOURCES OF INFORMATION

7.1 BOOKS, SCIENTIFIC PAPERS, INTERNATIONAL STANDARDS AND WEBSITES

[1] ASTM F2792-12a, “Standard Terminology for Additive Manufacturing Technologies”, (Withdrawn 2015) ASTM International, pp. 1–3, West Conshohocken, PA, 2012.

[2] Gibson, I., Rosen, D., & Stucker, B. (2015). *Additive manufacturing technologies: 3D printing, rapid prototyping, and direct digital manufacturing, Second Edition* (pp. 1–498). Springer New York.

[3] Goldberg, D. (2018). *History of 3D Printing: It’s Older Than You Are (That Is, If You’re Under 30)*, AutoDesk. [Online], available on: https://www.autodesk.com/redshift/history-of-3d-printing/ [Viewed on 12/2019].

[4] Wohlers, T., Campbell, I., Diegel, O., Kowen, J., & Caffrey, T. (2017). Wohlers Report 2017. Fort Collins.

[5] Holst, A. (2017). *3D printing market size worldwide from 2013 to 2021 (in billion U.S. dollars)*, Statista. [Online], available on: https://www.statista.com/statistics/796237/worldwide-forecast-growth-3d-printing-market/ [Viewed on 12/2019].

[6] Rahmati, S., & Branch, M. (2014). *10.12.3.4 DMLS Tooling* (Vol. 10, pp. 308–309).

[7] Sillani, F., Kleijnen, R. G., Vetterli, M., Schmid, M., & Wegener, K. (2019). Selective laser sintering and multi jet fusion: Process-induced modification of the raw materials and analyses of parts performance. *Additive Manufacturing*, *27*, pp. 32–41.

[8] Calignano, F., Manfredi, D., Ambrosio, E. P., Biamino, S., Lombardi, M., Atzeni, E., & Fino, P. (2017). Overview on additive manufacturing technologies. *Proceedings of the IEEE*, *105*(4), pp. 593-612.

[9] Wudy, K., & Drummer, D. (2019). Aging effects of polyamide 12 in selective laser sintering: Molecular weight distribution and thermal properties. *Additive Manufacturing*, *25*, pp. 1–9.

[10] Zenou M., & Grainger L. (2018). *Additive Manufacturing: Materials, Processes, Quantifications and Applications* (pp. 53-103). Elsevier.

[11] Gu, H., Bashir, Z., & Yang, L. (2019). The re-usability of heat-exposed poly (ethylene terephthalate) powder for laser sintering. *Additive Manufacturing*, *28*, pp. 194–204.

[12] Valino, A. D., Dizon, J. R. C., Espera, A. H., Chen, Q., Messman, J., & Advincula, R. C. (2019). Advances in 3D printing of thermoplastic polymer composites and nanocomposites. *Progress in Polymer Science*, *98*, 101162 (57 pp.).

[13] Song, S., Gao, Z., Lu, B., Bao, C., Zheng, B., & Wang, L. (2019). Performance optimization of complicated structural SiC/Si composite ceramics prepared by selective laser sintering. *Ceramics International, 46*(1), pp. 568-575.

[14] Nofal M., Al-Hallaj S., & Pan Y. (2019). Experimental investigation of phase change materials fabricated using selective laser sintering additive manufacturing. *Journal of Manufacturing Processes, 44*, pp. 91–101.

[15] Gu, H., Bashir, Z., & Yang, L. (2019). The re-usability of heat-exposed poly (ethylene terephthalate) powder for laser sintering. *Additive Manufacturing, 28*, pp. 194–204.

[16] Dadbakhsh, S., Verbelen, L., Verkinderen, O., Strobbe, D., Van Puyvelde, P., & Kruth, J. P. (2017). Effect of PA12 powder reuse on coalescence behaviour and microstructure of SLS parts. *European Polymer Journal, 92*, pp. 250–262.

[17] Kumar, S., & Czekanski, A. (2018). Roadmap to sustainable plastic additive manufacturing. *Materials Today Communications, 15*, pp. 109–113.

[18] Kozlovsky, K., Schiltz, J., Kreider, T., Kumar, M., & Schmid, S. (2018). Mechanical Properties of Reused Nylon Feedstock for Powder-bed Additive Manufacturing in Orthopedics. In *Procedia Manufacturing*, *26*, pp. 826–833.

[19] Nelson, J. C., Vail, N. K., Sun, M. M., Barlow, J. W., Marcus, H. L., Beaman, J. J., & Crawford, R. H. (1991). Post-processing of selective laser sintered polycarbonate parts. *Proceedings of the SFF Symposium Austin, Texas*, (1), pp. 78–85.

[20] Zarringhalam, H., & Hopkinson, N. (2003). Post-processing of DURAFORM parts for rapid manufacture. *Proceedings of the 14th Solid Freeform Fabrication (SFF) Symposium 2003, University of Texas (Austin)*.

[21] Yan, C., Shi, Y., Yang, J., & Liu, J. (2009). Preparation and selective laser sintering of nylon-12 coated metal powders and post processing. *Journal of Materials Processing Technology*, *209*(17), pp. 5785–5792.

[22] Shahzad, K., Deckers, J., Kruth, J. P., & Vleugels, J. (2013). Additive manufacturing of alumina parts by indirect selective laser sintering and post processing. *Journal of Materials Processing Technology*, *213*(9), pp. 1484–1494.

[23] Redwood, B. (2017). *Post Processing for SLS Printed Part*, 3D Hubs. [Online], available on: https://www.3dhubs.com/knowledge-base/post-processing-sls-printed-parts [Viewed on 11/2019].

[24] Chen, F., Wu, J.-M., Wu, H.-Q., Chen, Y., Li, C.-H., & Shi, Y.-S. (2018). Microstructure and mechanical properties of 3Y-TZP dental ceramics fabricated by selective laser sintering combined with cold isostatic pressing. *International Journal of Lightweight Materials and Manufacture*, *1*(4), pp. 239–245.

[25] Zhu, W. (2019). Models for wind tunnel tests based on additive manufacturing technology. *Progress in Aerospace Sciences, 110*, 100541 (15 pp.).

[26] Gayer, C., Ritter, J., Bullemer, M., Grom, S., Jauer, L., Meiners, W., Pfister, A., Reinauer, F., Vucak, M., Wissenbach, K., Fischer, H., Poprawe, R., & Schleifenbaum, J. H. (2019). Development of a solvent-free polylactide/calcium carbonate composite for selective laser sintering of bone tissue engineering scaffolds. *Materials Science and Engineering C*, *101*, pp. 660–673.

[27] Chen, A. N., Gao, F., Li, M., Wu, J. M., Cheng, L. J., Liu, R. Z., Chen, Y., Wen, S. F., Li, C. H., & Shi, Y. S. (2019). Mullite ceramic foams with controlled pore structures and low thermal conductivity prepared by SLS using core-shell structured polyamide12/FAHSs composites. *Ceramics International*, *45*(12), pp. 15538–15546.

[28] Singamneni, S., Velu, R., Behera, M. P., Scott, S., Brorens, P., Harland, D., & Gerrard, J. (2019). Selective laser sintering responses of keratin-based bio-polymer composites. *Materials & Design*, *183*, 108087 (10 pp.).

[29] Meng, Z., He, J., Cai, Z., Wang, F., Zhang, J., Wang, L., Ling, R., & Li, D. (2020). Design and additive manufacturing of flexible polycaprolactone scaffolds with highly-tunable mechanical properties for soft tissue engineering. *Materials and Design*, *189*, 108508 (29 pp.).

[30] Meiners, W. *Shaped body especially prototype or replacement part production*, German patent 19649865 filled on December 2nd of 1996, issued on February 12th of 1998.

[31] Contuzzi, N., Campanelli, S. L., & Ludovico, A. D. (2011). 3D finite element analysis in the Selective Laser Melting process. *International Journal of Simulation Modelling*, *10*(3), pp. 113–121.

[32] Nguyen, Q. B., Luu, D. N., Nai, S. M. L., Zhu, Z., Chen, Z., & Wei, J. (2018). The role of powder layer thickness on the quality of SLM printed parts. *Archives of Civil and Mechanical Engineering*, *18*(3), pp. 948–955.

[33] Yap, C. Y., Chua, C. K., Dong, Z. L., Liu, Z. H., Zhang, D. Q., Loh, L. E., & Sing, S. L. (2015). Review of selective laser melting: Materials and applications. *Applied Physics Reviews 2*, 041101 (16 pp.).

[34] Unknown author. 3D Printing Gold, Silver and precious metals, 3D Alchemy. [Online], available on: https://www.3d-alchemy.co.uk/3d-printing-in-gold.html [Viewed on 11/2019].

[35] Zheng, Y., Zhang, K., Liu, T. T., Liao, W. H., Zhang, C. D., & Shao, H. (2019). Cracks of alumina ceramics by selective laser melting. *Ceramics International*, *45*(1), pp. 175–184.

[36] AlMangour, B., Baek, M. S., Grzesiak, D., & Lee, K. A. (2018). Strengthening of stainless steel by titanium carbide addition and grain refinement during selective laser melting. *Materials Science and Engineering*, *712*, pp. 812–818.

[37] Grainger, L. (2016). Investigating the effects of multiple re-use of Ti6Al4V powder in additive manufacturing. *Renishaw*, pp. 1-10.

[38] Cordova, L., Campos, M., & Tinga, T. (2019). Revealing the Effects of Powder Reuse for Selective Laser Melting by Powder Characterization. *JOM, 71(3)*, pp. 1062-1072.

[39] Ardila, L. C., Garciandia, F., González-Díaz, J. B., Álvarez, P., Echeverria, A., Petite, M. M., Deffley, R., & Ochoa, J. (2014). Effect of IN718 recycled powder reuse on properties of parts manufactured by means of Selective Laser Melting. *Physics Procedia, 56(C)*, pp. 99-107.

[40] Pinto, F. C., Souza Filho, I. R., Sandim, M. J. R., & Sandim, H. R. Z. (2020). Defects in parts manufactured by selective laser melting caused by δ-ferrite in reused 316L steel powder feedstock. *Additive Manufacturing, 31*, 100979 (10 pp.).

[41] ASTM F3055, "Standard specification for additive manufacturing nickel alloy (UNS N07718) with powder bed fusion". ASTM International, West Conshohocken, PA, 2014.

[42] Seifi M., Salem A.A., Satko D.P., Grylls R., & Lewandowski J.J. (2018) Effects of Post-processing on Microstructure and Mechanical Properties of SLM-Processed IN-718. *Proceedings of the 9th International Symposium on Superalloy 718 & Derivatives: Energy, Aerospace, and Industrial Applications. The Minerals, Metals & Materials Series.* Springer, Cham.

[43] Löber, L., Flache, C., Petters, R., Kühn, U., & Eckert, J. (2013). Comparison of different post processing technologies for SLM generated 316l steel parts. *Rapid Prototyping Journal*, *19*(3), pp. 173–179.

[44] Sangid, M. D., Book, T. A., Naragani, D., Rotella, J., Ravi, P., Finch, A., Kenesei, P., Park, J. S., Sharma, H., Almer, J., & Xiao, X. (2018). Role of heat treatment and build orientation in the microstructure sensitive deformation characteristics of IN718 produced via SLM additive manufacturing. *Additive Manufacturing*, *22*, pp. 479–496.

[45] Sing, S. L., Huang, S., & Yeong, W. Y. (2020). Effect of solution heat treatment on microstructure and mechanical properties of laser powder bed fusion produced cobalt-28chromium-6molybdenum. *Materials Science and Engineering A*, *769*, 138511 (26 pp.).

[46] Seabra, M., Azevedo, J., Araújo, A., Reis, L., Pinto, E., Alves, N., Santos, R., Pedro Mortágua, J. (2016). Selective laser melting (SLM) and topology optimization for lighter aerospace components. *Procedia Structural Integrity*, *1*, pp. 289–296.

[47] Cooper, D. E., Stanford, M., Kibble, K. A., & Gibbons, G. J. (2012). Additive Manufacturing for product improvement at Red Bull Technology. *Materials and Design*, *41*, pp. 226–230.

[48] Hansen, C. (2018). *Additive Manufacturing in Formula 1*, Sauber F1 Team. [Online], available on: https://additiveworld.com/upload/file/Sauber_Engineering_AG_20180330.pdf [Viewed on 11/2019].

[49] Noelke, C., Gieseke, M., & Kaierle, S. (2013). Additive manufacturing in micro scale. *ICALEO 2013 - 32nd International Congress on Applications of Lasers and Electro-Optics* (pp. 1–6).

[50] Wu, L., Zhao, Z., Bai, P., Zhao, W., Li, Y., Liang, M., Liao, H., Huo, P., & Li, J. (2020). Wear resistance of graphene nano-platelets (GNPs) reinforced AlSi10Mg matrix composite prepared by SLM. *Applied Surface Science*, *503*, 144156 (33 pp.).

[51] Jung, I. D., Lee, M. S., Lee, J., Sung, H., Choe, J., Son, H. J., Yun, J., Kim, K., Kim, M., Lee, S. W., Yang, S., & Yu, J. H. (2020). Embedding sensors using selective laser melting for self-cognitive metal parts. *Additive Manufacturing*, *33*, 101151 (27 pp.).

[52] Tan, Q., Zhang, J., Mo, N., Fan, Z., Yin, Y., Bermingham, M., Liu, Y., Huang, H., & Zhang, M. X. (2020). A novel method to 3D-print fine-grained AlSi10Mg alloy with isotropic properties via inoculation with LaB6 nanoparticles. *Additive Manufacturing*, *32*, 101034 (29 pp.).

[53] Sun, S., Brandt, M., & Easton, M. (2017). Powder bed fusion processes: An overview. *Laser Additive Manufacturing: Materials, Design, Technologies, and Applications* (pp. 55–77).

[54] Aboulkhair, N. T., Simonelli, M., Parry, L., Ashcroft, I., Tuck, C., & Hague, R. (2019). 3D printing of Aluminium alloys: Additive Manufacturing of Aluminium alloys using selective laser melting. *Progress in Materials Science, 106*, 100578 (45 pp.).

[55] Ali, H., Ghadbeigi, H., & Mumtaz, K. (2018). Effect of scanning strategies on residual stress and mechanical properties of Selective Laser Melted Ti6Al4V. *Materials Science and Engineering A*, *712*, pp. 175–187.

[56] Nguyen, Q. B., Luu, D. N., Nai, S. M. L., Zhu, Z., Chen, Z., & Wei, J. (2018). The role of powder layer thickness on the quality of SLM printed parts. *Archives of Civil and Mechanical Engineering*, *18*(3), pp. 948–955.

[57] Majeed, A., Ahmed, A., Salam, A., & Sheikh, M. Z. (2019). Surface quality improvement by parameters analysis, optimization and heat treatment of AlSi10Mg parts manufactured by SLM additive manufacturing. *International Journal of Lightweight Materials and Manufacture, 2*(4), pp. 288-295.

[58] Tonelli, L., Fortunato, A., & Ceschini, L. (2020). CoCr alloy processed by Selective Laser Melting (SLM): effect of Laser Energy Density on microstructure, surface morphology, and hardness. *Journal of Manufacturing Processes*, *52*, pp. 106–119.

[59] Bourell, D., Kruth, J. P., Leu, M., Levy, G., Rosen, D., Beese, A. M., & Clare, A. (2017). Materials for additive manufacturing. *CIRP Annals - Manufacturing Technology*, *66*(2), pp. 659–681.

[60] Li, N., Huang, S., Zhang, G., Qin, R., Liu, W., Xiong, H., Shi, G., Blackburn, J. (2019). Progress in additive manufacturing on new materials: A review. *Journal of Materials Science and Technology*, *35*(2), pp. 242-269.

[61] Unknown author. *Properties of Titanium Ti-6Al-4V (Grade 5)*, Matweb. [Online], available on: http://www.matweb.com/search/datasheet.aspx?MatGUID=10d463eb3d3d4ff48fc57e0ad1037434 [Viewed on 12/2019].

[62] Zuback, J. S., & DebRoy, T. (2018). The hardness of additively manufactured alloys. *Materials*, *11*(11), 2070 (41 pp.).

[63] Castellanos, S. D., Alves, J. L., & Neto, R. J. (2017). A comparative study of manufacturing processes of complex surface parts in Titanium Ti6Al4V. *Ciência e Tecnologia Dos Materiais*, *29* (2), pp. 73–78.

[64] Ngo, T. D., Kashani, A., Imbalzano, G., Nguyen, K. T. Q., & Hui, D. (2018). Additive manufacturing (3D printing): A review of materials, methods, applications and challenges. *Composites Part B: Engineering, 143,* pp. 172-196.

[65] Unknown author. *Case study of a Gooseneck Krueger Flap Actuation Bracket*, SLM Solutions. [Online], available on: https://www.slmsolutions.com/fileadmin/user_upload/Case_Study_Asco_Gooseneck_Bracket1912.pdf [Viewed on 12/2019].

[66] Lopez-Galilea, I., Ruttert, B., He, J., Hammerschmidt, T., Drautz, R., Gault, B., & Theisen, W. (2019). Additive manufacturing of CMSX-4 Ni-base superalloy by selective laser melting: Influence of processing parameters and heat treatment. *Additive Manufacturing*, *30*, 100874 (12 pp.).

[67] Unknown author. *Case Study of a Monolithic Thrust Chamber*, SLM Solutions. [Online], available on: https://www.slmsolutions.com/fileadmin/user_upload/Case_Study_CellCore_Thrust_Chamber.pdf [Viewed on 12/2019].

[68] Tucho, W. M., Cuvillier, P., Sjolyst-Kverneland, A., & Hansen, V. (2017). Microstructure and hardness studies of Inconel 718 manufactured by selective laser melting before and after solution heat treatment. *Materials Science and Engineering A, 689*, pp. 220–232.

[69] Zhang, D., Feng, Z., Wang, C., Wang, W., Liu, Z., & Niu, W. (2018). Comparison of microstructures and mechanical properties of Inconel 718 alloy processed by selective laser melting and casting. *Materials Science and Engineering A, 724*, pp. 357–367.

[70] Wang, X., Gong, X., & Chou, K. (2017). Review on powder-bed laser additive manufacturing of Inconel 718 parts. *Proceedings of the Institution of Mechanical Engineers, Part B: Journal of Engineering Manufacture, 231*(11), pp. 1890-1903.

[71] Li, X., Shi, J. J., Wang, C. H., Cao, G. H., Russell, A. M., Zhou, Z. J., Li, C. P., & Chen, G. F. (2018). Effect of heat treatment on microstructure evolution of Inconel 718 alloy fabricated by selective laser melting. *Journal of Alloys and Compounds*, *764*, pp. 639–649.

[72] AMS 5663, “Nickel Alloy, Corrosion and Heat Resistant, Bars, Forgings, and Rings 52.5Ni 19Cr 3.0Mo 5.1Cb 0.90Ti 0.50Al 19Fe, Consumable Electrode or Vacuum Induction Melted 1775°F (968°C) Solution and Precipitation Heat Treated”. SAE International, 1965.

[73] AMS 5383, “Nickel Alloy, Corrosion and Heat-Resistant, Investment Castings, 52.5Ni - 19Cr - 3.0Mo - 5.1Cb(Nb) - 0.90Ti - 0.60Al - 18Fe, Vacuum Melted Homogenization and Solution Heat Treated”. SAE International, 1966.

[74] SAE AMS 5664E, “Nickel Alloy, Corrosion and Heat Resistant, Bars, Forgings, and Rings 52.5Ni 19Cr 3.0Mo 5.1Cb 0.90Ti 0.50Al 18Fe Consumable Electrode or Vacuum Induction Melted 1950°F (1066°C) Solution Heat Treated, Precipitation Hardenable”. SAE International, 2001.

[75] Lu, Y., Wu, S., Gan, Y., Huang, T., Yang, C., Junjie, L., & Lin, J. (2015). Study on the microstructure, mechanical property and residual stress of SLM Inconel-718 alloy manufactured by differing island scanning strategy. *Optics and Laser Technology*, *75*, pp. 197–206.

[76] Yang, H., Meng, L., Luo, S., & Wang, Z. (2020). Microstructural evolution and mechanical performances of selective laser melting Inconel 718 from low to high laser power. *Journal of Alloys and Compounds*, *828*, 154473 (12 pp.).

[77] Moussaoui, K., Rubio, W., Mousseigne, M., Sultan, T., & Rezai, F. (2018). Effects of Selective Laser Melting additive manufacturing parameters of Inconel 718 on porosity, microstructure and mechanical properties. *Materials Science and Engineering A*, *735*, pp. 182–190.

[78] Wan, H. Y., Zhou, Z. J., Li, C. P., Chen, G. F., & Zhang, G. P. (2019). Effect of scanning strategy on mechanical properties of selective laser melted Inconel 718. *Materials Science and Engineering A*, *753*, pp. 42–48.

[79] Unknown author. *Properties of 3D Systems LaserForm® CoCr*, Matweb. [Online], available on: http://www.matweb.com/search/DataSheet.aspx?MatGUID=e290fb660ab44fd6a421c3f3cfd4170e&ckck=1 [Viewed on 12/2019].

[80] Ni, J., Ling, H., Zhang, S., Wang, Z., Peng, Z., Benyshek, C., Zan, R., Miri, A. K., Li, Z., Zhang, X., Lee, J., Lee, K. J., Tebon, P., Hoffman, T., Dokmeci, M. R., Ashammakhi, N., Li, X., & Khademhosseini, A. (2019). Three-dimensional printing of metals for biomedical applications. *Materials Today Bio*, *3*, 100024 (18 pp.).

[81] Unknown author. *ASTM F75 CoCr Alloy Properties*, ArcAM. [Online], available on: http://www.arcam.com/wp-content/uploads/Arcam-ASTM-F75-CobaltChrome.pdf [Viewed on 12/2019].

[82] Unknown author. *Case Study of a Motor Housing for an Electric Race Car*, SLM Solutions. [Online], available on: https://www.slmsolutions.com/fileadmin/user_upload/Case_Study_Lions_Racing_Team_Motor_Housing.pdf [Viewed on 12/2019].

[83] Deng, D., Peng, R. L., Brodin, H., & Moverare, J. (2018). Microstructure and mechanical properties of Inconel 718 produced by selective laser melting: Sample orientation dependence and effects of post heat treatments. *Materials Science and Engineering A, 713*, pp. 294–306.

[84] Bartlett, J. L., & Li, X. (2019). An overview of residual stresses in metal powder bed fusion. *Additive Manufacturing, 27,* pp. 131-149.

[85] Yadroitsev, I., & Yadroitsava, I. (2015). Evaluation of residual stress in stainless steel 316L and Ti6Al4V samples produced by selective laser melting. *Virtual and Physical Prototyping*, *10*(2), pp. 67–76.

[86] Guo, J., Fu, H., Pan, B., & Kang, R. (2020). Recent progress of residual stress measurement methods: A review. *Chinese Journal of Aeronautics*. In press, https://doi.org/10.1016/j.cja.2019.10.010.

[87] ASTM E 837-08. (2008). Standard Test Method for Determining Residual Stresses by the Hole-Drilling Strain-Gages, *1*, pp. 1–17.

[88] Group, V. P. (2007). Measurement of Residual Stresses by the Hole-Drilling Strain Gage Method, Tech Note TN-503.

[89] Ajovalasit, A., Scafidi, M., Zuccarello, B., Beghini, M., & Bertini, L. (2010). The hole-drilling strain gauge method for the measurement of uniform or non-uniform residual stresses. *Working Group on Residual Stresses* (pp. 1–70).

[90] ASTM E 1441-00. (2005). Standard Guide for Computed Tomography Imaging, *1*, pp. 1–33.

[91] Zanini, F., Sbettega, E., & Carmignato, S. (2018). X-ray computed tomography for metal additive manufacturing: Challenges and solutions for accuracy enhancement. *Procedia CIRP*, *75*, pp. 114–118.

[92] Du Plessis, A., Yadroitsev, I., Yadroitsava, I., & Le Roux, S. G. (2018). X-Ray Microcomputed Tomography in Additive Manufacturing: A Review of the Current Technology and Applications. *3D Printing and Additive Manufacturing*, *5*(3), pp. 227–247.

[93] Kim, F. H., Villarraga-Gómez, H., & Moylan, S. P. (2016). Inspection of Embedded Internal Features in Additive Manufactured Metal using metrological X-ray computed tomography. *American Society for Precision Engineering,* pp. 191-195.

ANNEXES

8 ANNEXES

8.1 ANNEX 1 – Ti6Al4V ALLOY DATASHEET

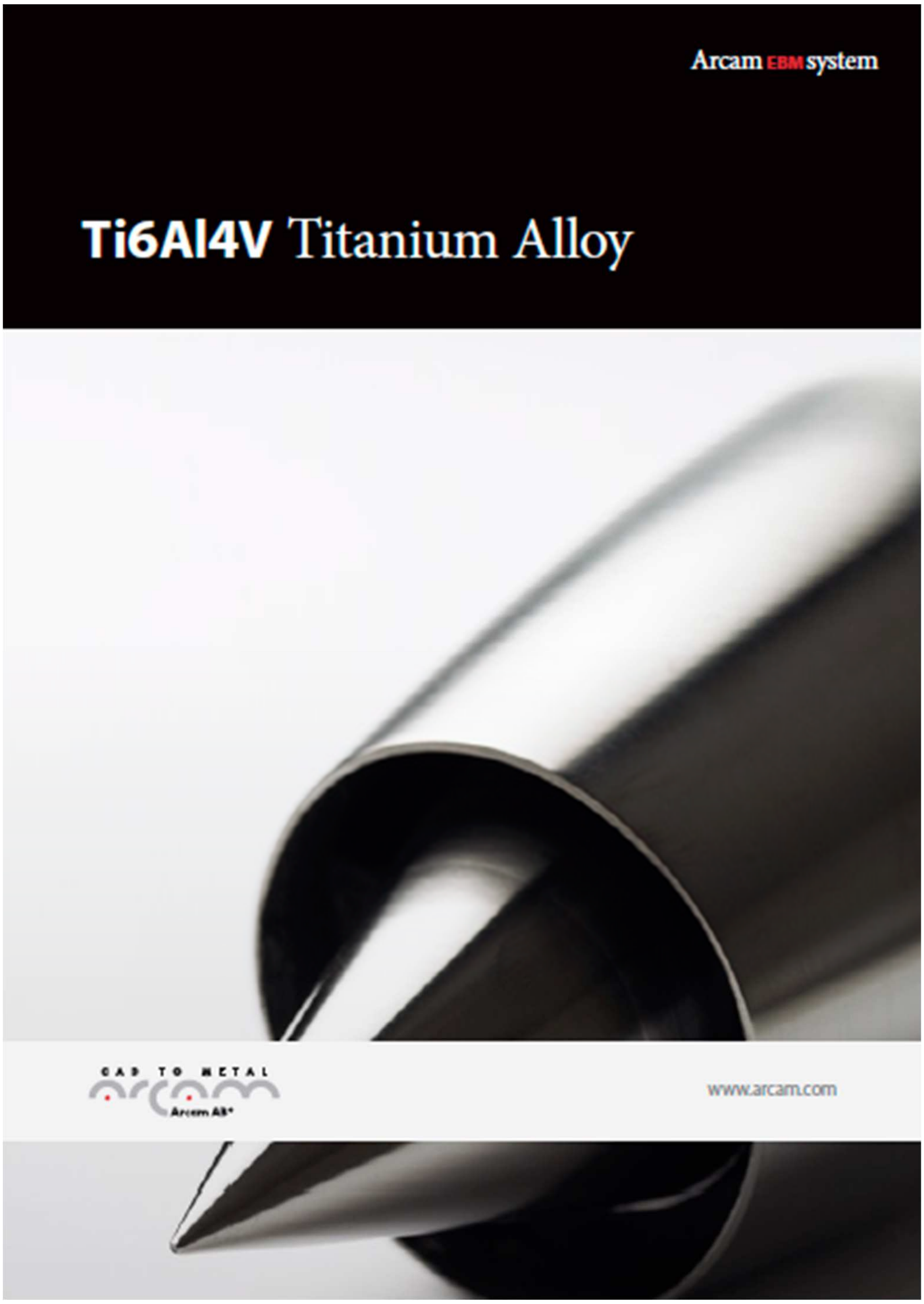

Arcam EBM system

Ti6Al4V Titanium Alloy

CAD TO METAL
arcam
Arcam AB®

www.arcam.com

Arcam EBM system

Ti6Al4V Titanium Alloy

General characteristics
The high strength, low weight ratio and outstanding corrosion resistance inherent to titanium and its alloys has led to a wide and diversified range of successful applications which demand high levels of reliable performance in surgery and medicine as well as in aerospace, automotive, chemical plant, power generation, oil and gas extraction, sports, and other major industries.

In the majority of these and other engineering applications titanium has replaced heavier, less serviceable or less cost-effective materials. Designing with titanium taking all factors into account has resulted in reliable, economic and more durable systems and components, which in many situations have substantially exceeded performance and service life expectations.

Titanium is available in several different grades. Pure titanium is not as strong as the different titanium alloys are.

Special characteristics
Ti6Al4V is the most widely used titanium alloy. It features good machinability and excellent mechanical properties. The Ti6Al4V alloy offers the best all-round performance for a variety of weight reduction applications in aerospace, automotive and marine equipment.

Ti6Al4V also has numerous applications in the medical industry. Biocompatibility of Ti6Al4V is excellent, especially when direct contact with tissue or bone is required.

Applications
Ti6Al4V is typically used for:

- Direct Manufacturing of parts and prototypes for racing and aerospace industry
- Biomechanical applications, such as implants and prosthesis
- Marine applications
- Chemical industry
- Gas turbines

Powder specification
The Arcam Titanium Ti6Al4V (Grade 5) powder has a particle size between 45 and 100 microns. This limit on the minimum particle size ensures safe handling of the powder.

Please refer to the Arcam MSDS (Material Safety Data Sheet) for more information about the handling and safety of the Arcam Ti6Al4V alloy.

Race car gearbox manufactured with Arcam EBM in Ti6Al4V.

CHEMICAL SPECIFICATION

	Arcam Ti6Al4V, Typical	Ti6Al4V, Required*	Ti6Al4V, Required**
Aluminium, Al	6%	5,5–6,75%	5,5–6,75%
Vanadium, V	4%	3,5–4,5%	3,5–4,5%
Carbon, C	0,03%	< 0,1%	< 0,08%
Iron, Fe	0,1%	< 0,3%	< 0,3%
Oxygen, O	0,15%	< 0,2%	< 0,2%
Nitrogen, N	0,01%	< 0,05%	< 0,05%
Hydrogen, H	0,003%	< 0,015%	< 0,015%
Titanium, Ti	Balance	Balance	Balance

*ASTM F1108 (cast material) **ASTM F1472 (wrought material)

MECHANICAL PROPERTIES

	Arcam Ti6Al4V, Typical	Ti6Al4V, Required**	Ti6Al4V, Required***
Yield Strength (Rp 0,2)	950 MPa	758 MPa	860 MPa
Ultimate Tensile Strength (Rm)	1020 MPa	860 MPa	930 MPa
Elongation	14%	>8%	>10%
Reduction of Area	40%	>14%	>25%
Fatigue strength* @600 MPa	>10,000,000 cycles		
Rockwell Hardness	33 HRC		
Modulus of Elasticity	120 GPa		

*After Hot Isostatic Pressing **ASTM F1108 (cast material) ***ASTM F1472 (wrought material)
The mechanical properties of materials produced in the EBM process are comparable to wrought annealed materials and are better than cast materials.

Arcam Ti6Al4V High Cycle Fatigue Test

HCF S/N diagram in MPa units

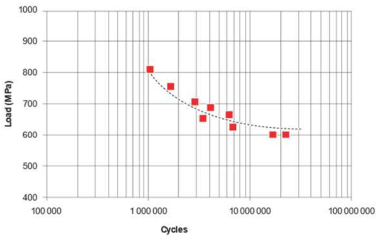

POST PROCESSING

Heat treatment
Hot Isostatic Pressing (HIP) is recommended for fatigue-loaded components. The following HIP parameters are recommended:
- 920° C
- 100 MPa
- 120 minutes

Machining
Ti6Al4V parts manufactured in the EBM process feature good machinability and can be machined as stock parts.

The following factors contribute to efficient machining of Ti6Al4V parts:
- Low cutting speeds
- High feed rate
- Generous quantities of cutting fluid
- Sharp tools
- Rigid setup

Welding
Ti6Al4V may be welded by a wide variety of conventional fusion and solid-state processes, although its chemical reactivity typically requires special measures and procedures.

8.2 ANNEX 2 – IN 718 ALLOY DATASHEET

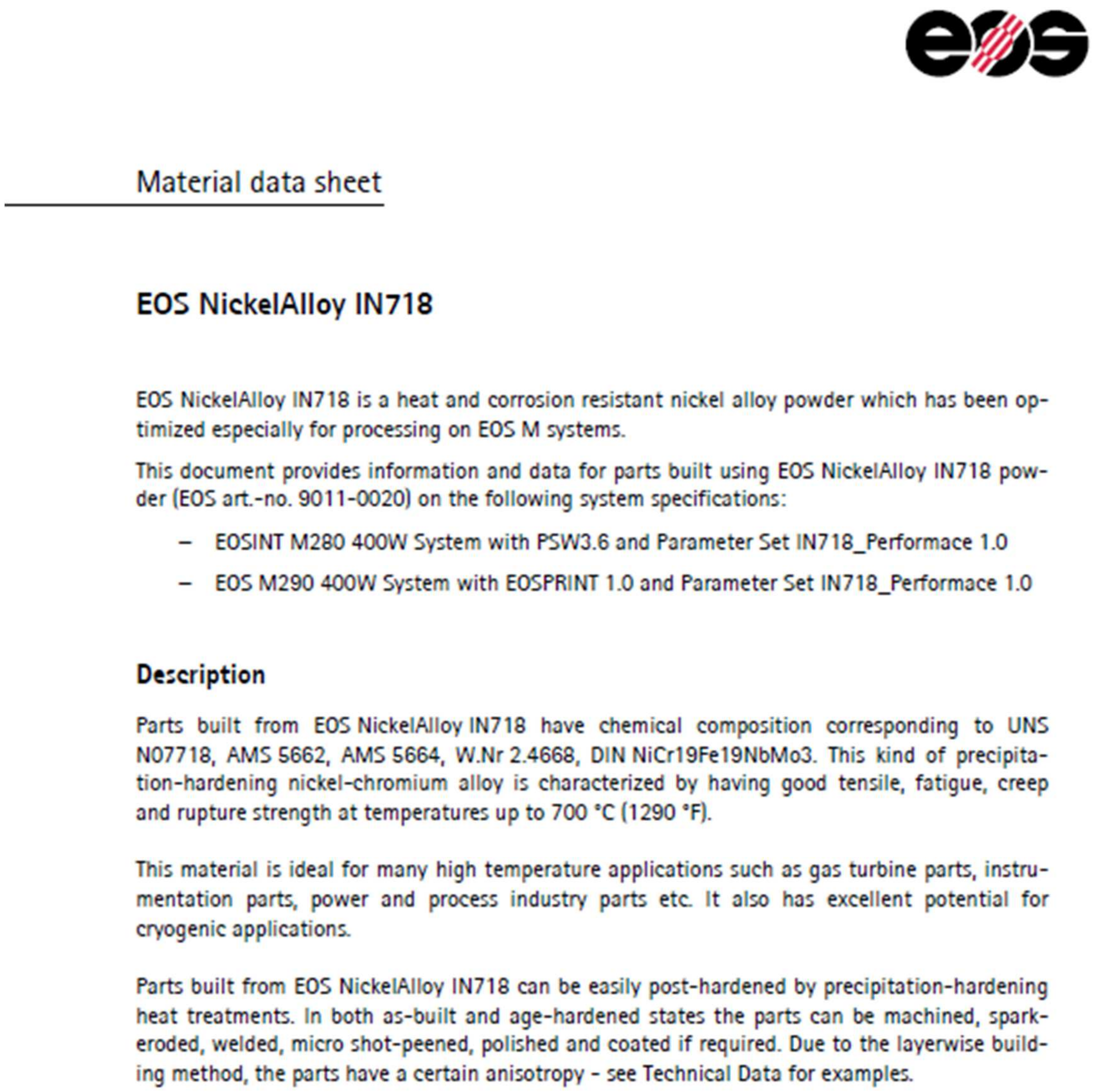

Material data sheet

EOS NickelAlloy IN718

EOS NickelAlloy IN718 is a heat and corrosion resistant nickel alloy powder which has been optimized especially for processing on EOS M systems.

This document provides information and data for parts built using EOS NickelAlloy IN718 powder (EOS art.-no. 9011-0020) on the following system specifications:

- EOSINT M280 400W System with PSW3.6 and Parameter Set IN718_Performace 1.0
- EOS M290 400W System with EOSPRINT 1.0 and Parameter Set IN718_Performace 1.0

Description

Parts built from EOS NickelAlloy IN718 have chemical composition corresponding to UNS N07718, AMS 5662, AMS 5664, W.Nr 2.4668, DIN NiCr19Fe19NbMo3. This kind of precipitation-hardening nickel-chromium alloy is characterized by having good tensile, fatigue, creep and rupture strength at temperatures up to 700 °C (1290 °F).

This material is ideal for many high temperature applications such as gas turbine parts, instrumentation parts, power and process industry parts etc. It also has excellent potential for cryogenic applications.

Parts built from EOS NickelAlloy IN718 can be easily post-hardened by precipitation-hardening heat treatments. In both as-built and age-hardened states the parts can be machined, spark-eroded, welded, micro shot-peened, polished and coated if required. Due to the layerwise building method, the parts have a certain anisotropy - see Technical Data for examples.

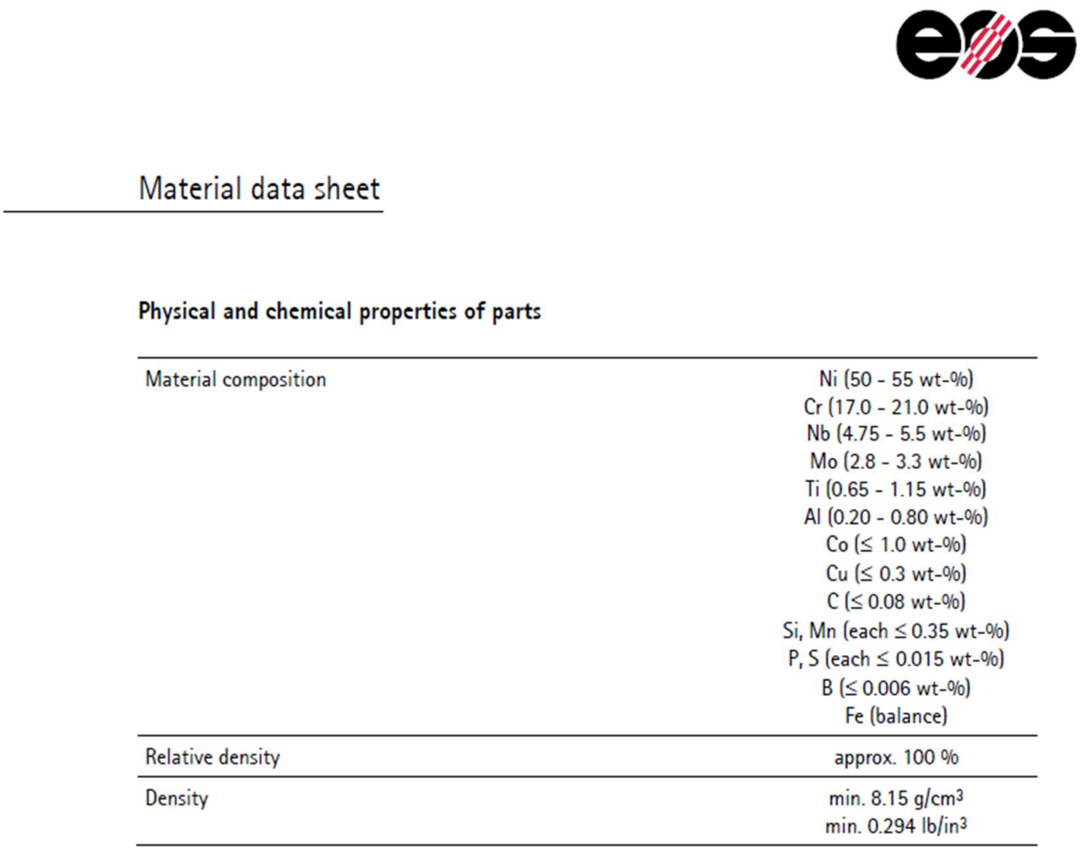

Material data sheet

Physical and chemical properties of parts

Material composition	Ni (50 - 55 wt-%) Cr (17.0 - 21.0 wt-%) Nb (4.75 - 5.5 wt-%) Mo (2.8 - 3.3 wt-%) Ti (0.65 - 1.15 wt-%) Al (0.20 - 0.80 wt-%) Co (≤ 1.0 wt-%) Cu (≤ 0.3 wt-%) C (≤ 0.08 wt-%) Si, Mn (each ≤ 0.35 wt-%) P, S (each ≤ 0.015 wt-%) B (≤ 0.006 wt-%) Fe (balance)
Relative density	approx. 100 %
Density	min. 8.15 g/cm³ min. 0.294 lb/in³

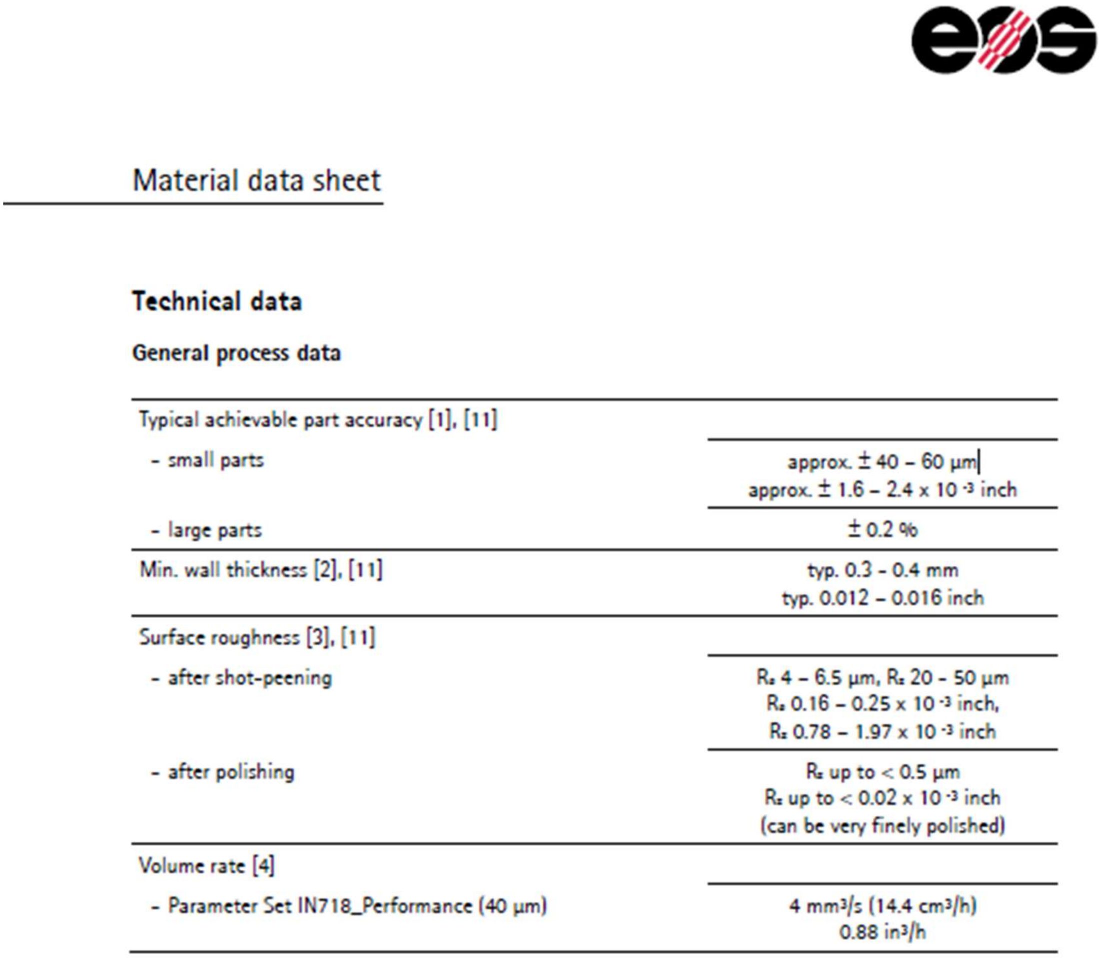

Material data sheet

Technical data

General process data

Typical achievable part accuracy [1], [11]	
- small parts	approx. ± 40 – 60 µm approx. ± 1.6 – 2.4 x 10^{-3} inch
- large parts	± 0.2 %
Min. wall thickness [2], [11]	typ. 0.3 - 0.4 mm typ. 0.012 – 0.016 inch
Surface roughness [3], [11]	
- after shot-peening	R_a 4 – 6.5 µm, R_z 20 - 50 µm R_a 0.16 – 0.25 x 10^{-3} inch, R_z 0.78 – 1.97 x 10^{-3} inch
- after polishing	R_z up to < 0.5 µm R_z up to < 0.02 x 10^{-3} inch (can be very finely polished)
Volume rate [4]	
- Parameter Set IN718_Performance (40 µm)	4 mm^3/s (14.4 cm^3/h) 0.88 in^3/h

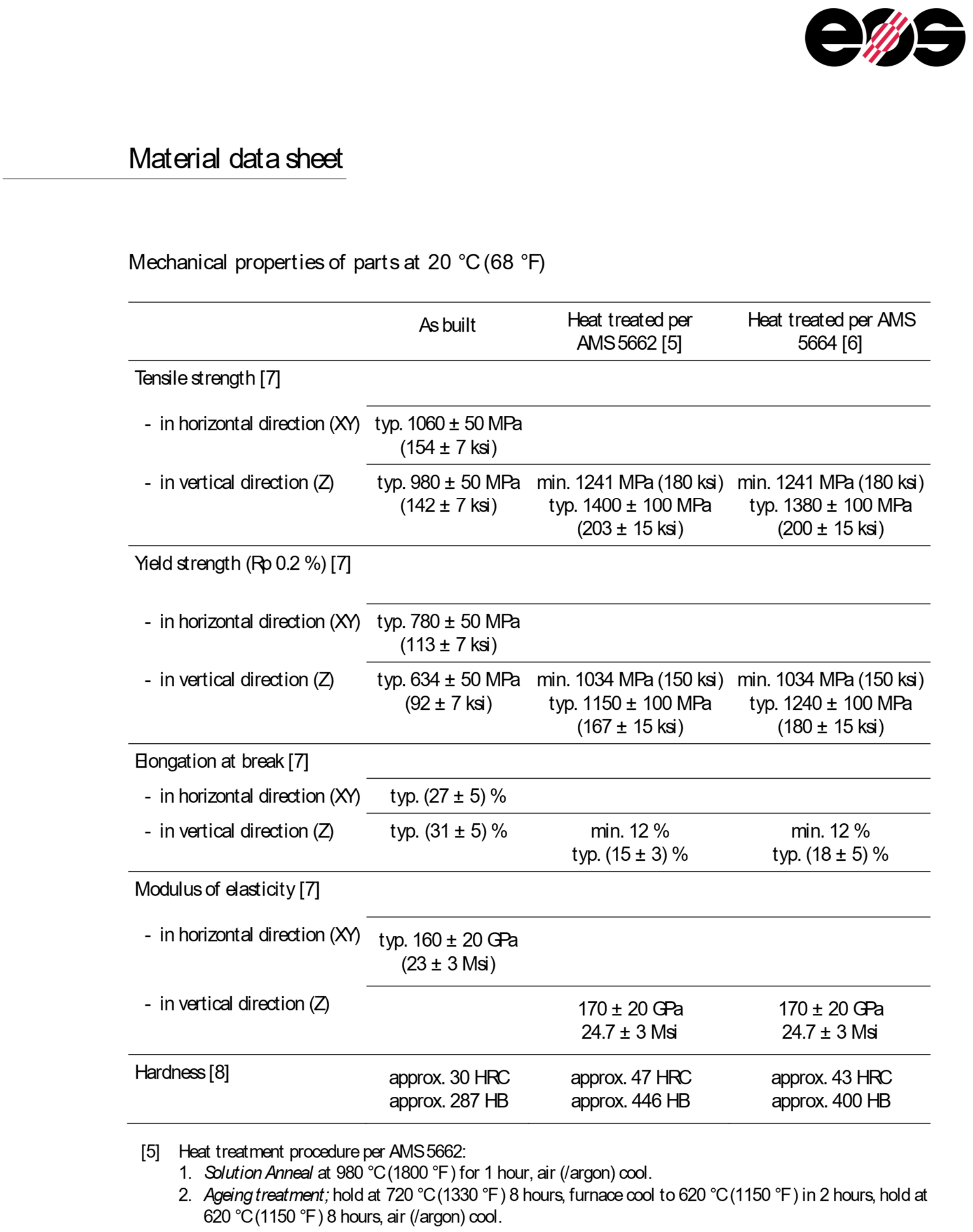

Material data sheet

Mechanical properties of parts at 20 °C (68 °F)

	As built	Heat treated per AMS 5662 [5]	Heat treated per AMS 5664 [6]
Tensile strength [7]			
- in horizontal direction (XY)	typ. 1060 ± 50 MPa (154 ± 7 ksi)		
- in vertical direction (Z)	typ. 980 ± 50 MPa (142 ± 7 ksi)	min. 1241 MPa (180 ksi) typ. 1400 ± 100 MPa (203 ± 15 ksi)	min. 1241 MPa (180 ksi) typ. 1380 ± 100 MPa (200 ± 15 ksi)
Yield strength (Rp 0.2 %) [7]			
- in horizontal direction (XY)	typ. 780 ± 50 MPa (113 ± 7 ksi)		
- in vertical direction (Z)	typ. 634 ± 50 MPa (92 ± 7 ksi)	min. 1034 MPa (150 ksi) typ. 1150 ± 100 MPa (167 ± 15 ksi)	min. 1034 MPa (150 ksi) typ. 1240 ± 100 MPa (180 ± 15 ksi)
Elongation at break [7]			
- in horizontal direction (XY)	typ. (27 ± 5) %		
- in vertical direction (Z)	typ. (31 ± 5) %	min. 12 % typ. (15 ± 3) %	min. 12 % typ. (18 ± 5) %
Modulus of elasticity [7]			
- in horizontal direction (XY)	typ. 160 ± 20 GPa (23 ± 3 Msi)		
- in vertical direction (Z)		170 ± 20 GPa 24.7 ± 3 Msi	170 ± 20 GPa 24.7 ± 3 Msi
Hardness [8]	approx. 30 HRC approx. 287 HB	approx. 47 HRC approx. 446 HB	approx. 43 HRC approx. 400 HB

[5] Heat treatment procedure per AMS 5662:

1. *Solution Anneal* at 980 °C (1800 °F) for 1 hour, air (/argon) cool.
2. *Ageing treatment;* hold at 720 °C (1330 °F) 8 hours, furnace cool to 620 °C (1150 °F) in 2 hours, hold at 620 °C (1150 °F) 8 hours, air (/argon) cool.

8.3 ANNEX 3 – CoCr ALLOY DATASHEET

LaserForm® CoCr (B)

Cobalt-chromium-molybdenum alloy fine-tuned for use with DMP Flex 100, ProX® DMP 200 and ProX® DMP 300 metal printers producing industrial parts with high corrosion and wear resistance that also require high temperature resistance.

LaserForm CoCr (B) is formulated and fine-tuned specifically for 3D Systems DMP Flex 100, ProX® DMP 200 and ProX® DMP 300 metal 3D printers to deliver high part quality and consistent part properties. The print parameter database that 3D Systems provides together with the material has been extensively developed, tested and optimized in 3D Systems' part production facilities that hold the unique expertise of printing 500,000 challenging metal production parts in various materials year over year. For a 24/7 production operation 3D Systems' thorough Supplier Quality Management System guarantees consistent, monitored material quality for reliable process results.

Material Description

Cobalt-chromium-molybdenum alloys are known for their high strength and hardness and retain these properties even at elevated temperatures. In addition, they spontaneously form a protective passive film, which makes LaserForm CoCr (B) both corrosion resistant and biocompatible.

These benefits make LaserForm CoCr (B) the ideal material for medical tools and devices, molds and dies, industrial, high wear applications and parts requiring high strength at elevated temperatures.

Classification

The chemical composition of LaserForm® CoCr (B) conforms to the requirements of the ASTM F75 and is indicated in the table below in % of weight.

Mechanical Properties[1,2]

MEASUREMENT	CONDITION	METRIC		U.S.	
		AS-BUILT	AFTER SOLUTION ANNEAL	AS-BUILT	AFTER SOLUTION ANNEAL
Youngs modulus (GPa | ksi)	ASTM E8M				
Horizontal direction - XY Vertical direction - Z		220 ± 40 170 ± 40	240 ± 40 220 ± 40	31900 ± 5800 24700 ± 5800	34800 ± 5800 31900 ± 5800
Ultimate strength (MPa | ksi)	ASTM E8M				
Horizontal direction - XY Vertical direction - Z		1150 ± 80 1090 ± 40	1050 ± 50 1040 ± 50	165 ± 12 160 ± 6	150 ± 7 150 ± 7
Yield strength Rp0.2% (MPa | ksi)	ASTM E8M				
Horizontal direction - XY Vertical direction - Z		840 ± 80 630 ± 40	590 ± 40 570 ± 40	120 ± 12 90 ± 6	85 ± 6 85 ± 6
Elongation at break (%)	ASTM E8M				
Horizontal direction - XY Vertical direction - Z		6 ± 2 15 ± 4	33 ± 6 35 ± 6	6 ± 2 15 ± 4	33 ± 6 35 ± 6
Reduction of area (%)	ASTM E8M				
Horizontal direction - XY Vertical direction - Z		13 ± 8 19 ± 8	31 ± 6 32 ± 6	13 ± 8 19 ± 8	31 ± 6 32 ± 6
Hardness, Rockwell C	ASTM E18	32 ± 5	26 ± 5	32 ± 5	26 ± 5

---

[1] Parts manufactured with standard parameters on DMP Flex 100 and ProX® DMP 200

[2] Values based on average and double standard deviation

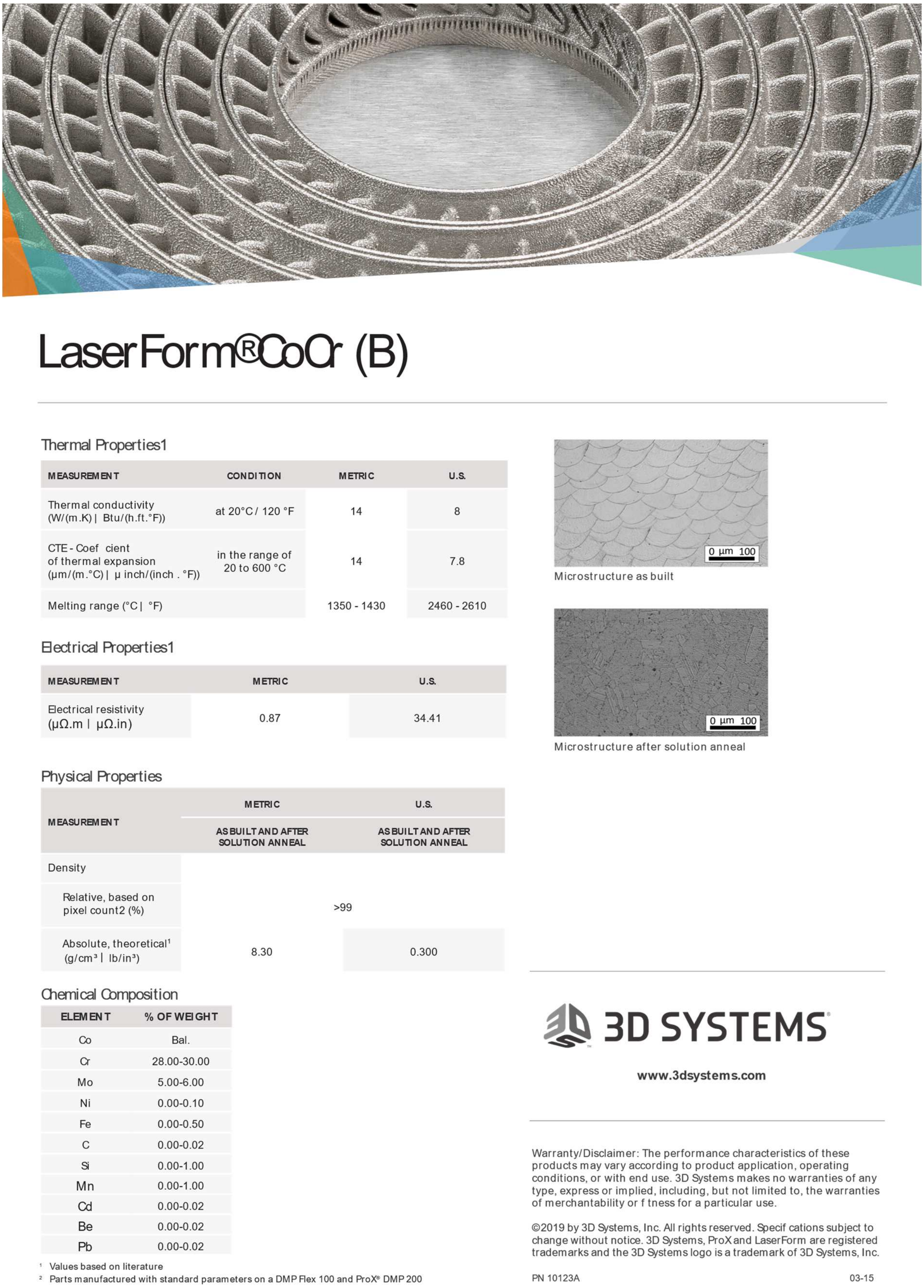

LaserForm® CoCr (B)

Thermal Properties1

MEASUREMENT	CONDITION	METRIC	U.S.
Thermal conductivity (W/(m.K) | Btu/(h.ft.°F))	at 20°C / 120 °F	14	8
CTE - Coefficient of thermal expansion (µm/(m.°C) | µ inch/(inch . °F))	in the range of 20 to 600 °C	14	7.8
Melting range (°C | °F)		1350 - 1430	2460 - 2610

Electrical Properties1

MEASUREMENT	METRIC	U.S.
Electrical resistivity (µΩ.m | µΩ.in)	0.87	34.41

Physical Properties

MEASUREMENT	METRIC	U.S.
	AS BUILT AND AFTER SOLUTION ANNEAL	AS BUILT AND AFTER SOLUTION ANNEAL
Density		
Relative, based on pixel count2 (%)	>99	
Absolute, theoretical¹ (g/cm³ | lb/in³)	8.30	0.300

Chemical Composition

ELEMENT	% OF WEIGHT
Co	Bal.
Cr	28.00-30.00
Mo	5.00-6.00
Ni	0.00-0.10
Fe	0.00-0.50
C	0.00-0.02
Si	0.00-1.00
Mn	0.00-1.00
Cd	0.00-0.02
Be	0.00-0.02
Pb	0.00-0.02

Microstructure as built

Microstructure after solution anneal

3D SYSTEMS

www.3dsystems.com

PN 10123A 03-15

---

[1] Values based on literature

[2] Parts manufactured with standard parameters on a DMP Flex 100 and ProX® DMP 200

8.4 ANNEX 4 – AlSi10Mg ALLOY DATASHEET

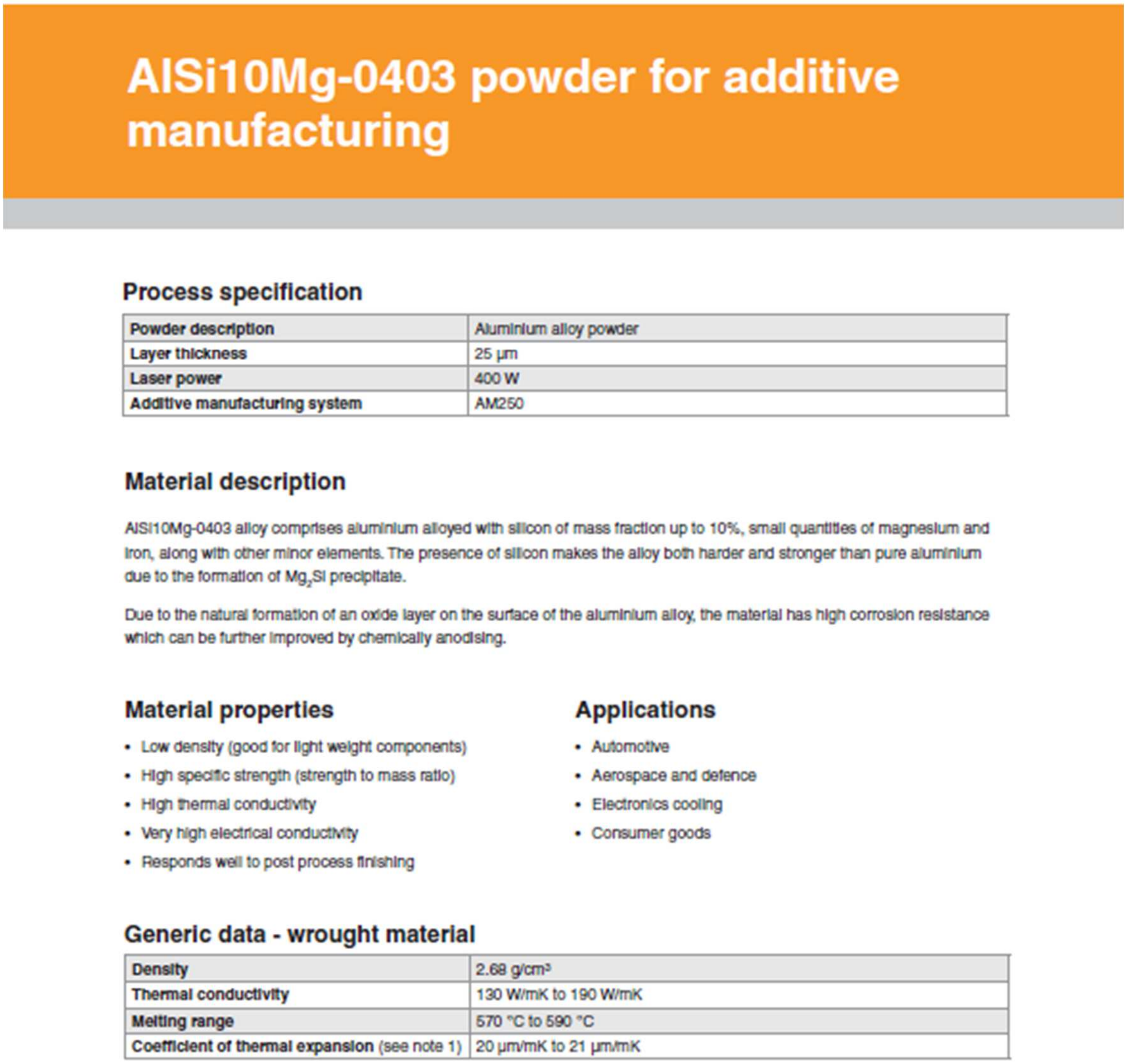

AlSi10Mg-0403 powder for additive manufacturing

Process specification

Powder description	Aluminium alloy powder
Layer thickness	25 µm
Laser power	400 W
Additive manufacturing system	AM250

Material description

AlSi10Mg-0403 alloy comprises aluminium alloyed with silicon of mass fraction up to 10%, small quantities of magnesium and iron, along with other minor elements. The presence of silicon makes the alloy both harder and stronger than pure aluminium due to the formation of Mg_2Si precipitate.

Due to the natural formation of an oxide layer on the surface of the aluminium alloy, the material has high corrosion resistance which can be further improved by chemically anodising.

Material properties

- Low density (good for light weight components)
- High specific strength (strength to mass ratio)
- High thermal conductivity
- Very high electrical conductivity
- Responds well to post process finishing

Applications

- Automotive
- Aerospace and defence
- Electronics cooling
- Consumer goods

Generic data - wrought material

Density	2.68 g/cm³
Thermal conductivity	130 W/mK to 190 W/mK
Melting range	570 °C to 590 °C
Coefficient of thermal expansion (see note 1)	20 µm/mK to 21 µm/mK

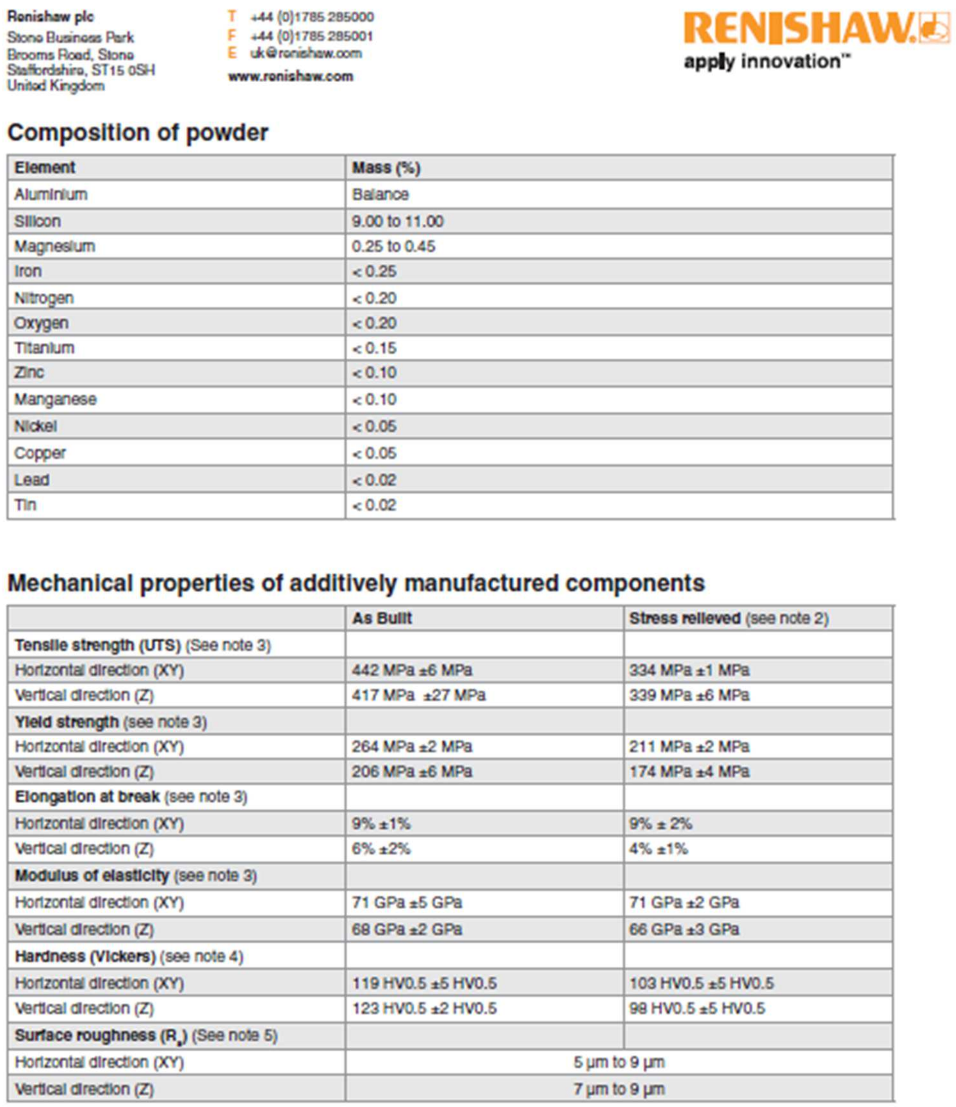

Renishaw plc
Stone Business Park
Brooms Road, Stone
Staffordshire, ST15 0SH
United Kingdom

T +44 (0)1785 285000
F +44 (0)1785 285001
E uk@renishaw.com
www.renishaw.com

Composition of powder

Element	**Mass (%)**
Aluminium	Balance
Silicon	9.00 to 11.00
Magnesium	0.25 to 0.45
Iron	< 0.25
Nitrogen	< 0.20
Oxygen	< 0.20
Titanium	< 0.15
Zinc	< 0.10
Manganese	< 0.10
Nickel	< 0.05
Copper	< 0.05
Lead	< 0.02
Tin	< 0.02

Mechanical properties of additively manufactured components

	As Built	**Stress relieved** (see note 2)
Tensile strength (UTS) (See note 3)		
Horizontal direction (XY)	442 MPa ±6 MPa	334 MPa ±1 MPa
Vertical direction (Z)	417 MPa ±27 MPa	339 MPa ±6 MPa
Yield strength (see note 3)		
Horizontal direction (XY)	264 MPa ±2 MPa	211 MPa ±2 MPa
Vertical direction (Z)	206 MPa ±6 MPa	174 MPa ±4 MPa
Elongation at break (see note 3)		
Horizontal direction (XY)	9% ±1%	9% ± 2%
Vertical direction (Z)	6% ±2%	4% ±1%
Modulus of elasticity (see note 3)		
Horizontal direction (XY)	71 GPa ±5 GPa	71 GPa ±2 GPa
Vertical direction (Z)	68 GPa ±2 GPa	66 GPa ±3 GPa
Hardness (Vickers) (see note 4)		
Horizontal direction (XY)	119 HV0.5 ±5 HV0.5	103 HV0.5 ±5 HV0.5
Vertical direction (Z)	123 HV0.5 ±2 HV0.5	98 HV0.5 ±5 HV0.5
Surface roughness (R_a) (See note 5)		
Horizontal direction (XY)	5 µm to 9 µm	
Vertical direction (Z)	7 µm to 9 µm	